Titre: Title:	Pulsed Laser Manipulation of Cells Decorated by Plasmonic Nanoparticles
Auteur: Author:	Mengjiao Qi
Date:	2019
Type:	Mémoire ou thèse / Dissertation or Thesis
Référence: Citation:	Qi, M. (2019). Pulsed Laser Manipulation of Cells Decorated by Plasmonic Nanoparticles [Mémoire de maîtrise, Polytechnique Montréal]. PolyPublie. https://publications.polymtl.ca/3885/

URL de PolyPublie: PolyPublie URL:	https://publications.polymtl.ca/3885/
Directeurs de recherche: Advisors:	Michel Meunier
Programme: Program:	Génie biomédical

POLYTECHNIQUE MONTRÉAL

affiliée à l'Université de Montréal

Pulsed Laser Manipulation of Cells Decorated by Plasmonic Nanoparticles

MENGJIAO QI

Institut de génie biomédical

Mémoire présenté en vue de l'obtention du diplôme de *Maîtrise ès sciences appliquées*

Génie biomédical

Avril 2019

POLYTECHNIQUE MONTRÉAL

affiliée à l'Université de Montréal

Ce mémoire intitulé :

Pulsed Laser Manipulation of Cells Decorated by Plasmonic Nanoparticles

présenté par **Mengjiao QI**
en vue de l'obtention du diplôme de *Maîtrise ès sciences appliquées*
a été dûment accepté par le jury d'examen constitué de :

Frédéric LESAGE, président

Michel MEUNIER, membre et directeur de recherche

Marc LAVERTU, membre

DEDICATION

This thesis is dedicated to my parents. As I had gone through super difficult time studying abroad, they offered me help and suggestions to support me to go on. I gained a lot during my study, both scientific knowledge and experience to tackle problems. They are good examples for me to be independent and strong in any situation.

ACKNOWLEDGEMENTS

I should thank my supervisor Professor Michel Meunier for offering me opportunity to finish the study abroad. He offered help when I was in hard situations. He cares a lot about his students. I appreciate all the guidance, help and support from my supervisor.

I would also thank the members of jury for my thesis, professor Frédéric Lesage and professor Marc Lavertu, for their precious time on reviewing my thesis and taking time for my thesis defense.

Many thanks to the research associate Dr. Sergiy Patskovsky in the group, he spent much time with me to tackle the problems in my experiment, initiated me with some ideas those are quite important for me. I appreciated so much for his efforts and help.

Thanks to my colleagues in the group. Their kindness and support helped me to solve many specific problems in the lab.

RÉSUMÉ

Au cours des dernières décennies, la thérapie cellulaire a suscité un intérêt considérable dans les domaines de la recherche biomédicale et théranostique. Une large gamme d'applications biomédicales a obtenu des avantages fructueux par une manipulation directe de cellules (cellules seuls ou groupes de cellules individuelles) en contrôlant la concentration de nanoparticules plasmoniques fonctionnelles et de lasers à impulsions. Cependant, tous ces protocoles de transfection, accompagnés d'une efficacité et d'une toxicité de transfection cellulaire variées, sont applicables pour une condition spécifique. Ainsi, l'optoporation doit être explorée, optimisée et généralisée pour un large éventail de thérapies cellulaires délicates et complexes par le laser.

Un suivi en temps réel des cellules optoporées révèle les mécanismes impliqués dans une transfection réussie sans induire de cytotoxicité. Dans cette thèse, le laser pulsé nanoseconde (532 nm) utilisé pour optoporer une seule cellule cancéreuse humaine du sein (MDA-MB-231) montre clairement les effets des fluences du laser pulsé. L'optoporation intériorise les molécules exogènes (Iodure de Propidium) dans l'intervalle fonctionnel compris entre 0.3 et 0.7 J/cm^2 sans provoquer d'effet secondaire (confirmé par Calcein AcetoxyMethyl). La position du faisceau détermine clairement dans quels compartiments subcellulaires les molécules exogènes à intérioriser avec précision. Le faisceau laser focalisé près du noyau dirige intensément l'Iodure de Propidium (PI) pour qu'il réagisse avec les nucléotides cellulaires, alors que pour le faisceau focalisé loin du noyau, le PI se déverse à peine dans le site d'action. Ce protocole d'optoporation, indiquant le rôle critique des nanoparticules plasmoniques liées, nécessite un faisceau laser dirigé vers la position de la nanoparticule plasmonique sur la membrane cellulaire. L'éclairage latéral par LED développé ici visualise simplement la nanoparticule plasmonique liée sur la membrane cellulaire dans une grande zone.

Par la suite, un laser femtoseconde dans le proche infrarouge (800 nm) est également utilisé pour optoporer des cellules de lymphocyte T humaines supersensibles (Jurkat) avec un taux de survie négligeable après une exposition de courte durée à une fluence relativement élevée (252 mJ/cm^2). En explorant plusieurs fluences laser et durées d'irradiation, nous obtenons donc une gamme applicable de fluences laser (63 à 71 mJ/cm^2) et de temps d'irradiation (10 ms) pour l'optoporation de cellules de Jurkat liées à des nanoparticules plasmoniques sans réduire leur viabilité cellulaire. Ces résultats fondamentaux indiquent comment effectuer une optoporation réussie en ajustant les

paramètres du laser (fluence, durée d'irradiation, position, etc.) sur différentes lignées cellulaires afin d'atteindre une haute transfection pour une large gamme d'applications biomédicales.

ABSTRACT

In the last decades, cell therapy has attracted tremendous interests in biomedical and theranostic research fields. A wide range of biomedical applications has gained fruitful benefits by a direct manipulation of cells (whether single cell or bunch of individual cells) by controlling the concentration of functional plasmonic nanoparticles and pulsed lasers. However, all these transfection protocols, accompanied by a varied cellular transfection efficiency and toxicity, are applicable for a specific condition. Thus, the optoporation needs to be explored, optimized, and generalized for a broad range of delicate and complex laser mediated cell therapies.

A real-time monitoring of the optoporated cells reveals mechanisms involved in a successful transfection without inducing cytotoxicity. In this thesis, the nanosecond pulsed laser (532 nm) used to optoporate a single adherent human breast cancer cell (MDA-MB-231) clearly shows effects of the pulsed laser fluences. The optoporation internalizes the exogenous molecules (Propidium Iodide) at the functional range between 0.3 to 0.7 J/cm^2 without causing a side effect (confirmed by Calcein AcetoxyMethyl). The beam pointing location clearly determines in which subcellular compartments the exogenous molecules to be internalized precisely. The laser beam localized close to the nucleus intensively directs the Propidium Iodide there to react with cellular nucleotides, whereas the beam far away from the nucleus barely fluxes into the site of action. This optoporation protocol, indicates the critical role of the bound plasmonic nanoparticles, is required a laser beam to be directed to the position of the plasmonic nanoparticle on the cellular membrane. The lateral LED illumination developed here simply visualizes the bound plasmonic nanoparticle on the cell membrane in a large area.

Afterward, near-infrared femtosecond laser (800 nm) is also employed to optoporate supersensitive human T lymphocyte cells (Jurkat) with a negligible survival rate after a short time exposure to a relatively high fluence (252 mJ/cm^2). Exploring several laser fluences and irradiation durations, we therefore obtain an applicable range of laser fluences (63 to 71 mJ/cm^2) and irradiation time (10 ms) for the optoporation of plasmonic nanoparticles bound Jurkat cells without reducing their cell viability. These fundamental results indicate how to perform a successful optoporation by adjusting laser parameters (i.e., fluence, irradiation duration, position, etc.) on different cell lines in order to achieve high transfection for a wide range of biomedical applications.

TABLE OF CONTENTS

LIST OF TABLES

LIST OF FIGURES

LIST OF SYMBOLS AND ABBREVIATIONS

Abs   Antibodies

AgNPs   Silver Nanoparticles

AuNPs   Gold Nanoparticles

AuNRs   Gold Nanorods

BE   Beam Splitter

bp   base pair

Cal-AM   Calcein AcetoxyMethyl

DFM   Dark Field Microscopy

DI   Deionized

DMEM   Dulbecco's Modified Eagle's Medium

FBS   Fetal Bovine Serum

IHC   Immunohistochemistry

LEDs   Light Emitting Diodes

NA   Numerical Aperture

NPs   Nanoparticles

PBS   Phosphate Buffered Saline

pDF   partial Dark Field

PDs   Polymer Dots

PI   Propidium Iodide

PS	Penicillin and Streptomycin
PSF	Point Spread Function
QDs	Quantum Dots
RI	Refractive Index
RLM	Reflected Light Microscopy
ROI	Region Of Interest
SIM	Side-Illumination Microscopy
UCNPs	Upconversion Nanoparticles

LIST OF APPENDICES

CHAPTER 1   INTRODUCTION

Cell membrane as a biological barrier always keeps separated intracellular and extracellular compartments. Delivery of exogenous biomolecules into the intracellular compartments is highly interesting and functional for such applications including gene therapy. The small molecules in the cell medium like ions can easily penetrate the cell membrane by the passive diffusion through the ion channel [1]. However, large molecules such as DNA plasmids cannot penetrate in the same way due to a limited membrane permeability [2]. There are many methods, which enhance the internalization of large molecules into the cells (Figure 1.1). Virus-mediated transduction employs viral vectors, which contain functional nucleotides to be delivered into the cells [3-5]. However, this technique is not favored due to all inflammation and toxicity concerns and limited package load, even though the transduced cells earn a stable expression. The chemical engineered polymer or particles incorporating nucleotides do not have stable behaviors such as the destabilization of the structure due to the different environments of the treated cells [6, 7]. Mechanical methods such as microinjection and gene gun have high selectivity; however, these strategies show certain drawbacks such as low throughput of the cell treatment and high demand for skilled technicians[8, 9]. The physical methods, including I- electroporation (depending on charging electricity to increase cell membrane permeability), II- sonoporation (using ultrasound generated microbubbles to rupture cell membrane) and III- optoporation (applying laser energy to damage cell membranes integrity by heating or vapor bubble formation) provide a controlled gene delivery [10-17]. Electroporation has high cell throughput in one shot (quick treatment strategy) but it is accompanied by reducing cell viability due to the high voltage. Sonoporation make an uneven ultrasound pressure on targeted cells, which causes cell death. Optoporation uses a laser to produce transient pores on the cell membrane and the exogenous molecules either passively diffuse into the cell or are actively pushed into the cells by the generated vapor pressure. Laser manipulation of the cells has no contact to cells to induce toxicity and offers high selectivity and precision. The laser mediated cell therapy provides a manipulation at a single cell level even at the subcellular level [18].
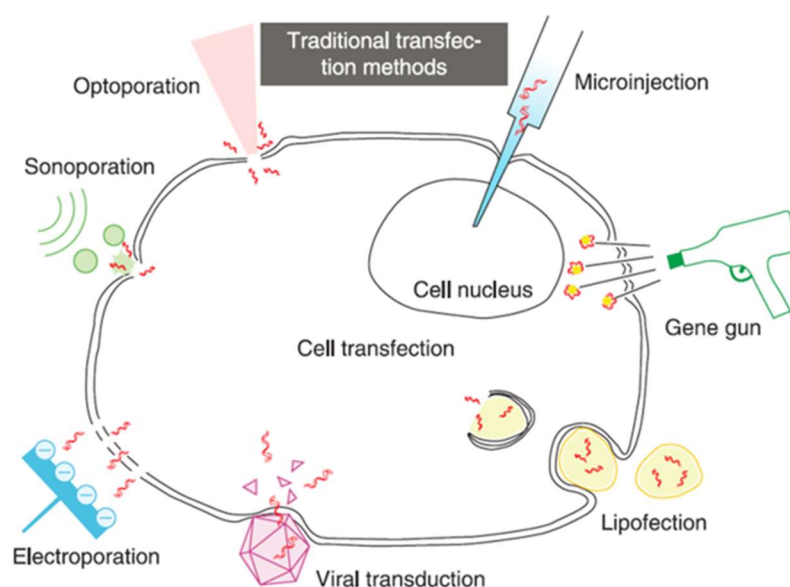
Figure 1.1 Schematic of traditional transfection methods. Reprinted from W. Ding et al. [19]

With different cell therapies mediated by lasers, the involved mechanisms for a membrane permeabilization depend on different laser types and irradiation parameters. Plasmonic nanoparticles (NPs) due to heating properties and near field enhancement effects play an important role in a laser-mediated cell perforation and significantly reduce the laser fluence threshold for minimizing cell damages [20-22]. The plasmonic NPs have variable optical and biological properties depending on different sizes, shapes and composites [23]. The NPs are able to offer spatial and temporal information by a laser irradiation with tunable parameters such as wavelength, laser energy, pulse duration. Moreover, the surface of plasmonic NPs can be chemically modified to bind to specific cells for a target-oriented laser irradiation. Among plasmonic NPs, the gold nanoparticles (AuNPs) are the most popular applied in the biochemical and biomedical therapeutic fields [24].

The AuNPs decorated cell optoporation mediated by the laser is a growing research field. In general, the permeabilization of the cell membrane is tuned by the heating and nanobubbles caused by the laser energy absorption of plasmonic NPs (Figure 1.2). By tightly focusing the laser on a single NP bound on the cell membrane, the permeability is increased, and the exogenous materials can locally flow into the cytoplasm. Whereas the higher throughput of the cell treatment is achieved by a loosely focused laser irradiating on NPs bound cells, and the treated NPs can rupture the integrity of the cell membrane to internalize extracellular materials.
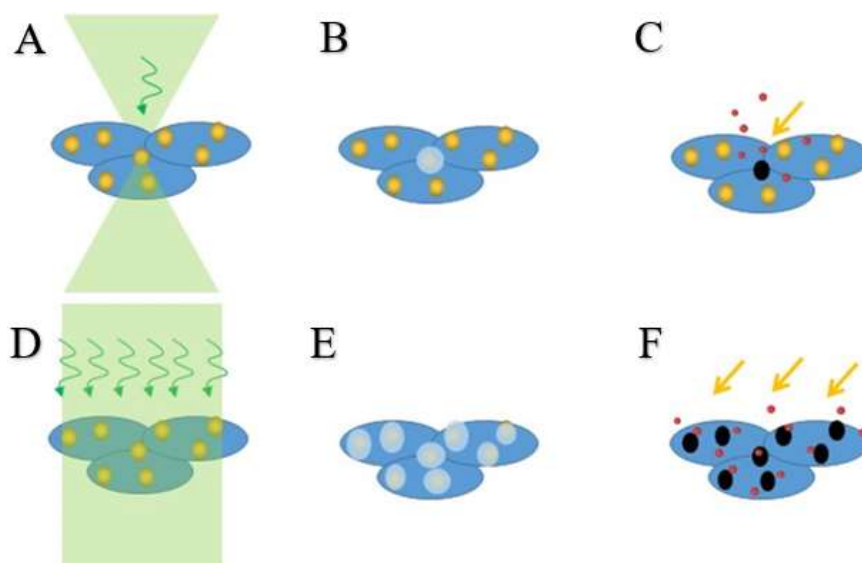
Figure 1.2 The NPs decorated cells have higher throughput optoporation with D) weak focused laser than A) the tightly focused laser beam. B) and E): the irradiated NPs provide spatial localization of the cell membrane rupture. C) and F): the permeabilized cell membrane takes the extracellular molecules into the cytoplasm.

1.1 Problems and objectives

Laser parameters (i.e., wavelength, pulse duration, laser fluence) are adjusted to focus on a single cell or target on a large quantity of cells for optoporation studies. Aiming at high transfection efficiency and cell viability through optoporation, most research focused on verifying cell optoporation efficiency and viability after hours of the laser treatment. Such a long waiting period makes it much tricky to precisely analyze these effective parameters and disregards all real-time changes. The study on the real-time responses of the laser treated cells is necessary for the optimized laser manipulation on the cells. As the adherent cells are investigated more for the laser manipulation studies because they are easy to operate, optoporation of the suspension cells with high efficiency is difficult to achieve due to the random and uneven hitting of the cell membrane by the laser irradiation [25]. Here, this thesis suggests studying the cellular real-time responses to the laser irradiation to optimize the optoporation parameters. The modifications on the optical setup for the visualization of NPs are also done to simplify the optoporation process. The exploration on the optoporation of NPs bound suspension cells (Jurkat cells) by the femtosecond laser paves the way for the highly efficient optoporation and transfection.

In this thesis, we target on solving certain issues involved in the laser-mediated cell manipulation for transferring exogenous materials into the cells without reducing the cell viability. The thesis is composed of different Chapters summarizing studies in this field through a literature review and indicating new experimental results:

1. Chapter 2 summarizes the related research in this field. Involving the viral-mediated cell transfection research, non-viral chemical-mediated studies such as the incorporated plasmid in the liposome, naked plasmid DNA, small interfering RNA (siRNA), micro RNA related research, DNA vaccine transfection method, physical-mediated methods and the most popular CRISPR involved transfection method in past few years.

2. Chapter 3 covers a real-time monitoring of single cell responses after the localized laser irradiation in order to understand the involved mechanisms. For this study, a nanosecond (ns) laser (532 nm) is used to irradiate the single AuNP (100 nm in diameter) bound MDA-MB-231 cell (an adherent human breast cancer cell). The localized membrane damage caused by the AuNP results in the uptake of the exogenous molecules. For this reason, Propidium Iodide (PI) staining molecules are used to indicate kinetics of the membrane damage by recording the real-time fluorescence signal change. The cell viability is then verified by means of Calcein AcetoxyMethyl (Cal-AM). The cellular responses after the laser irradiation are captured by monitoring intensity changes of the used fluorescent dyes and accordingly interpreted based on different laser parameters.

3. Chapter 4 describes how to develop a simple and elaborated side-illumination imaging device for the detection of plasmonic NPs in a cellular environment. As with the traditional NPs detection methods, the optical setup which has to incorporate laser irradiation optical path, fluorescence illumination path and signal collection path becomes more complicated, limiting the applications of cell manipulation by the laser. The side-illumination device is to solve the problem. A mixture of plasmonic NPs with different spectra can be also individually visualized and distinguished by their unique colors. The side-illumination imaging device is a useful setup for a wide range of biomedical applications such as disease diagnostic in pathology and cytology.

4. Chapter 5 presents an optimized range of effective parameters (i.e., laser fluence) of infrared femtosecond laser-mediated Jurkat cells optoporation. The individual Jurkat cell is

attached to the Petri dish substrate for investigation and optimization of femtosecond laser parameters. Suspension Jurkat cells are optoporated by femtosecond laser without and with decoration of AuNPs to study the influence of cell viability with different laser irradiation parameters. With experience from cellular response after laser irradiation, we use PI and Cal-AM to verify optoporation efficiency and cell viability. Various laser fluences are chosen for different applications, such as Jurkat cell optoporation and specific cell sorting. For further application of high-efficiency constant suspension cell optoporation mediated by femtosecond laser, some works are described in the appendix.

5. Chapter 6 discusses all results obtained earlier in the mentioned Chapters: monitoring of the plasmonic NPs bound single-cell response to ns laser optoporation paves the way to understand the relation of laser fluence and cellular real-time response, indicated by fluorescence signal change; side-illumination device replaces the traditional imaging methods of plasmonic NPs, with easy adaptation and high contrast; the proposed plasmonic NPs bound suspended cell optoporation mediated by femtosecond laser makes it possible for high throughput suspended cell optoporation.

6. Chapter 7 mainly focuses on the conclusions and suggestions of some future works.
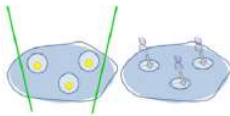
CHAPTER 2   LITERATURE REVIEW

As the transfection is a process that the exogenous nucleic acids are delivered into the cells, many techniques in different categories are widely developed such as the traditional viral vectors-mediated transfection, lipid-based transfection, and the popular physical methods in past decades, for instance, electroporation and optoporation [26]. However, the advantages and disadvantages of each of the most often used transfections methods are discussed: viral vectors can pack nucleic acids and introduce them into the cells with high efficiency, but it is time-consuming and causing the mutation concerns [27, 28]. Using recombinant viral vectors and non-viral carriers such as liposome is developed. Lipid-based transfection involves the lipid-soluble structures to be transferred into the cells incorporating the nucleic acids with minimum toxicity but low transfection efficiency [29, 30]. However, there are transfection methods for naked nucleic acids such as plasmid DNA and siRNA. Liu et al. demonstrated the significant gene expression in the liver of mice using the injection of naked plasmid DNA by simple mechanical massage [31]. The same method has been employed by siRNA (small interfering RNA) and microRNA for the transfection of kidney, liver and renal tubulointerstitial fibrosis cells [32-34]. Ghartye-Tagoe et al. reported the plasmid DNA transfection on differentiated intestinal epithelial monolayers by electroporation, and siRNA gene silencing. It was found that electroporation induced more expression and DNA uptake than lipofection with the reporter plasmids and siRNA resulted in up to 90% inhibition of targeted protein production [35]. DNA vaccines are plasmids that combine sequences required for replication and selection in Escherichia coli (bacterial region) with sequences needed to express an encoded transgene in vertebrate cells (eukaryotic region) [36]. DNA vaccines are inherently safe because the vectors are non-replicating, encode and express only the target antigen, not as with viral vectors. As they are well tolerated and the DNA product is highly stable, DNA vaccines have excellent safety profile in human clinical investigations [37]. The licensure of four animal health DNA vaccine products demonstrates the utility of DNA vaccination in large animals such as horses and pigs [38]. Wang et al. found that the human serum amyloid P binds and inhibits plasmid transfection and DNA vaccine induced adaptive immune responses more strongly than the murine counterpart [39], which raised difficulties for the DNA vaccine efficacy in humans. Moreover, most of developed delivery methods (such as the physical method: electroporation) can transfer the plasmid into the cytoplasm but rarely into the nucleus directly [40]. Thus, the developed and innovated design of the plasmid for the efficient delivery and diffusion to the nucleus need

highlighted exploration. Physical methods increase the cell membrane permeability by the external forces to open holes on the membrane, allowing exogenous nucleic acids to enter. The tunable parameters (electrical pulses for electroporation; laser wavelength, pulse width and laser fluence for optoporation) offer the alternatives for the transfection optimization [41, 42]. The electroporation treats the cells in the conductive suspension medium applying the electrical pulses, the induced charge accumulation opens the holes on the cell membrane. The membrane can repair when the electric field is removed. The electroporation is an easy method with a high quantity of the treated cells within a short time. However, it is required a commercial device and an optimized protocol for specific cell type transfection. A lot of cells are dead after the electrical pulse treatment due to the high voltage which needs the optimization [43-45]. The optoporation has been studied as a non-contact transfection method with spatial and temporal selectivity, and high targeting precision [46]. In the past few years, scientists have been working with a set of molecular scissors CRISPR (an enzyme that cuts DNA), which is the biggest breathtaking story in science as CRISPR makes genome edits cheaper and faster [47-50]. An important step to employ CRISPR on transfection is to deliver it into the cytoplasm or nucleus of the targeted cells. The transfection methods in different categories mentioned above can work with respective merits and drawbacks. As CRISPR has the biggest limitation that it is not a hundred percent efficient, and it has the off-target phenomenon [51-53] which is still under vast investigations. With various attention on the laser-mediated cell transfection, lots of studies are focusing on developing and optimizing the transfection process using the pulsed laser.

The objective of this master thesis is to investigate the pulsed laser optoporation accompanied by the plasmonic NPs, providing a controlled permeability to internalize exogenous materials into the cell. Both nanosecond and femtosecond lasers have been used to optoporate various cells (Table 2.1).

Table 2.1 Characteristic example of cell membrane optoporation and transfection application by the pulsed laser, referring to Etienne Boulais et al.[54]. Various cell types were optoporated or transfected by nanosecond laser or femtosecond laser under specific conditions. λ is wavelength, τ_p is pulse duration, F is single laser pulse fluence, E is the pulse exposure. T is the targeted cell.

Application	Laser&Target	Particles	Principle	Comments	Ref.
Cell membrane optoporation and transfection	λ=532 nm, τ_p=20 ns, F=500 mJ/cm^2 E : ~100 pulses T : Lymphocytes	-20 nm -AuNPs -Conjugated	-Bubbles	-Membrane recovers in 2 mins -Uptake of 10 kDa FITC-D	[55]
	λ=532 nm, τ_p=6 ns, F=500 mJ/cm^2 E : 1-50 pulses T : Hodgkin's disease and lymphoma cells	-15,30 nm -AuNPs -Conjugated	-Bubbles	-8-68% efficiency	[56]
	λ=532 nm, τ_p=0.5 ns, F=110-150 mJ/cm^2 E : single pulse T : Various	-Size not given -AuNPs clusters	-Bubbles	-Transfection of DNA plasmids -~70% efficiency	[57]
	λ=760nm, femtosecond, F=18 mJ/cm^2 E : 10 s@80 MHz T : epithelial breast cancer cells	-80 nm -AuNPs -Conjugated	-Low-density plasma	-Uptake of 10 kDa FITC-D	[58]
	λ=800 nm, τ_p=45 fs, F=100 mJ/cm^2 E : 10 s@80 MHz T : melanoma cells	-100 nm -AuNPs -Unconjugated	-Plasma-mediated bubbles	-~70% optoporation efficiency -Transfection of YFP-SMAD2 plasmids -~25% transfection efficiency	[59]

The role of plasmonic AuNPs on the cell membrane is crucial for providing an efficient laser-mediated cell optoporation and subsequent transfection. Plasmonic NPs are able to accumulate the electrons into an oscillatory movement by the irradiating light. When the frequency of the incident light is near the intrinsic plasmon frequency of the plasmonic NP, on-resonance phenomenon is accompanied by strong energy absorption. On the other hand, off-resonance happens when the NP's plasmon frequency is far from the frequency of the incident light and the energy absorption is no longer dominant to heat up, but to enhance the near field [60]. Boulais et al. [54] showed that the calculated absorption, scattering and extinction cross sections of AuNPs (100 nm in diameter) in water as a function of incident light (Figure 2.1.A). Figure 2.1.B showed the electric field distribution near the AuNP (100 nm in diameter) for low absorption and high near field enhancement. By tuning size, composite, shape of NPs and wavelengths of the incident light, NPs can be manipulated either on-resonance or off-resonance for different biomedical applications.
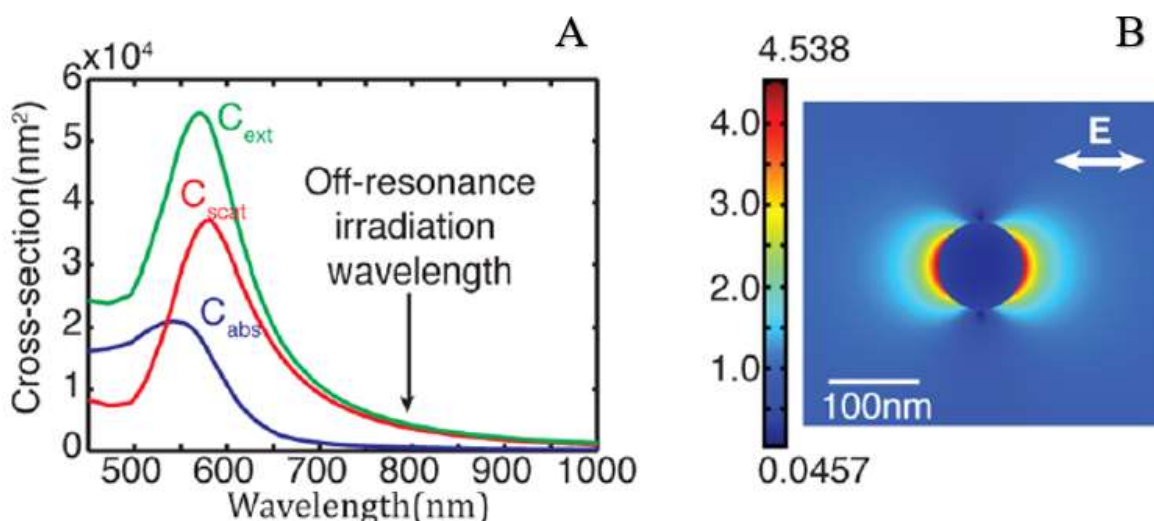
Figure 2.1 A) Scattering, absorption and extinction cross sections for 100 nm AuNP in water, showing the on-resonance wavelength around 570 nm and off-resonance wavelength in infrared. B) Electric field enhancement around the NP surface with low absorption and near field enhancement. Adapted from Ref. [54].

2.1 Nanosecond pulsed laser perforation on cells

As nanosecond laser is compact and relatively easy to operate, many optoporation studies have been performed with this type of laser [56, 61-63]. For the nanosecond laser cell perforation, the laser with wavelength in visible range (~532 nm) which is around the plasmon peak of 100 nm AuNPs (~570 nm) absorbs laser energy strongly and induces a temperature rise leading to the membrane permeability [64, 65]. The nanosecond laser cell perforation, mainly based on heating mechanisms of plasmonic NPs, causes a fragmentation of NPs and induces cytotoxicity. However, the use of a near-infrared laser (700-1000 nm) is highly desirable for a cell optoporation because the absorption by cellular components in this wavelength range is significantly low and indicates a great potential for a clinical translation.

2.1.1 Mechanism of nanosecond pulsed laser-induced cell perforation

The fluence for a single cell optoporation can be lowered through irradiation of single plasmonic NP binding to the membrane to keep the highest viability without reducing the transfection efficiency. The permeabilization using the plasmonic NP assisted optoporation involves two mechanisms including heating and vaporized nanobubbles (Figure 2.2) [66]. Allowing the fluorescent molecular agents enter the cytoplasm and becoming fluorescent.
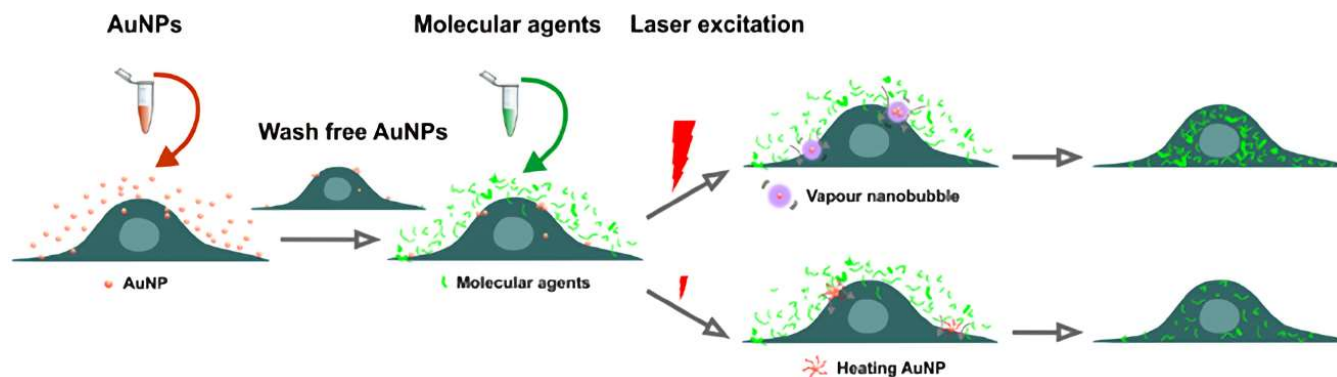
Figure 2.2 Schematic of the experimental procedure. After incubating cells with AuNPs and with the molecular agents. By applying different laser energies, cell membrane integrity is ruptured by vaporized bubbles (high laser energy) or heating of AuNPs (low laser energy). The treated cell membrane allows exogenous molecules to enter the cells. Adapted from Ref. [66].

2.1.2 Nanosecond optoporation of adherent cell

Nanosecond laser is a functional and applicable device for almost all cellular optoporation. For example, Krawinkel et al. have employed the Nd: YAG infrared nanosecond laser (1064 nm, 17 ns, 10 Hz) to deliver the PI molecules and GFP inserted plasmids into human breast adenocarcinoma MCF-7 cells. The cells were targeted by the laser and irradiated one by one. The optoporation (indicated by PI with energy density ~4 x 10^4 J/cm^2) and transfection (indicated by green fluorescent protein encoding plasmid into MCF-7 cells) were confirmed by the fluorescence microscopy [62]. Krawinkel et al. incubated primary human gingival fibroblasts (pHFIB-G) cells with AuNPs prior to the nanosecond laser irradiation (532 nm, 1 ns, 22.5 kHz). The optical setup could irradiate the cell samples by the laser with a large Rayleigh range (16.2 mm) by installing an extra lens (focal length f =250 mm). The laser irradiation resulted in high throughput of pHFIB-G manipulation (up to 85%) with 97% cell viability. The fibroblasts internalized dextran polymers with molecular weights up to 500 kDa to estimate the size of the pores on the membrane [63]. Yao et al. have also shown a cell specific optoporation by using antibody (BerH2: against CD30 and ACT1: against CD25) decorated AuNPs to target cells (Hodgkin's disease cell line L428 and human lymphoma cell line Karpas 299). The optoporation with 30 nm AuNPs transfected 68% of cells with FITC-Dextran with a cell death (27%) compared to the smaller AuNPs 15 nm [56]. Saklayen et al. cultured the HeLa CCL-2 cells on a thermoplasmonic substrate with an array of pyramids with a gold surface (Figure 2.3.A), developed controllable hotspots generated bubbles at

the underneath of the cell membrane using a nanosecond laser irradiation to internalize FITC-Dextran. The flow cytometry was used to evaluate the delivery efficiency: for the delivered cargos size ranging from 0.6 to 2000 kDa, the delivery efficiency was up to 95% for the smallest molecule and cell viability was up to 98% [67]. Xiong et al. selectively optoporated cells (Figure 2.3.B) using spatially resolved laser scanning manner and the nanoparticle-sensitized photoporation to internalize FITC-Dextran (10 kDa) according to the pre-defined pattern (for a selective location) or image-guided interactive method (a single cell targeting) [68].
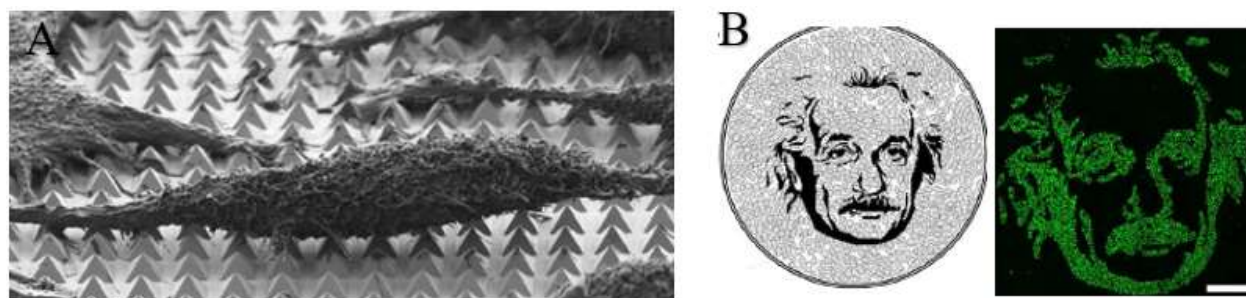
Figure 2.3 A) SEM of fixed HeLa CCL-2 cells on the thermoplasmonic substrate, referring to [67]. B) Illustration of the cell optoporation selectivity according to the black pixels of Albert Einstein drawing. The green fluorescence FITC-dextran with 10 kDa is successfully delivered into the optoporated cells. Scale bar is 1000 μm. Adapted from Ref. [68].

However, a real-time monitoring of cellular response of the individual cell receiving nanosecond laser irradiation has not been reported in order to further optimize the optoporation technique and facilitate a clinical translation of the optoporation.

2.2 Femtosecond pulsed laser perforation on cells

Plasmonic NPs-mediated femtosecond laser cell optoporation is quite popular, especially for near-infrared femtosecond laser due to avoiding the fragmentation of NPs and the toxicity [59, 69]. The near field enhancement around plasmonic NPs generated by a multiphoton ionization forms nanocavitation, to permeabilize the cell membrane. The femtosecond laser cell optoporation with high selectivity, efficiency and viability is a hot topic for cell therapy and further clinical translation.

2.2.1 Mechanism of femtosecond pulsed laser-induced cell perforation

The infrared femtosecond laser (~800 nm) perforating cell membrane has been studied using an objective in the inverted microscope optical setup to precisely target the specific cell and generate spatially confined holes [70-72]. The opened pores allow exogenous biomolecules to diffuse into the cell cytoplasm. However, it is needed an alignment of the femtosecond laser to precisely focus onto the cell surface and target surface bound plasmonic NPs. Thus, the membrane bound NPs address the location of the cell membrane due to their intrinsic scattered light. Locating the cell membrane surface by bound NPs, cells can be permeabilized with femtosecond laser irradiation. The femtosecond laser-mediated AuNPs bound cell membrane permeabilization is based on two fundamental mechanisms including a near field enhancement and particle heating effect [54, 73, 74]. The near field enhancement occurs due to collective oscillations of electrons in AuNPs caused by the incident laser electromagnetic field. The heating effect of the NPs occurs owing to the energy absorption from the incident irradiation. The dominant mechanism for an infrared femtosecond laser irradiation, for instance, on AuNPs (100 nm in diameter) involves an energy transfer and plasma generation in order to induce nanocavitation. The mechanism, corresponding to the energy absorption and light scattering by AuNPs in different laser irradiation intensities, depicted in Figure 2.4. The NPs absorption dominates in the nanostructure and heats the gold electrons when it is in-resonance. In off-resonance, the absorption is relatively low, and the light can be scattered in the near field of NPs to enhance the near field effect. When the laser intensity reaches over the optical breakdown threshold, the electronic plasma is generated near the NPs structure. Continuous laser energy absorption by the plasma finally transfers into the release of the pressure waves, which results in a nanocavitation bubble eventually [54, 75]. These induced effects, in turn, reduce cell membrane permeability, enabling diffusion of exogenous molecules into the cytoplasm.
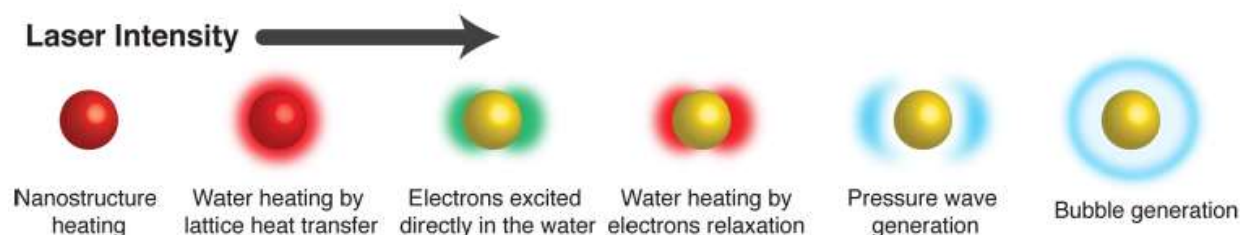
Figure 2.4 Schematics of different NPs phenomena with increased laser irradiation classified in the term of laser intensity. Adapted from Ref. [54].

2.2.2 Femtosecond optoporation of adherent cell

The femtosecond laser for cell therapy shows a great potential in a wide range of biomedical and biophotonic applications for providing efficient transfection through a non-toxic cell optoporation. The femtosecond laser optoporation has used to transfect the adherent cells, such as CHO cells (represent a mammalian model system for optical transfection study), melanoma cells (human skin cancer model), and MDA-MB-231 cells (transfection of human breast cancer cells) [59, 69, 76, 77]. The adherent cells should be pre-cultured into a petri dish in the suggested cultured medium complex until reaching at confluency more than 90%. On the day of the laser treatment, the cells are incubated with plasmonic NPs at a specific concentration. Depending on specific applications, some bound NPs need to be surface modified by binding specific membrane antigen receptors to attach specific cell types [69]. The pre-programmed laser scanning pattern allows a high throughput of the treated cells [78, 79]. The perforation of cell membrane by femtosecond laser is controllable to generate a wide range of patterns by different laser scanning modes (Figure 2.5).
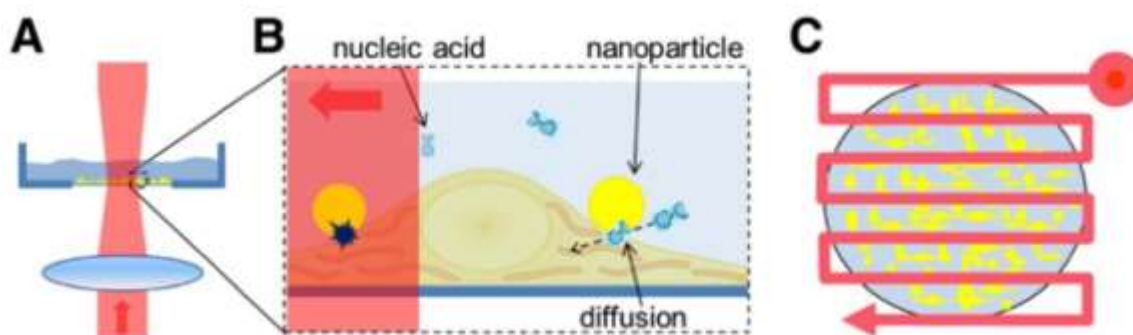
Figure 2.5 A) demonstrates a side view of the laser irradiation treated cell samples with a loosely focused femtosecond laser. B) shows the laser irradiation on NPs decorated cell samples and the permeabilized membrane allows the exogenous nucleic acid to enter. C) programmed laser irradiation scanning pattern for treating cells in large quantity. Adapted from Ref. [79].

To apply the optimized protocol for a single cell optoporation to a bunch of cells, Georg Breunig et al., achieved the automated CHO cell optoporation by using the infrared femtosecond laser (800 nm, 85 MHz, sub-15 fs). The whole automated setup was designed to find the location of the cells and designate the cells for a laser focal point for irradiation. The software dominant method could target 7-8 cell positions per second for an illumination duration of 100 ms and achieved effective 10,000 cells treated per hour automatically. Employing a uniform laser focal region (i.e., beam shaping to quasi-Bessel beam geometry) can also raise the number of the laser treated cells. The

maximum cell viability after the optoporation was observed around 60-70% [78]. Baumgart et al. used off-resonance femtosecond laser based high throughput virus and fragmentation free transfection method for AuNPs bound melanoma cells. The femtosecond laser was with a center wavelength of 800 nm and a repetition rate of 1 kHz. The laser irradiation optical setup was incorporated with the in-situ spectroscopy to study the fragmentation of NPs and the confocal microscopy for the visualization. A high throughput of laser treated cells was obtained using an optimized speed (40 mm^2/min) with a low toxicity (<1%) and high transfection efficiency (~3 fold higher than the lipofection). They also proposed that the further work on the bioconjugation modified NPs could lead to the promising spatially selective treatment of cells of interest [59]. Bergeron et al. modified the surface of plasmonic NPs and applied these antibody conjugated NPs to target specific cells for a laser treatment. With the conjugated NPs, optoporation of the targeted specific cells in co-culture cell lines (MDA-MB-231 cells positive CD44, and RAW661 cell negative CD44) was achieved using an infrared laser (800 nm) without affecting the non-targeted cells. The threshold to have a selective optoporation was found with 49 pulses at 250 Hz or 97 pulses at 500 Hz [69].

For the numerous investigations on femtosecond laser applied for NPs bound adherent cell optoporation, the cells were on the petri dish substrate and could be controlled by the built-in translation stage in any designed movement. As a comparison, the manipulation of the suspended cells for an efficient transfection using the femtosecond laser optoporation remains challenging because the floating nature of suspended cells, making it hard to manipulate.

2.2.3 Femtosecond optoporation of suspension cell

Transfection of suspended cells has been proven to be quite difficult due to the intrinsic nature of the cell floating character. The common liposome-based non-viral vectors due to a low molecular binding and uptake are not suitable for the transfection of suspended cells [80-82]. However, optoporation is a cell type non-dependent method to perforate the membrane efficiently including the suspended cells. Certain protocols have been developed for a high-efficiency transfection of suspension cells such as chicken eggs coated culture plates to eliminate the nonadherent cell[83] as well as a real time femtosecond laser irradiation in microfluidic system for a spatial confinement of the cell flow [84]. However, cells' immobilization onto the substrate, requires a pre-treatment

on the petri dish. Moreover, the microfluidic setup with a constant flow needs sub-micron accuracy for positioning of the laser beam on the cell membrane to reach a high-efficient perforation [85].

Marchington et al. have used femtosecond laser (800 nm, 80 MHz, 100 fs) to irradiate individual suspending human embryonic kidney (HEK293) cells in a microfluidic channel. The focused laser beam generated transient pores which allowed uptake of the extracellular molecules in the surrounding fluid into the cytoplasm. The optical setup enabled the rate of cell treatment at 1 cell/s and several thousand cells per hour. The optoporation efficiency ($42 \pm 8\%$) and cell viability ($28 \pm 4\%$) were tested by PI and Cal-AM cell stains. They also suggested the future development should include the integration of the lab-on-chip technology with the existing setup, incorporating fluorescence spectroscopy [86]. Georg Breunig et al. explored the transfection of the trypsinized CHO cells by using the 800 nm, 85 MHz, sub-15 fs laser, embedded into a microflow system, including the reshaped laser beam focal region into a zero-order quasi-Bessel beam for relative uniform laser energy deposited on the cells. After the transfection (24 h), a small part (~1%) of the bunch of laser treated cells expressed GFP. The lower transfection efficiency compared to the single cell optoporation in petri dish was related to a shielding effect, impedes well-contributed laser fluence in the confined microfluidic channel. The low transfection efficiency might be improved by increasing the cell number and scanning rate of the laser beam [84].

2.3 Summary

Different transfection methods are mentioned with their advantages and disadvantages, transfection by optoporation is chosen for the study due to the variable parameters (i.e., wavelength, pulse width, fluence etc.), controllable spatial and temporal selectivity, and cell type non-dependent.

CHAPTER 3   REAL-TIME MONITORING OF PLASMONIC NANOPARTICLE-MEDIATED PULSED LASER SINGLE-CELL OPTOPORATION

In this chapter, a single cell therapy was demonstrated with the aid of plasmonic NP-pulsed laser optoporation. A reflected light microscopy (RLM) with a high numerical aperture (NA) objective is initially developed to provide precise localization of an individual NP bound to the cell membrane and spatially control of the single cell optoporation. All effective parameters including nanosecond laser exposure, laser fluence and optomechanical particle-membrane interaction were then optimized by developing an algorithm for an error-free automatic alignment of laser focus with the bound NP. We proceed to study the single cell optoporation by a systematic analysis of the internalization of PI molecules and perforation kinetics. The internalization rate of PI molecules through a time-dependent perforation indicates a range of suitable fluences (0.3-0.7 J/cm^2) without inducing cell death. The developed NP imaging strategy for a live cell based on RLM, fully compatible with a simultaneous fluorescence microscopy imaging, also provides a real-time observation and systematic analysis of cellular responses. Our results demonstrate that optimized mechanisms and parameters involved in the single-cell optoporation are critical to achieve a successful perforation and cell therapy for a broad range of biomedical applications.

3.1 Introduction

3.1.1 Research question

An elaborated nanomedicine, provides a single cell therapy among a cluster of different cells (i.e., cancer and healthy cells with a broad range of physical and biological features), is now achievable by employing a plasmonic particle-mediated single-cell optoporation [87]. A non-specific optoporation of a cluster of cells by a blind scanning mode consisted of an unequal distribution of Gaussian intensity of laser light (i.e., generation of a wide range laser powers on the cell membrane and reoccurrence of the laser exposure) mainly induce cell death. Therefore, single-cell optoporation, which focuses on a precise laser manipulation of an individual cell targeted by functional plasmonic NPs, controls all effective aspects of laser irradiation, including laser fluence and irradiation duration; however, the blind laser scanning mode affects most of the cells around the laser point and subsequently their normal proliferation and cycle [69]. Moreover, the laser

operation in the highly focused pointing mode, which provides greater selectivity compared to the loosely focused scanning mode for an individual cell optoporation, can act as a microscalpel to generate a local disruption of the cell membrane locally and precisely transfer exogenous biomolecules into intracellular compartments [88].

The position of the laser beam whether to irradiate nuclear-targeted or cytoplasm-targeted plasmonic NPs is critical to obtain suitable cellular responses and improve optoporation efficiency [89, 90]. The irradiation near nuclei provides a narrow laser parameter manipulation range due to inducing cell death; however, irradiation far from nuclei gives a wider laser manipulation range, which is suitable to achieve a high optoporation efficiency (i.e., the threshold to induce cell death when the irradiation is near the nuclei is below the laser fluence of 695 mJ/cm^2 but not for the irradiation afar).

Therefore, plasmonic NPs bound on the cell membrane, acts as an error-free membrane marker, provide a highly spatial localized optoporation using the highly focused pointing mode. Highly focused laser optoporation requires well-developed plasmonic NPs (i.e., target a specific cell), simultaneous visualization of the fluorescence dynamic (i.e., permeabilize the plasma membrane by adjusting the transient pore size and resealing rate), and numerical simulation of the optoporation process (i.e., provide accurate optoporation and transfection for a wide variety of biomedical applications). Thus, a successful development of the single cell optoporation can minimize side effects of the laser irradiation and improve the transfection of the targeted cell at the subcellular level.

3.1.2 Objective

In this chapter, we investigate a real-time single cell response to nanoparticle-mediated pulsed laser optoporation and then develop a spatial and temporal monitoring system to in situ control and optimize in vitro single cell laser optoporation.

3.2 The proposed approach

We here develop a nanosecond laser-based optoporation setup to integrate plasmonic NPs (act as the cellular markers) with a high NA objective (allows a precise localization of NPs), automated laser focus positioning, and longtime measurement of the dynamic of fluorescence. An extensive

study is also aimed to evaluate effective laser parameters (i.e., laser fluence) on biomolecular delivery in situ. In this case, the optimized parameters of the laser for generating an effective optoporation will be confirmed by pursuing cellular targeting (i.e., a backscattering imaging system using a high numerical aperture objective to visualize single NP bound plasma membrane), delivery of exogenous substances such as fluorescent PI molecules with a strong quantum yield [91, 92], and their transport kinetics into the optoporated cell and intracellular compartments. A real-time measurement of the corresponding fluorescence intensity of the exogeneous fluorescent PI molecules, inflows to the cytoplasm (simulated according to Davis's diffusion model [11]), determines the permeabilization and subsequent recovery processes. Using high-speed shadowgraphic imaging in situ also shows how to follow the status of bubble generation and sizes on the pore formation and recovery.

3.3 Methodology

3.3.1 Cell culture, PI transfection, and live cell assay

MDA-MB-231 cell (Human breast cancer cell line, American Type Culture Collection, Manassas, VA, USA) with a density of $1x10^5$ cells/well were seeded into a glass bottom Petri dish (19.625 cm^2, MatTek, Ashland, MA, USA) by adding Dulbecco's Modified Eagle's Medium (DMEM) supplemented with 10% fetal bovine serum (FBS, Invitrogen) and 1% penicillin (100 units/mL, Invitrogen) to reach 80% confluency overnight (37 °C with 5% CO_2). After a washing step (using buffered phosphate saline, PBS, Sigma-Aldrich), the cells were then incubated with 8 μg/ml of AuNPs (50 μg/mL, 100 nm in diameter, A11-100-CIT, Nanopartz, Loveland, CO, USA) in the DMEM for 2 h in the incubator (37 °C with 5% CO_2). Afterwards, the treated cells were washed three times with PBS prior to the laser treatment to remove unbound NPs. In this chapter, AuNPs (100 nm in diameter) were used without further modifications. The dynamic is detected by adding PI (ThermoFisher Scientific) with a final concentration 1.5 μM (diluted in DMEM) to the treated cells 30 minutes before the laser irradiation. The cell viability of the treated cells was evaluated by using Calcein Acetoxymethyl (Cal-AM, ThermoFisher Scientific) with a concentration of 1 μM at 2 h post-irradiation.

3.3.2 Preparation of optical setup for optoporation and visualization

The experimental setup for a single-cell optoporation (Figure 3.1) consists an inverted Eclipse Ti microscope (Nikon, Mississauga, ON, Canada) equipped with a high NA objective (100X, oil immersion, variable NA:0.5-1.3, Nikon) accompanied by a refractive index (RI) of immersion oil is 1.51 at 23 °C (Olympus Scientific Solutions Americas). The glass-bottom petri-dish was then placed in a humidified CO_2 cellular incubator system (Live Cell Instrument, Korea) installed on a flat top 3D motorized translation stage (H117P1, ProScan, Prior Scientific, Rockland, MA, USA). The laser beam was automatically focused on the targeted NPs by using the z-step scanning system. The focal spot size was roughly calculated as the value of wavelength around 500 nm.

A fluorescence lamp C-HGFI Intensilight (Nikon) with ET-DsRed excitation filter (545 ± 30 nm, Chroma Technology, USA 49005) provided a light for PI fluorophores excitation (~ 535 nm) and cell-NP complex visualization with a QIClick digital CCD camera (QImaging, Surrey, BC, Canada). The detection of real-time living-cell fluorescence dynamic was performed using another CCD camera (Hamamatsu R2) equipped with a corresponding PI fluorophore emission filter (620 ± 60 nm, Chroma Technology, USA 49005). Cal AM was then detected by a filter sets (Ex: 500 ± 20 nm, Em: 535 ±30 nm, Chroma Technology, 49003-ET-EYFP, USA).

The laser source used for cell perforation was an ultra-compact 15 nanosecond laser (QC532, CrystaLaser, USA) working at 100 Hz and 532 nm wavelength. The laser power was controlled by the homemade software (developed function integrated in LabView to control attenuator and shutter for laser irradiation) with the rotation of a half-wavelength waveplate combined with a plate polarizer on the beam path. The irradiation time was automatically controlled by the mechanical shutter (Thorlabs) connected to the software. A beam expander accompanied by a diaphragm was also used to adjust laser focal point size by changing the effective NA. As double decks were placed under the objective from the Nikon microscope to provide two optical pathways: (1) the upper path was conducted to a laser 90:10 beam splitter (Thorlabs, Newton, NJ) from the backport of the microscope to the sample after going through the objective, and (2) the second path separated a wide field NP imaging and fluorescence illumination using a 50:50 beam splitter. Cell perforation was performed by using LabView software to generate a Gaussian fit for PSF of the bound NP, recording the position of the NP, and controlling the translation stage to move the NP's position to the initial laser focal point position. The NP was precisely selected and well aligned according to

the laser beam path to provide an effective optoporation on a single cell. Note, several automatic iterations of alignment of NP and laser focus processes were employed to achieve the laser focal point due to certain instabilities (i.e., vibration of the optical table).

A standard white light source (Nikon) with 50 W halogen lamp was employed to provide a conventional transmission microscopy and 3D imaging with partial Dark-Field (pDF) microscopy. Partial illumination from Halogen lamp was blocked using an opaque paper before the darkfield condenser (NA=0.9, Nikon) to enhance imaging contrast by creating artificial shadows (Figure 3.1).
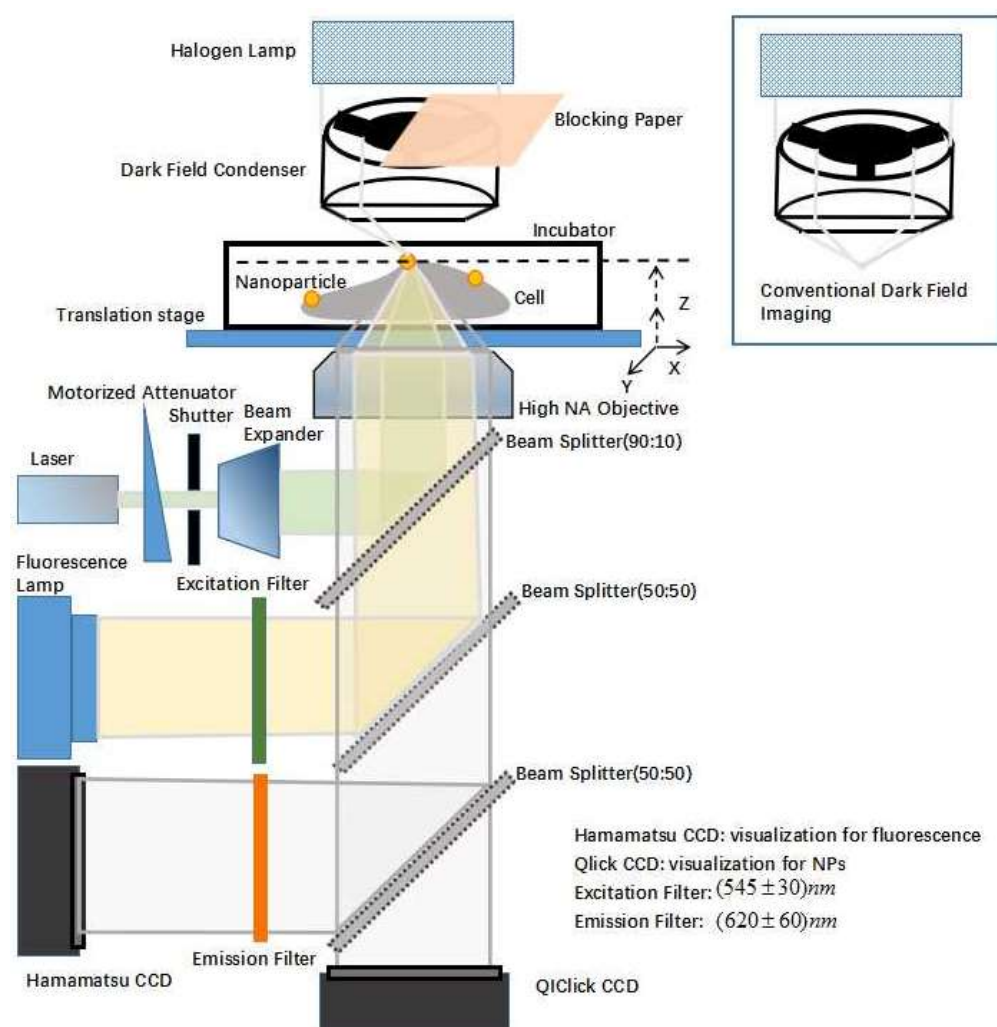
Figure 3.1 Schematic of the experimental setup for the single-cell optoporation. AuNP serves as membrane position target and field enhancement factor for localized optoporation.

3.4 Results and discussions

3.4.1 RLM imaging of NPs in a cellular environment

The developed optical setup provides an excitation light for fluorescence imaging following laser irradiation on the chosen region of interest (ROI). Using a high magnification oil immersion objective and darkfield condenser, bound NPs on the cell membrane can be precisely visualized. To achieve a reliable identification and spatial localization of NPs on the cell membrane, the NPs were imaged based on the high backscattering signal detection [93, 94]. RLM, which is compatible with pDF imaging, simultaneously visualize both cell and NPs (Figure 3.2).
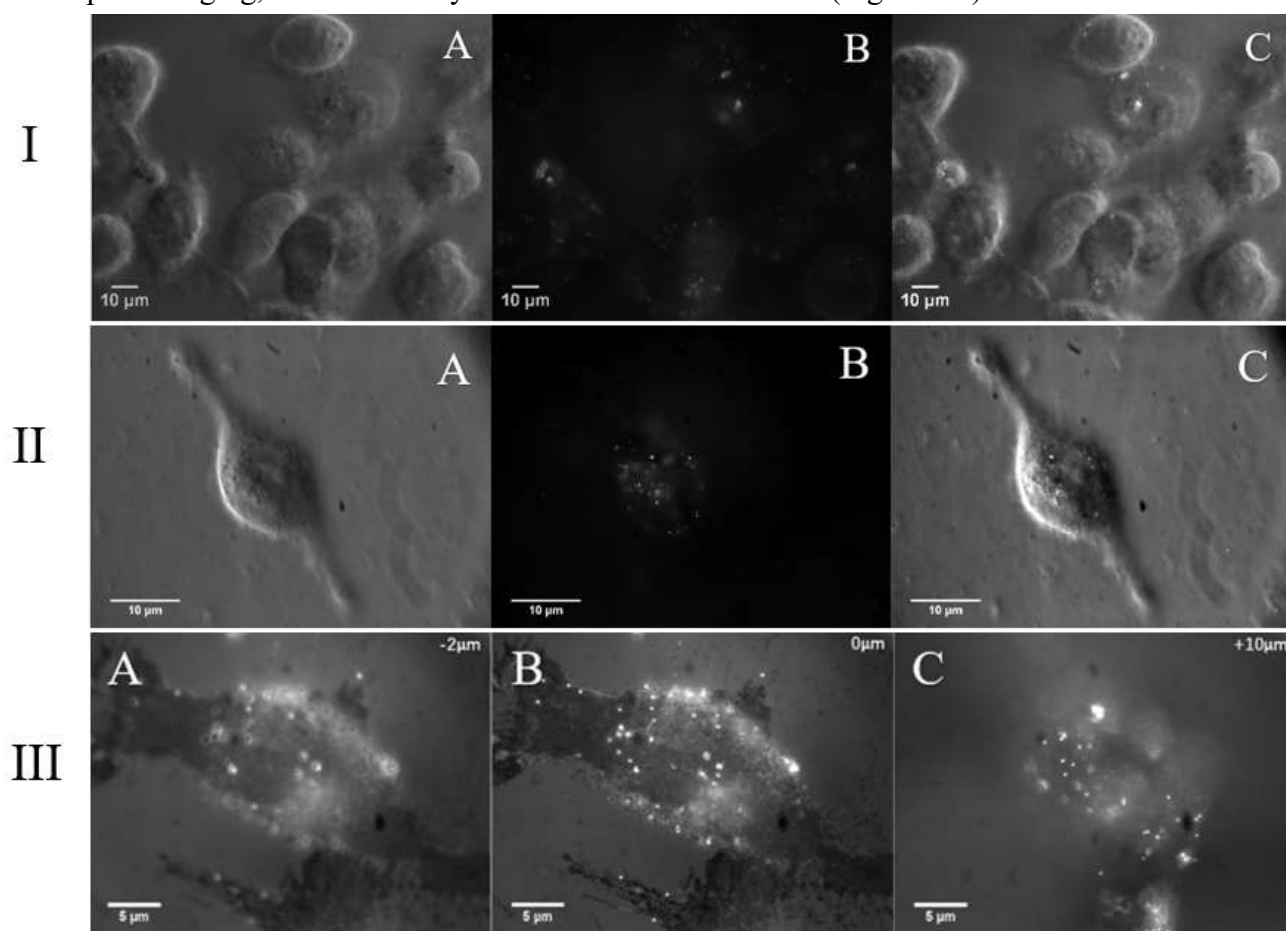
Figure 3.2 Cell-NP images taken with I) 60X objective and II) 100X objective. A) Images acquired in pDF imaging of cells; B) RLM imaging of NPs on the cell surface; C) Combination of pDF and RLM imaging. The scale bar is 10 μm; III) RLM imaging of NP distribution on a single cell at -2 μm, B) 0 μm (at the bottom of petri dish substrate) and C) 10 μm position (NPs on top surface of the cell membrane). The scale bar is 5 μm.

The typical experimental images of cells decorated with AuNPs (100 nm in diameter) are illustrated in Figure 3.2.I (60X oil immersion objective with NA:1.4, Nikon) and Figure 3.2.II (100X oil immersion objective with NA:0.5-1.3, Nikon). The images acquired by pDF and RLM and their combination (overlapped images) using 100X oil immersion objective shows an improved contrast to differentiate targeted NPs and cells and analyzed the distribution of bound NPs at different positions of the cell membrane by tuning z-step (Figure 3.2.III).

3.4.2 NP-laser alignment

A controlled optoporation of an individual cell depends on the precision of 3D spatial alignment of laser focal point with a bound NP on the cell membrane. Owing to the high NA (0.5-1.3) objective and sharp laser energy distribution, small miss-displacement (in a nanoscale) of the laser focal point from the bound NP induces a dramatic laser energy loss. Therefore, a fine z-scanning (-2 μm to +2 μm, step size: 0.1 μm) remarkably indicates the laser beam 3D intensity distribution (laser Gaussian energy distribution) and focal point on a Si-wafer (full reflection of laser irradiation) (Figure 3.3).
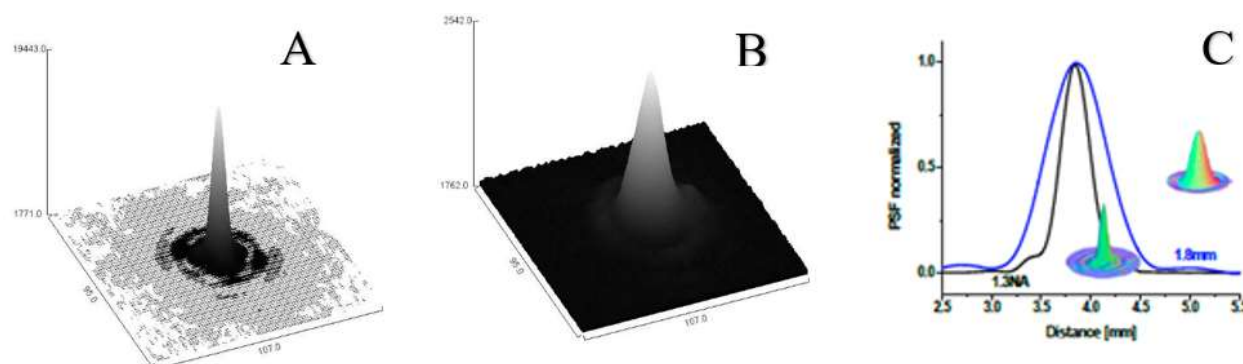
Figure 3.3 Illustration of the 3D energy distribution of the laser focus when NA equals to A) 1.3 and B) effective diaphragm is 1.8 mm. C) shows the Point Spread Function (PSF) normalization of energy distributions of two NAs.

3.4.3 Analysis of perforation dynamics

Accurate delivery of exogenous biomolecules into an individual cell and its subcellular compartment provides a precise functionality and control in cell therapy [95]. The investigation and analysis of cellular responses after the laser irradiation can be tackled down by using the developed microscopic setup (see above section). Therefore, the perforation dynamics can be

characterized by tracking the PI internalization at the localized perforation (i.e., detecting temporal and spatial fluorescence intensity changes). In the developed tracking system, the nanoparticle-mediated optoporation shows four typical perforation dynamic trends for the treated MDA-MB-231 cells incubated with AuNPs (Figure 3.4). The different laser fluences (0.3, 0.7, 1.5 and 2.2 J/cm^2) were applied to study the internalization of PI molecules. PI molecules were internalized by the perforated single cell, which showed a higher fluorescence intensity compared to the non-perforated cell. Depending on membrane disruption, the quantity of PI uptake indicates different responses (according to the fluorescence intensity measurement). PI molecules (668.4 Da) enter into the cytoplasm to form fluorescent PI-nucleic acid complexes, and PI molecules can diffuse into the nucleus by crossing the nuclear membrane and pores since they are 10-20 times smaller than short double-stranded oligomers (10-20 bp) [6]. The successful perforated cell shows detectable fluorescence intensity, and intensity changes depend on amount of the internalized PI molecules and formed PI-nucleic acid complexes. The gradual increase and following decrease of the total intracellular fluorescence intensity indicate the pore formation and subsequent resealing process (shown by curve I and II in Figure 3.4). A severe perforated cell suffers from many PI-nucleic acid complexes (mostly in nucleus), and the fluorescence intensity continuously increases and indicates the dead cell (curve III and IV in Figure 3.4). In fact, the internalization continues for a longer period (from seconds to minutes) after the optoporation up to a full recovery of the cell membrane or an equilibrium condition between PI molecules and nucleotides [96].
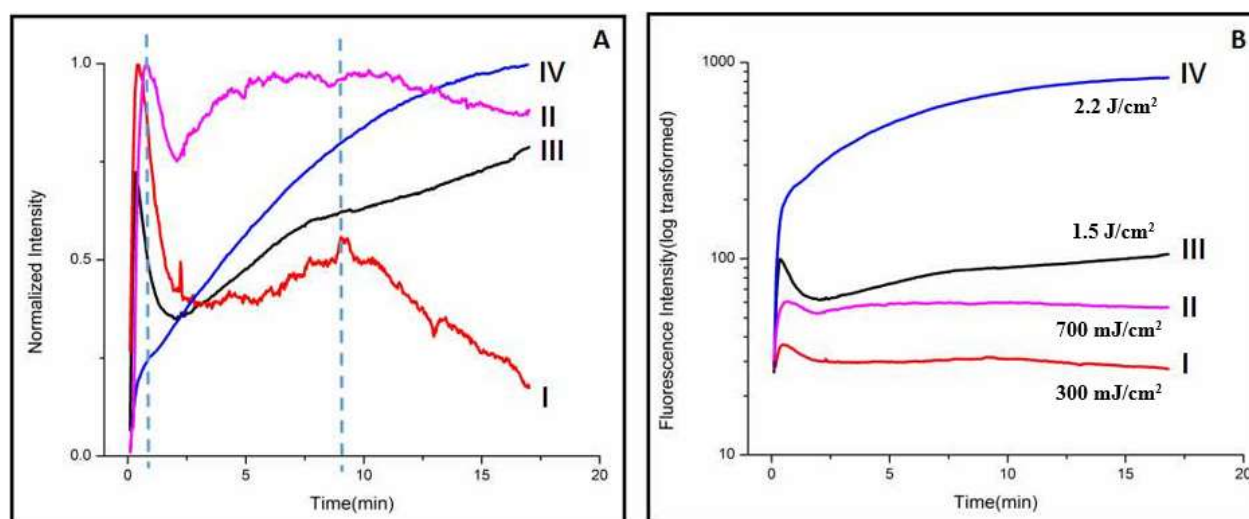
Figure 3.4 Typical dynamics of PI uptake and PI-nucleic acid binding diffusion in a cell after nanoparticle-mediated optoporation. A) shows the normalized fluorescence intensity to dynamic tendencies and relative intensity changes; B) shows a log transformation of the absolute

fluorescence intensity values without the normalization. I-IV demonstrates responses with different laser fluences.

To study the effect of laser fluence on the single cell optoporation, four different fluences (0.3, 0.7, 1.5 and 2.2 J/cm^2) were applied and corresponding internalizations and cell viabilities were shown in Figure 3.5. The laser fluences less than 700 mJ/cm^2 (Figure 3.5.I.A and B) did not affect the cell viability of the treated cells, while the higher fluences killed the cells (Figure 3.5.I.C). However, the optoporation was not observed for the fluence less than 300 mJ/cm^2. The real-time imaging system provided a quantitative visualization overview of the localized perforation (Figure 3.5.II). The highly localized perforation specifically revealed a strong red spot (PI emission fluorescence) compared to a normal cell without the optoporation. Moreover, the increase of the laser fluence to 700 mJ/cm^2 remarkably permeabilized the cell membrane and subsequently increased the internalization of PI molecules, and boosted red fluorescence (Figure 3.5.III). However, the treated cell was survived after 2 h post-irradiation based on Cal-AM cell viability analysis.
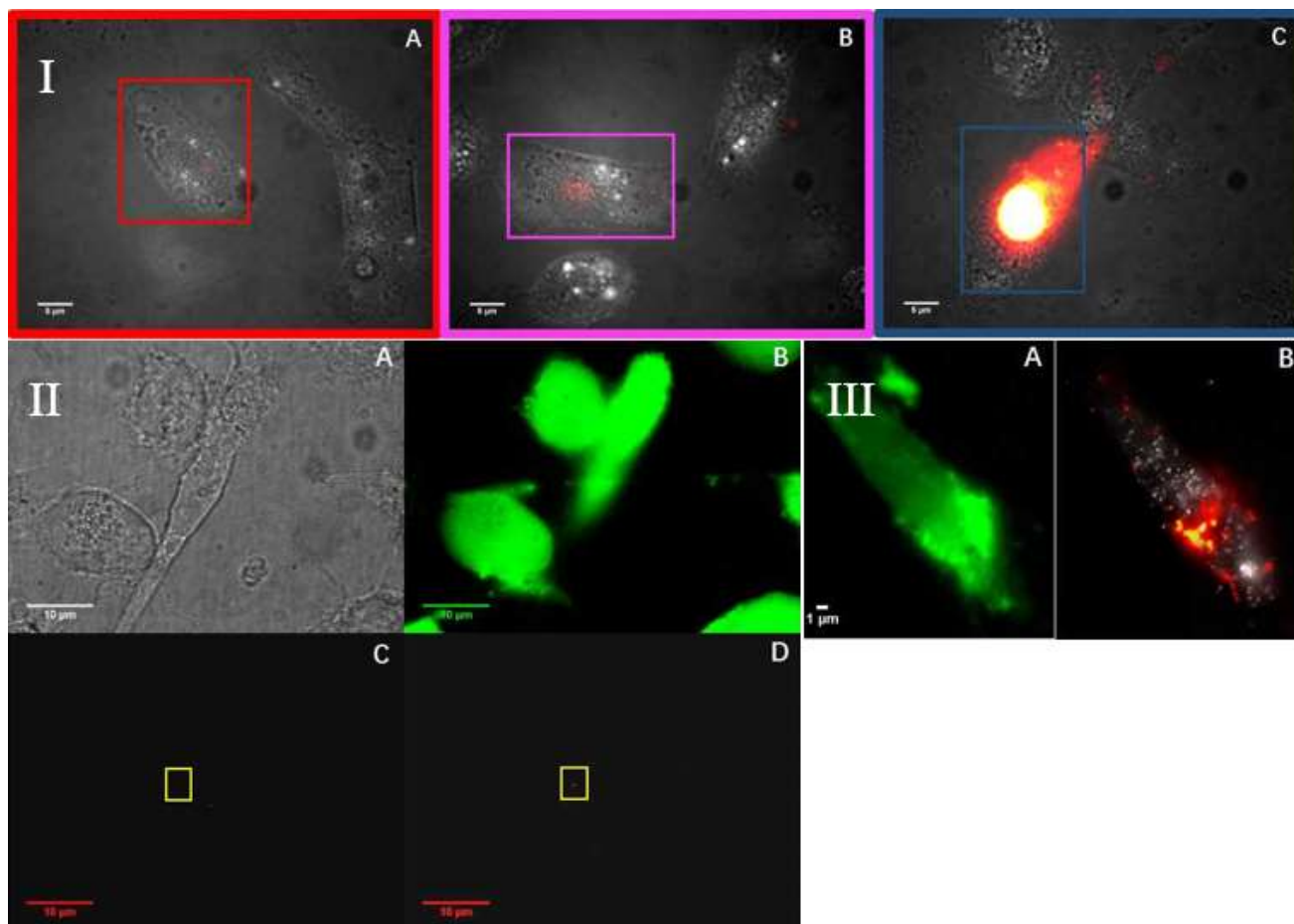
Figure 3.5 I) Combined imaging of cell transmission imaging and PI fluorescence imaging after laser irradiation. A) Laser fluence is between 200-300 mJ/cm^2; B) Laser fluence is between 300-700 mJ/cm^2; C) Laser fluence higher than 1.5 J/cm^2. Colored squares demonstrate the perforated cells. Scale bar is 5 μm. II) Cellular response with laser fluence lower than 300 mJ/cm^2. A) shows the transmission imaging of a single cell; B) Cal-AM fluorescence of the cells 2 hours post-irradiation; C) and D) demonstrate PI fluorescence imaging of the cell before and after laser irradiation. The yellow square indicates the irradiated area. Scale bar is 10 μm. III) Fluorescence imaging of a single cell with laser irradiation fluence around 700 mJ/cm^2. A) Cal-AM fluorescence of the cell; B) RLM of NP and PI fluorescence of the cell with excretion. Scale bar is 1 μm.

Different intracellular PI trafficking mechanisms occur after the second intensity peak for curve I, II and III. However, severe membrane damage causes a dramatic raise of the fluorescence intensity with no reduction (curve IV). The trends of the fluorescence intensity, the mechanism is divided into 5 regions by the vertical blue dashed lines (detailed in Table 3.1). Region 1 shows the fluorescence intensity before the laser irradiation. In region 2, the laser irradiation causes a raise of the intensity. The second and third regions (labelled curve I, II and III) follow the same trend before the second peak, and then an intensity drop, but the curve IV shows a constant increasing intensity due to an extensive perforation (1.5 J/cm^2).

Table 3.1 Schematic of the cellular post-irradiation responses to different laser fluences. There is no fluorescence intensity detection or cellular response before the laser irradiation (Region 1). In region 2, the dramatic increase of fluorescence intensity is related to the effect of the initial excitation and internalization of PI molecules into the locally perforated membrane. The nucleotides in the cytoplasm react with the internalized PI molecules, and quickly activate fluorescent responses (the initial intensity peak). This trend is the same for all four curves. In region 3 and 4, there is an intensity drop followed by another increase which is related to different mechanisms for curve I, II and III. For the intensity drop after the initial irradiation, 1) the membrane reparation stopped the internalization and 2) photobleaching of the PI molecules caused by the illumination. On the other hand, the intensity rise might be caused by a slow diffusion of big PI molecule-nucleic acid complexes. The free internalized PI molecules also enter into the nucleus and bind with nucleotides (second intensity peak). The fluorescent intensity mainly depends on the perforation of the membrane. At the low laser fluence the perforated membrane reseals by itself, the PI intensity gradually decreases due to the photobleaching (curve I in region

5). The saturation effect on curve II is also observed in region 5 due to the existed excretion of nucleotides from the damaged cell [97] during optoporation which activates PI in the solution (Figure 3.5.III.B). Higher laser fluence would cause cell damage easily by necrosis [98] and many PI molecules could enter into the nucleus, causing cell death and giving bright fluorescence as curve III and IV in region 5.
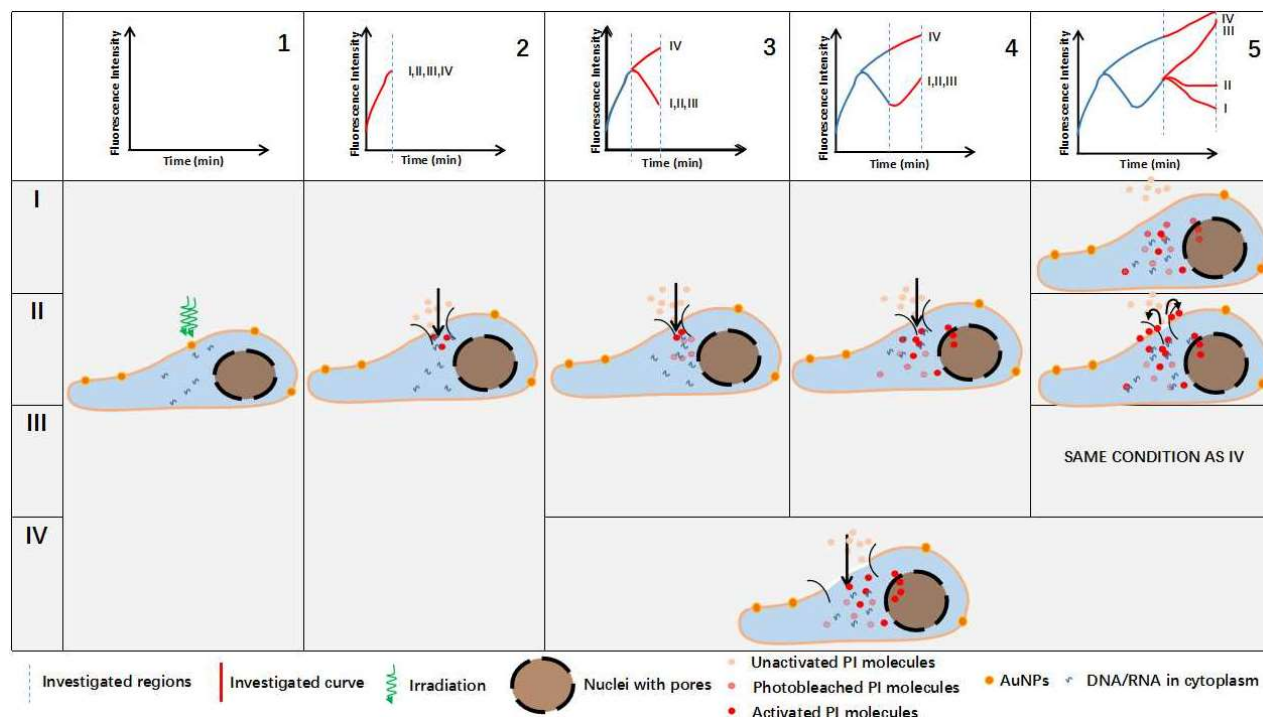
3.4.4 Effects of irradiation areas

Irradiation area on the cell membrane where to internalize PI molecules close to nucleus or far away is important because the internalized PI around the nucleus can extensively penetrate it [90]. Under same experimental conditions using laser fluence 695 mJ/cm^2, two irradiation locations, near and far from the nucleus, indicate different perforation mechanisms (Figure 3.6.I). The targeted cell (a laser beam located far away from the nucleus) shows a small internalization of PI molecules compared to the cell (a laser beam located close to the nucleus) that is fully affected by the internalization of PI molecules reacted with nucleotides (Figure 3.6.II and Figure 3.6.III). Moreover, the cell viability measured using Cal-AM (2 h post-optoporation) shows a cell death for the laser beam located close to the nucleus in the comparison to the beam located far away.

I
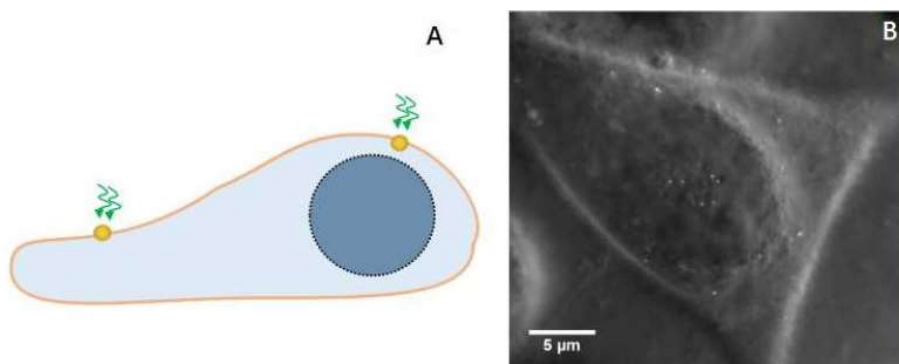
II
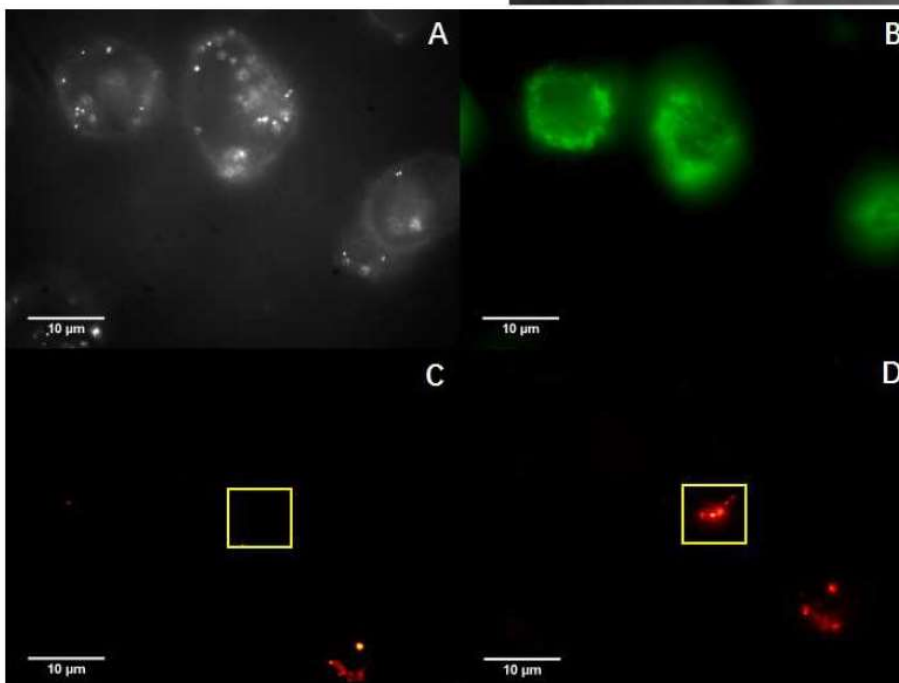
III
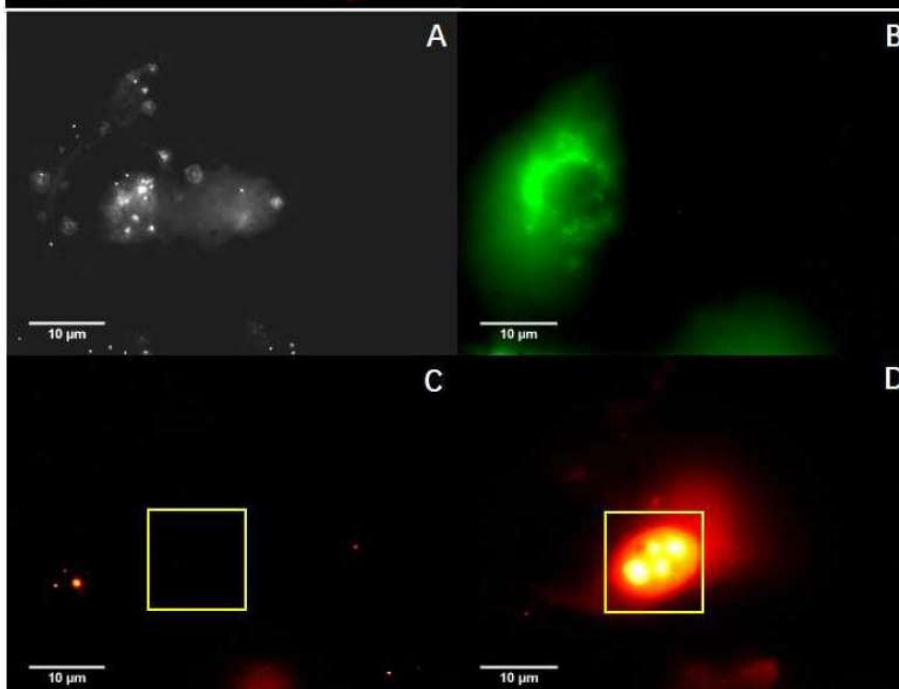
Figure 3.6 demonstrates the laser targeted cell on different locations. I.A) The schematic of different irradiation areas on the cell; B) pDF imaging of the cell and RLM imaging of NPs with visible nucleus. II) and III) are the laser irradiation are far from and close to the nucleus respectively: A) RLM imaging of NPs on cell membrane; B) Cal-AM fluorescence imaging 2 h post-irradiation; C) and D) PI fluorescence imaging before and after the laser irradiation. The yellow square is the irradiated area.

In conclusion, the pulsed laser single cell optoporation paves the way to understand the mechanisms of cell membrane damage by monitoring and recording the exogenous biomolecules inflows.

CHAPTER 4   ARTICLE 1: COST-EFFECTIVE SIDE-ILLUMINATION DARKFIELD NANOPLASMONIC MARKERS MICROSCOPY

This Chapter is a transcription of the article published for publication in Analyst (Royal Society of Chemistry (RSC) Publishing). It demonstrates a well-designed and fabricated illumination device with arrayed LEDs inserted along the sample slide, providing feasibility to adapt on any microscopes with high contrast NPs in diferent cellular environments. Amoslt all experiments, developments and optimizations were fulfilled by myself. Dr. Sergiy Patskovsky kindly helped me to design and develop the prototype of the illumination device and offered crucial experimental and theoretical suggestions and recommendations. Ms. Cecile Darviot kindly assisted me to culture Y79 cancer cells. This study was supervised by Prof. Michel Meunier.

4.1 Authors

*Mengjiao Qi, *[a] Cecile Darviot, [a] Sergiy Patskovsky, [a] and Michel Meunier [a]*

[a] Department of Engineering Physics, Polytechnique de Montreal, Quebec, H3T 1J4, Canada

4.2 Abstract

We present the development of an innovative technology for quantitative multiplexed cytology analysis based on the application of spectrally distinctive plasmonic nanoparticles (NPs) as optical probes and on cost-effective side-illumination multispectral darkfield microscopy (SIM) as the differential NP imaging method. SIM is based on lateral illumination by arrays of discrete color RGB light emitting diodes (LEDs) of spectrally adjusted plasmonic NPs and consecutive detection by the conventional CMOS color camera. We demonstrate the enhanced contrast and higher resolution of our method for individual NP detection in the liquid medium and of NP markers attached on the cell membrane in a cytology preparation by comparing it to the conventional darkfield microscopy (DFM). The proposed illumination and detection system are compatible with current clinical microscopy equipment used by pathologists and can greatly simplify the adaptation of plasmonic NPs as novel reliable and stable biological multiplexed chromatic markers for bio detection and diagnosis.

KEYWORDS: Plasmonic nanoparticles, darkfield microsopy, RGB light emitting diodes, side-illumination multispectral darkfield micriscopy.

4.3 Introduction

Over recent years, tremendous efforts have been invested in designing novel nanoparticle (NP) probes with unique properties that are advantageous for use in biochemical diagnostics and disease treatment[99, 100]. The NP probes most widely used in diagnostic applications are quantum dots (QDs), polymer dots (PDs), upconversion nanoparticles (UCNPs), and plasmonic nanoparticles (NPs)[101].

The unique optical and physical properties of plasmonic NPs, their proven photo-stability, water solubility and biocompatibility provide new opportunities and open new fields of biomedical application ranging from using NPs as a targeted drug carrier or gene deliverer to cancerous cells, to using NPs as a biological immunomarker agent in biomedical diagnostics and disease treatment[102-105]. An outstanding example is the use of spectrally tunable NPs as optical multiplexing biomarkers for selective cell and tissue labelling[106, 107]. This multiplexed method could notably show several advantages for cytology applications. Currently, in cytology specimen analysis, pathologists heavily rely on immunohistochemistry (IHC) to increase the accuracy of their diagnosis[108]. Multiple preparation steps have to be performed to color these proteins, which can destroy the proteins and therefore strongly reduces the reliability of the technique. It is also impossible to assess the relative expression of multiple antibodies (Abs) at the single cell level, which is important for a reliable diagnosis. There is a need for a cost-effective, sensitive and specific diagnostic methodology to overcome the limitations associated with conventional IHC based methods. We think that a methodology based on a new cytology protocol, where immunolabeling by plasmonic NPs[109, 110] is performed on fresh cells before fixation can improve diagnostic reliability.

To promote user adoption of this new method in cytopathology laboratories, the NP imaging hardware should be compatible with equipment currently used in laboratories, and the sample preparation and imaging procedure should not involve additional steps or risks of contamination to the sample compared with the existing procedure. This currently represents a challenge with plasmonic NP markers, as the optical detection of plasmonic

NPs typically relies on the scattered light by NPs detected in a darkfield microscopy (DFM) mode. Although there are on the market hyperspectral microscopes with a darkfield condenser to detect and differentiate NPs with a very high resolution (e.g.: CytoViva, Photon Etc.), they are costly, require considerable changes to the conventional microscopy system, and are therefore impractical in clinical settings. Recently, we proposed a widefield hyperspectral 3D imaging of cell-NPs[93] with reflected light microscopy (RLM)[94] which overcomes the numerical aperture (NA) limitations of darkfield imaging and provides enhanced contrast of NP imaging in cellular environment. However, the RLM requires high NA immersion objectives with matching oil that contaminate histopathology and cytology microscopy samples and limit widespread application.

In this article, we propose to use a multispectral side-illumination darkfield microscopy (SIM) method that allows designing and fabricating a compact microscopy module for optical imaging and spectroscopic identification of individual plasmonic NPs in fixed or live cell preparations. This method employs darkfield NP imaging with lateral optical illumination[111, 112] that removes the inherent limitations on the NA of the imaging objective used for the conventional darkfield microscopy and provides an enhanced contrast of plasmonic NPs in the diffusing medium, cellular membrane and extracellular matrix. By using recent light emitting diode (LED) technology for side-illumination, the dimension of the proposed microscopy module can be comparable with the conventional histopathology sample holder. This compact side-illumination module can provide a convenient and routine method for immunoplasmonic markers visualization by cytopathologists. It can be easily adaptable to the microscopes currently used in the clinical setting thus facilitating and accelerating its adoption.

4.4 Experimental

4.4.1 Cell culture

To image NP mixture in cellular environment, we cultured adherent MDA-MB-231 human breast cancer cells and suspension Y79 human retinoblastoma cells.

MDA-MB-231 cells (ATCC® HTB-26™) were grown in Dulbecco's Modified Eagle's Medium (DMEM) containing 10% fetal bovine serum (FBS, Life Technologies) and 1% penicillin and streptomycin (PS, Invitrogen) and cells were removed by trypsinization and

seeded onto microscopic slide with help of a self-insertion well from Ibidi. When the cells reached ~80% confluence, they were incubated with a NP mixture for ~3 hours in an incubator and then washed 3 times with phosphate-buffered saline (PBS, Sigma-Aldrich), fixed with cold methanol for 5 minutes and washed another 3 times with PBS. Then the self-insertion well was replaced by the coverslip (SPI Supplies) on top of the slide.

Y79 cells (ATCC® HTB-18[TM]) were cultured in RPMI 1640 (Life Technologies) containing 10% FBS (Life Technologies) supplemented with 1% PS. The NP mixture was incubated with Y79 cells for 3 hours before centrifugation at 200g for 7 minutes. The NP mixture incubated Y79 cells were then sprayed on a slide coated with poly-L-lysine and covered by a coverslip.

4.4.2 Plasmonic nanoparticles

For both individual or multiplexed NPs detection applications shown in this article, we used 70nm silver (Ag) spherical NPs (Ted Pella Inc.), 50nm, 60nm and 80nm gold (Au) spherical NPs (Nanopartz), and 40 x 80nm gold nanorods (AuNR) (Nanopartz).

The NPs were placed in different environments to prepare the samples: in homogeneous low-scattering PBS medium and in a high-scattering cellular environment filled with Vectashield Antifade Mounting Medium. We used conventional 25x75 microscopy slides as a substrate with thin 0.13-0.17 μm coverslips.

4.4.3 Side-illumination microscopy adaptor.

The main principle of the side-illumination darkfield method is shown in Figure 4.1.A and the schematic of the light beam propagation is presented in Figure 1 of the ESI.† Figure 4.1.B shows a technical schematic of the microscopy module with lateral LED illumination. Two types of microscopy adaptors optimized for inverted (Figure 4.1.C) and upright microscopes (Figure 4.1.D) were designed by us and fabricated by VegaPhoton. The adaptors were fabricated with aluminum CNC machining to obtain the precision and rigidity required for use with professional microscopes. To simplify integration, in the case of the inverted microscope, the adaptor was integrated into a ProScan™ flat top inverted microscope motorized stage (Prior Scientific, Inc.) that allows fine 3D spatial sample translation. For the conventional upright microscope, the adaptor thickness was designed to

be only 5.4 mm for seamless integration with the existing transmission illumination setup and to avoid hinder to the objective free run. The narrow RGB LED array (2.8 x 0.35 x 0.85, Citizen CL246) is mounted on a PCB card compatible with both inverted and upright microscopes and placed in close optical contact with both sides of the standard microscope slides used in histo- and cyto-pathological analysis, as shown in Figure 4.1.B. Typical emission spectra of the RGB LED are shown in Figure 4.2.A.
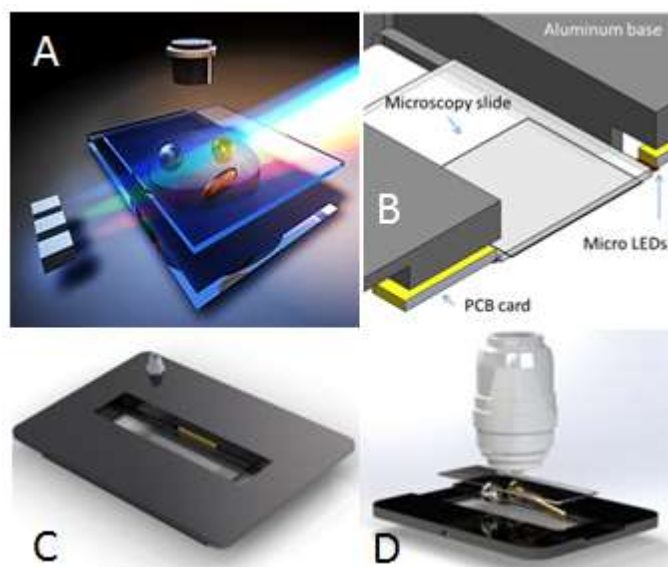
Figure 4.1 A) Principle of the side-illumination darkfield technique. B) Schematics and C) experimental prototypes of the darkfield microscopy with side LED illumination designed for inverted and D) upright microscopes.

The manual or automatic power control of illumination intensity for individual color LEDs provides a possibility for direct visualization of multiple plasmonic biomarkers placed in the medium or on the cellular membrane. Automatic LED intensity control is very useful for the development of the digital NP imaging and detection using a fast CMOS color or monochromatic camera and sophisticated image treatment software. Another advantage of the proposed microscopy adaptor is in the simplicity of switching between the conventional transmission mode already used by pathologist and the darkfield side-illumination mode and, especially, the possibility to use them together, thus generating more relevant information about investigated samples.
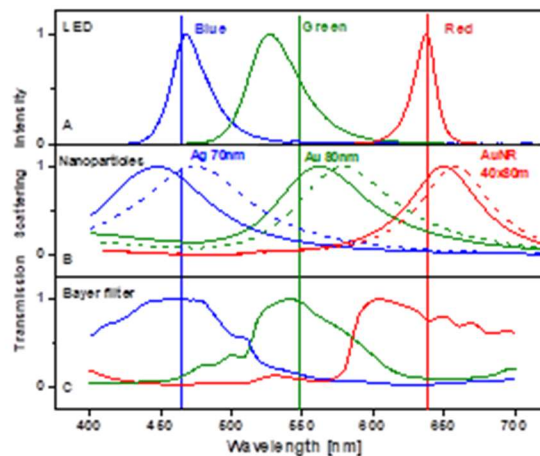
Figure 4.2 Resonance peaks of NPs are selected to fit the spectral emission of the color LED used for lateral illumination and to the imaging camera detector filters. A) CL246 LED spectral emission properties. B) Scattering properties of 70 nm Ag NPs, 80 nm Au NPs and 40x80 nm Au NRs in PBS (solid line) and in Vectashield mounting medium (dashed line). C) Transmission spectral profiles of CMOS camera Bayer filters

4.5 Results and discussion

4.5.1 Side-illumination darkfield multispectral plasmonic NP microscopy.

The proposed SIM method and corresponding microscopy module are based on four complementary technologies, in order to provide a high resolution and high contrast NP imaging in the complex medium and facilitate integration into existing optical systems.

The first technology is a darkfield microscopy technique based on lateral illumination[111, 113, 114]: this method resides in excluding the non-scattered light from the output image by using an illumination orthogonal to the imaging lens optical axis. This approach is optimal for darkfield NP imaging contrast and what is also important is that it removes the inherent limitation on the NA of the objective which has to be smaller than the NA of the illumination condenser in the conventional transmission darkfield mode. The second technology is an application of the recent development in discrete color LEDs specifically designed and optimized for lateral illumination of thin glass substrates (<400 µm). Such LEDs can be directly put in close optical contact with standard microscope slides and coverslips. The third technology is based on the multiplexing abilities and unique resonance properties of metallic NPs, which demonstrate an enhanced scattering efficiency compared to the cellular membrane. Furthermore, the possibility to tune NP plasmon peak to the maximum intensity of the illuminating LED source allows improving the efficiency of NP chromatic differentiation. The fourth technology relies on the introduction on the market of low-cost, fast and sensitive CMOS cameras. Such cameras in combination with corresponding image treatment software serve as the basis for the automatic multiplex NP detection, spatial localization and spectral differentiation.

As follows from the above description, the most efficient NP detection system will use matching and as narrow as possible spectral characteristics of LED sources, imaging camera filters and plasmonic NP scattering spectra. However, while it is possible to build such a system with the available technology, the cost-efficiency aspect introduces certain limitation on the optical design. In this work we are using freely available on the market RGB lateral illumination LEDs in combination with a compact low-cost color CMOS camera (Ximea). Integrated into the camera Bayer filters provides a relatively large spectral range still giving the opportunity for the multiplexing.

Resonance properties of the plasmonic NPs can be readily tuned to the optimal peak position by changing the material, composition, size and geometry. However, a reliable NP detection by the darkfield method imposes a limitation on the scattering efficiency that directly depends on the NP size. That is why in this work we are using sufficiently large NPs for the multiplexing: 70 nm Ag, 80 nm Au, and 40 x 80 nm AuNR. In Figure 4.2 we show theoretical scattering spectra for our choice of NPs placed in the two most used media for

the visualization: PBS buffer with a refractive index (RI) of 1.34 and mounting medium with RI=1.45. As we can conclude from the figure, the spectral position of the 80 nm Au NPs in particular is far from the optimal but taking into account NP scattering efficiency and CMOS camera sensitivity these NPs can be spectrally differentiated as we show below.

4.5.2 Multispectral plasmonic NP imaging in homogeneous medium

The SIM method using our portable adaptor for an inverted microscope (Figure 4.1.C) was initially used to test the efficiency of the approach in the comparative study with conventional transillumination DFM (Nikon). Plasmonic NPs were placed on the microscopy slide in the PBS buffer drop and covered by the thin coverslip through the 200 μm spacer. Objective 60x, 0.7 NA was used for the imaging and a Nikon darkfield condenser (NA 0.8-0.95) was used for the conventional darkfield setup. All RGB LEDs were illuminated for the side-illumination adaptor. In Figure 4.3 we present results for the detection of Au NPs with different sizes. In the same images we also show a local scattering intensity distribution that allows us to compare experimental signal to- noise ratio and NP contrast obtained by these two optical methods. As we can conclude from these figures even for the smallest 50 nm Au NPs, that we are considering as the limit for the reliable NP detection, side-illumination mode provides a higher contrast and thus is more performant and has the potential for a reliable NP detection. The obvious NP color difference is explained by the different illumination sources: RGB LEDs for side-illumination and halogen for darkfield method.

For the next experiment, we prepared a 1 x 1 x 1 mixture of three NPs optimal for the SIM mode: 70 nm Ag NPs (spectral peak 450 nm), 80 nm Au NPs (spectral peak 560 nm) and 40x80 nm Au NRs (spectral peak 650 nm). Obtained color images are shown in Figure 4.4. All three individual NPs in the homogeneous PBS solution can be discriminated in different scattered colors even by visual observation.

However, a more reliable differentiation method can be proposed by controlling illumination intensities of different LEDs. For example, only Ag NPs were detected with an individual LED blue channel on and both Ag and Au NPs were visualized with blue and green channels on, as presented in Figure 4.4.B and C. Au NRs can be subtracted from the NP mixture image taken with all LEDs on, as shown in Figure 4.4.D.
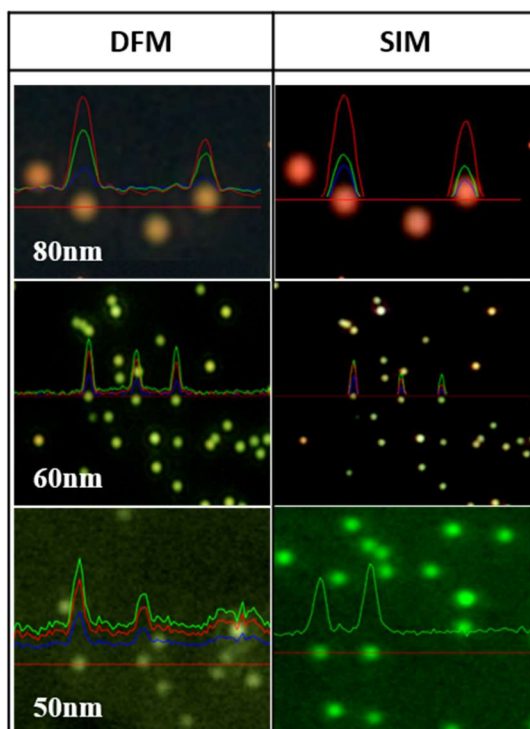
Figure 4.3 Comparative conventional darkfield microscopy (DFM) with Nikon darkfield condenser (left column) and side-illumination microscopy (SIM) (right column) detection of Au NPs samples with different sizes (80 nm, 60 nm, 50 nm). NPs in the PBS buffer between conventional microscopy slide and thin coverslip. Objective 60x, 0.7 NA.

4.5.3 Plasmonic NP imaging in cell-NP complex.

And finally, we are presenting the most important results of multiplexed NP visualization. Different cell lines with different sizes and properties were nonspecifically decorated with plasmonic NPs and observed by the proposed SIM mode and DFM mode for comparison.

Firstly, we prepared a cytology sample with MDA-MB-231 that is a highly aggressive, invasive and poorly differentiated triple-negative breast cancer cell line. Triple-negative breast cancer is an aggressive form of breast cancer with limited treatment options. Understanding the molecular basis of this cancer is therefore crucial for effective new drug development and as a result many studies on potentially active agents for this particular type of breast cancer have been conducted using the MDA-MB-231 cell line (PHE Culture Collections)[115, 116]. MDA-MB-231 cells are rather large (up to 30 μm) adherent cells.

They were mixed with our three types of NPs and placed in the Vectashield antifade mounting medium.

Retinoblastoma is a rare childhood cancer of the eye that can begin *in utero* and is diagnosed during the first few years of life. To date, two human retinoblastoma cell lines, Weri1 and Y79, are widely used in research. Y79 cell-line is suspension cells with small dimensions (10-12 μm diameter) and two markers on the membrane can be selectively labelled by plasmonic probes: MRC2 and CD209[117]. We have prepared a second type of cytology samples with a Y79 cell–NP complex placed in the mounting medium.

As was shown in the literature[118, 119], the influence of the cellular environment on the quality of the conventional darkfield optical detection of the forward scattering light makes image interpretation and NP visualization in the cellular environment quite complicated or even impossible (Figure 2 in the ESI†). However, our experimental results obtained with a SIM setup showed drastic improvement for the NP visualization in the cellular environment compared to the conventional darkfield mode. In Figure 4.5, we present the images of MDA-MB-231 and Y79 cells decorated with different NPs where high NP contrast allows reliable spatial and spectral detection even by direct visual observation. This is not the case for the DFM where high cellular scattering block NPs. This phenomenon is more obvious for smaller Y79 cells making NP differentiation and even detection impossible.

NP spatial distribution and spectral differentiation in a cellular environment are main parameters for using NPs as multiplexed biomarkers to target specific cells in biomedical applications and our results show good potential for the SIM method to provide reliable information.

The side-illumination adaptor imposes no limitation on the objective NA, so we can increase the NA up to 0.95. Results of the SIM image of cells-NP complex taken with objective 60x, 0.95 NA with the corresponding local 3D NP intensity patterns confirm high contrast of NPs placed on the cell membrane (Figure 4.6).

Such advantages of the SIM method are very useful for the application of localizing the NP position in the 3D space. Enhanced spatial resolution especially in the z-direction is provided by the objective with a high NA and the experimental result of dynamic 3D NP scanning is attached in ESI Video. †

Our microscopy approach has significantly lower NP multiplexing capabilities than continuous scanning hyperspectral systems. However, considering a much lower cost, simplicity of integration and utilization in the fields where three plasmonic markers can provide adequate information, SIM has very good industrial potential. Also, a continuous advancement of the microelectronic technology will provide new more efficient and spectrally variable LED light sources and imaging detectors with tunable filters that will contribute to the performance of SIM technology.

This compact side-illumination module presented in this work can provide a convenient and routine method for immunoplasmonic marker visualization by the pathologist.
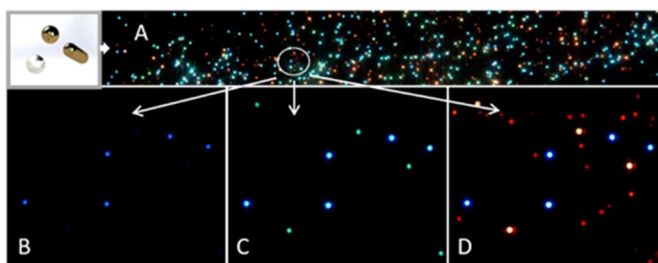
Figure 4.4 A) Example of NP mixture on a coverslip visualization with SIM microscopy. B) Magnified Ag NPs imaging with only blue LED, C) Ag and Au NPs imaging with blue and green LEDs, D) Ag, Au, Au NR mixture imaging with all LEDs. Objective 60x, 0.7 NA.
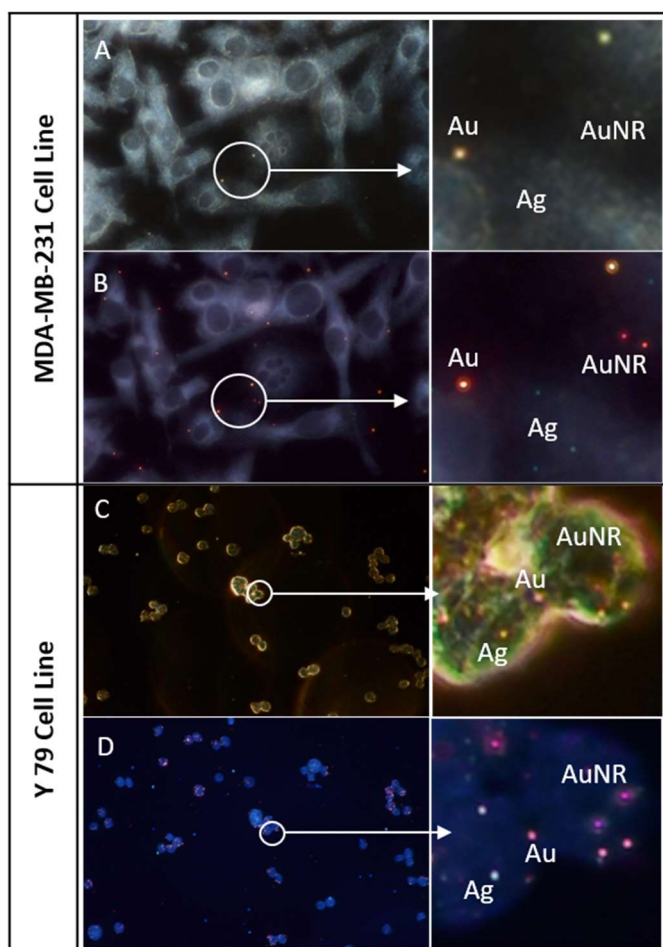
Figure 4.5 Cell-NP complex imaging by DFM A), C) and SIM B), D). Adherent cell line MDA-MB-231 A), B) and suspension cell line Y79 C), D). Insets show a magnified view of the selected area

However, to achieve this goal, it is necessary to develop the corresponding hardware architectures and software algorithms, which will automatically detect positions, types and concentration of the immunoplasmonic markers using a multispectral data cube. As the result the SIM method could serve as the basis for the whole slide imaging (WSI) automatic system[120]. Such a system will enable pathologists to read slides digitally, helps to visualize/identify new immunoplasmonic biomarker signatures and to develop early diagnosis and effective therapeutic intervention tools. The inherent stability of immunoplasmonic biomarkers (noble metal NPs preserve their plasmonic properties for a long time) can be considered as an advantage as the time between labelling and digitization became not critical.
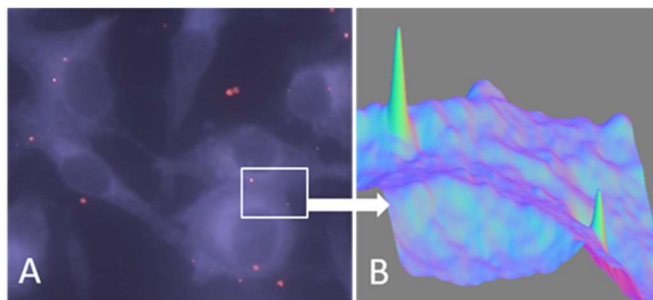
Figure 4.6 A) SIM image of cells-NP complex taken with objective 60x, 0.95 NA. B) corresponding 3D intensity patterns show high contrast of NPs placed on the MDA-MB-231 cell membrane.

4.6 Conclusion

Side-illumination plasmonic nanoparticle microscopy (SIM) has several advantages such as high optical contrast for individual NP imaging, precise 3D NPs localization due to the high NA objectives, possibility of the visual and software-based NP chromatic differentiation, and simple integration on any upright or inverted microscope preserving original functionalities. Pathologists and cytologists would benefit from this cost-effective, portable and functional side illumination setup for their request of real-time diagnosis and test. Combined with the technique of specific antibody functionalized NPs selectively targeting diseased cells, our SIM system can provide a cost-effective, compact clinically relevant approach for quick diagnosis and high efficiency therapeutic treatment.

4.7 Acknowledgement

CHAPTER 5 PLASMONIC NANOPARTICLE MEDIATED FEMTOSECOND LASER JURKAT CELL OPTOPORATION

This Chapter details femtosecond laser manipulation of Jurkat cells (an immortalized line of human T lymphocyte cells), which are used to study leukemia, solid-state cancers, and HIV (Human Immunodeficiency Viruses) infection [121-123]. In this Chapter, aiming at different applications (the sorting and the optoporation) of Jurkat cells, they are studied either bare or decorated with AuNPs for femtosecond laser optoporation.

5.1 The proposed approach

Transfection of suspension cells such as Jurkat cells by using the femtosecond laser irradiation is functional for most of biomedical applications; however, it is tricky owing to 1) the small size of Jurkat cells, 2) the floating nature of the cells, 3) the fragility of the Jurkat cells [124-126].

We here propose to deliver PI molecules (as a fluorescence marker of cellular uptake) into the Jurkat cells through the use of the femtosecond laser optoporation. To find a suitable range of femtosecond laser fluences for an effective optoporation, the floating Jurkat cells were immobilized on the petri dish substrate. By employing the laser scanning in a parallel mode on the immobilized Jurkat cells, the effective laser fluence range is confined to a specific range from 32 to 252 mJ/cm^2. Subsequently, after optimizing the functional range of the laser fluence, the Jurkat cells were cultured in the floating condition, in order to be perforated one by one. To scale up the production of the optoporated Jurkat cells with high viability and materials-delivery efficiency, the whole optoporation setup was further modified by replacing the petri dish by a microfluidic channel slide for constant suspension cells supply. It is planned to adapt the side-illumination device for the simplicity of NPs visualization for the microfluidic channels slide and reshape the laser beam profile to a few millimeters scale line for homogeneous laser energy distribution to scan the suspension cells. The individual part of the proposed approaches is performed, and the integration of all parts have been put into the future work (Appendix B: Modifications of femtosecond laser setup for the optoporation of Jurkat cells).

5.2 Methodology

5.2.1 Cell sample preparation

Jurkat cells were cultured using RPMI-1640 medium, properly supplemented with 10% of FBS and 1% of PS. For the preliminary laser fluence parameters test, the cells were cultured two days before the experiments with the final density of 10^4 cells/mm^2 to cover the petri dish substrate (diameter 35 mm, MatTek). On the day of the experiment, samples containing Jurkat cells were incubated with 100 nm AuNPs (with a concentration of 5.71×10^9 NP/ml and the number ratio of NPs and cells is 2×10^4) for 2 h, followed by two centrifugation steps (7 min, 200 g) to eliminate the free NPs. The centrifuged NPs-cell complexes were attached on the petri dish containing poly-l-lysine as the modified substrate. After the incubation for another 2 h, the sample with attached Jurkat cell samples were used for the laser irradiation with adding cell stain PI (final concentration is 2.73 µM) and Cal-AM (final concentration is 1 µM).

After finding a functional range of the laser parameters on the adherent Jurkat cells, we then cultured the suspending Jurkat cells in a petri dish (diameter 35 mm, MatTek) to optimize the laser irradiation parameters for the floating conditions. We explored the effects of different laser fluences on the perforation of Jurkat cells decorated without and with AuNPs (according to the same incubation protocol mentioned above). After the optional incubation step of AuNPs with the Jurkat cells according to the specific experiments (cell sorting and cell optoporation), PI and Cal-AM were added into the petri dish prior to the laser irradiation. The laser-induced localized macroscopic holes on the cells were visualized by the transmission imaging system. The generated microscopic holes on the cell membrane were indicated by the internalization of PI molecules, which can be fluorescence activated by the intracellular nucleotides. The cell viability was verified by Cal-AM, with esterase activated green fluorescence.
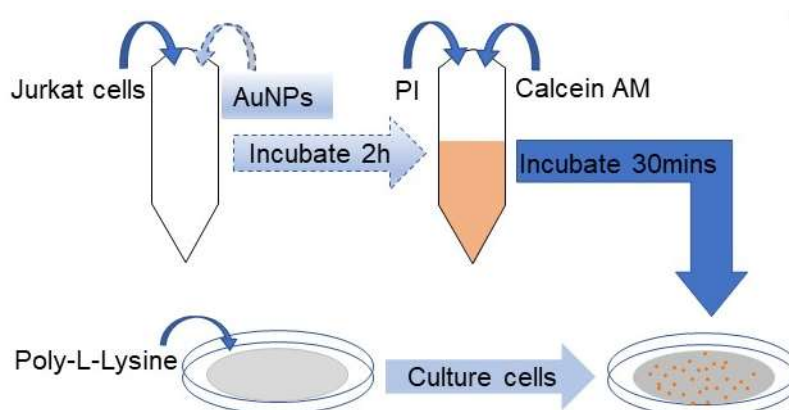
Figure 5.1 Demonstration of the cell sample preparation. Dashed arrows mean the alternative treatment for the sample preparation depending on different experiments (cell sorting and cell optoporation).

5.2.2 Optical setup

The experimental setup assembled for the femtosecond laser irradiation experiment is illustrated in Figure 5.2. It included a Nikon inverted microscope, equipped with a standard translation stage (Prior) to perform X-Y-Z 3D scanning of the treated sample. The standard QImage CCD camera and the fluorescence setup (X-Cite LED) were used to visualize NP-cell complex for doing the laser irradiation and verifying cell viability after the laser treatment.
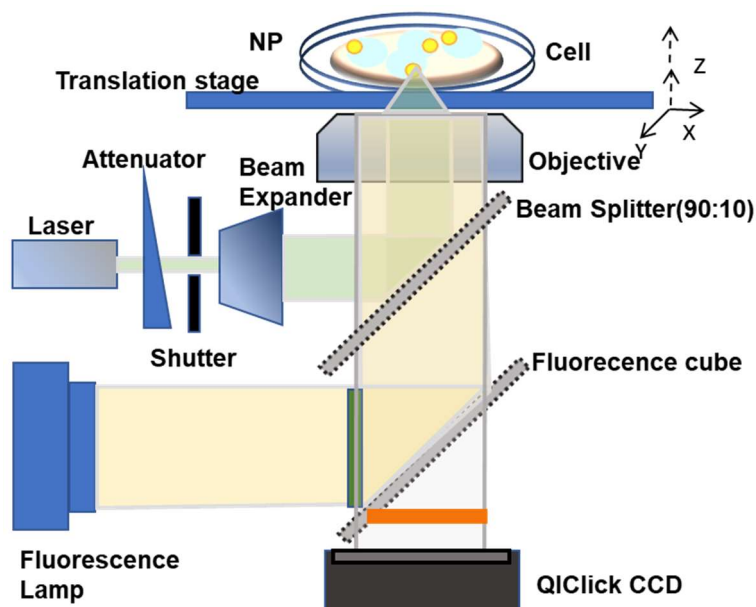
Figure 5.2 Schematic of the optical setup for femtosecond laser irradiation of the NP-cell sample in a petri dish.

The laser source used for the cell optoporation is an ultrafast 45 fs laser working at 1 kHz with a center wavelength of 800 nm (Spectra Physics). The laser power for the cell perforation was controlled by the pre-characterized motorized attenuator (Thorlabs). The duration of the laser irradiation was controlled by a mechanical shutter (Thorlabs) integrated into the LabView software. The whole optical setup was equipped with different NA objectives for different purposes, 20x objective for a large field of view imaging and 60x oil immersion objective for the backscattering imaging of NPs in the cellular environment. The visualization of NPs was achieved by the backscattering imaging technique. To observe NP-cell complex in a microfluid channel, we incorporated the side-illumination device within our microscope setup. Using a low NA objective provided a clear observation of the sample with a large field of view and high contrast image of NP-cell mixture in the microfluidic channel.

A translation motion stage was carried out to scan the Z direction as well as parallel X-Y field. All samples were then irradiated by the laser scanning in a parallel mode and the treated cells emitted reddish/greenish fluorescent colors after adding the cell viability stains. The setup was integrated with a portable incubator for the petri dish (37 °C and 5% CO_2).

5.3 Results and discussions

5.3.1 NPs attachment on the cell membrane

NPs were targeted on the cell membrane on a large scale, the supernatant (contain unbound NPs) was removed after the centrifugation (200 g, 7 min, and triple washing step) and then resuspended in the culture medium. Figure 5.3.A shows the spectrum of NPs in the NP-Jurkat cell mixture after each centrifugation step. When the AuNPs were incubated with the cells, the NPs concentration slightly reduced due to the dilution and slight aggregation of the NPs in the cell culture medium. After the first centrifugation, the supernatant of the NP-cell mixture was removed and resuspended in a culture medium and found out that the first centrifugation removed more than 40% of the NPs from the initial NP-cell mixture. For the second centrifugation, it removed another 10% of NPs from the NP-cell mixture and the third centrifugation did not show an obvious change of the NPs concentration in the supernatant. The obtained spectra indicate a suitable centrifugation (200 g for 7 min) and twice washing step to achieve an efficient NPs-Jurkat cell binding.
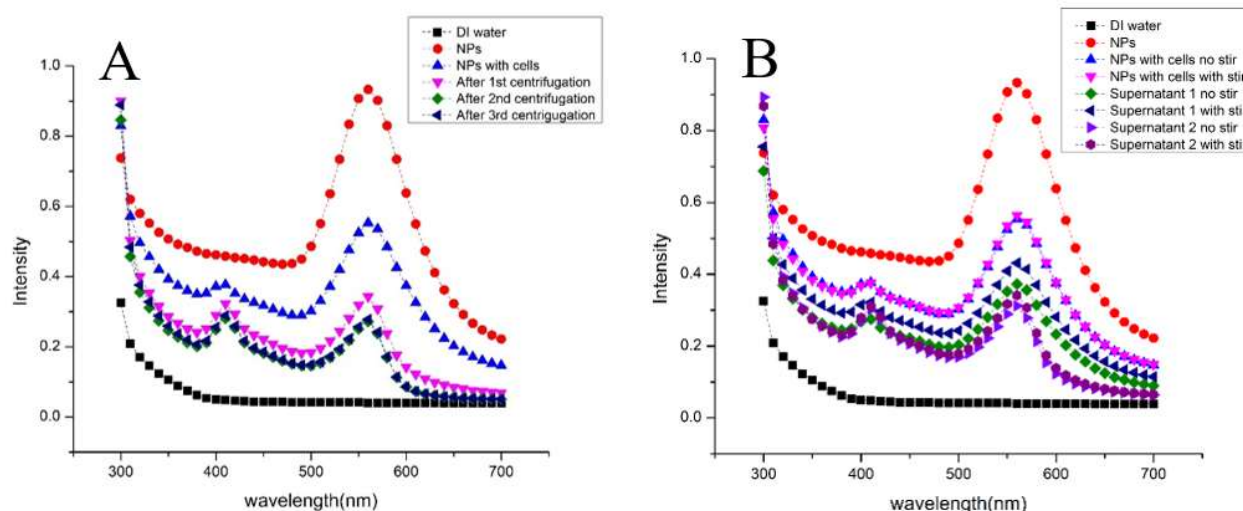
Figure 5.3 A) Spectrum of the NPs in the NP-Jurkat cell samples after three individual centrifugations. B) Spectrum of the NPs in the NP-Jurkat cell samples before the centrifugation and the NPs concentration in the supernatant after two individual centrifugations with and without the agitation. All tests were performed in the 96-well plate with the same volume of medium (200 µl). The spectrum of deionized (DI) water was given as a reference. The spectrum of the commercial NPs showed the plasmonic peak characteristic of the uniform NP distribution.

As NPs and Jurkat cells are floating in the culture medium during the binding procedure, the effect of the agitation rate is required to be evaluated in order to improve the binding of the NPs on the cell membrane. Figure 5.3.B shows the spectra of the NPs in the NP-cell mixture and in their supernatant after two individual centrifugations (200 g, 7 min). After adding NPs into the Jurkat cell suspension with and without the agitation, the concentration of the NPs decreased due to the dilution of NPs in the cell culture medium. After incubating the NPs with Jurkat cells for 2 h with and without agitation in the same condition, the spectra after the first centrifugation showed more NPs in the supernatant of the NP-Jurkat sample with the agitation. The second centrifugation slightly removed more NPs from cells into the supernatant with the agitation. After two individual centrifugations, the proposed magnetic agitation did not improve the affinity of NPs on the cell membrane

With the multifunctional optical setup, visualization and characterization of bound NPs on the Jurkat cell membrane were studied using the backscattering imaging (plasmonic NPs) and weak brightfield imaging (cell morphology). By analyzing the NPs attachment on 30 individual cells, the range number of NPs per cell is 4~7. Figure 5.4 shows a representative image of a single cell decorated by 5 individual NPs on the cell membrane. For the application of NP-Jurkat cells visualization in the microfluidic channel, our objective was transferred into a smaller magnification (20X) for a larger field of view, but the objective still provided enough contrast of NPs in the cellular environment (Appendix Figure B.2).
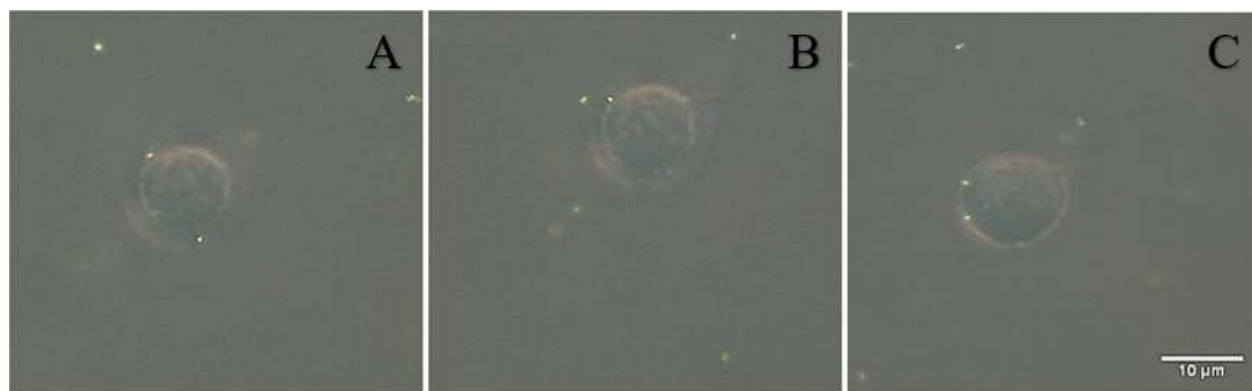
Figure 5.4 Backscattering imaging of the NPs attached on the Jurkat cell membrane with z-direction scanning. A), B) and C) show different levels of the cell membrane attached with NPs. On average, the NPs on the Jurkat cell membrane is around 5 NPs per cell. 60x oil immersion objective is applied for the NPs visualization.

5.3.2 Femtosecond laser treatment of Poly-L-Lysine attached Jurkat cells

Figure 5.5.I shows the femtosecond laser beam profile at the focal point by the image (Figure 5.5.I.A), with the analysis by fitting of the focus profile (Figure 5.5.I.B), the experimental laser focus diameter was achieved at around 11.3 μm.
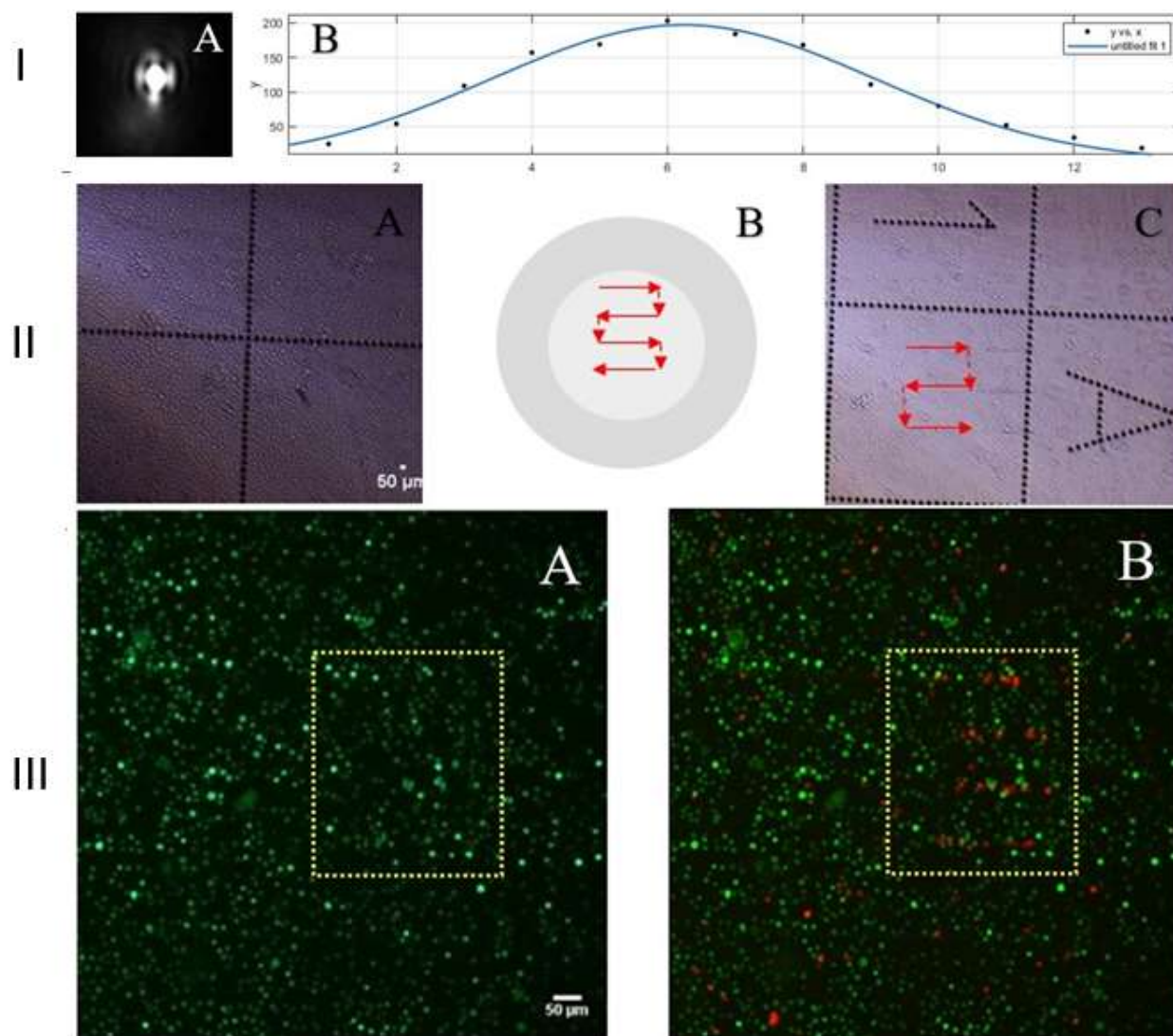
Figure 5.5 I.A) The image of femtosecond laser focal point with 20x objective for the irradiation application; I.B) Black dots are the experimental results from the image; The solid fitting curve is created using MatLab software. II.A) Brightfield imaging of Poly-L-Lysine attached cells on the substrate, for a large field of view, 10x objective is used for the imaging; II.B) Schematic of the X-Y parallel scanning of the cell sample in a Petri dish; II.C) The cells are irradiated by the laser. The dark lines beside the red arrows show the destroyed cells. Black round dots and black letters are the grids and the indications of the Petri dish. III)Fluorescent

imaging of femtosecond laser irradiated cell samples with the proposed parallel stepped scanning; III.A) The treated cells are alive with a fluence of 32 mJ/cm^2 and III.B) the treated cells are dead with a fluence of 252 mJ/cm^2; The irradiated area is in dotted yellow square.

The cell sample containing Jurkat cells in the petri dish on the polymers treated substrate was irradiated by the laser through a 20X objective, the laser fluence was controlled by a motorized attenuator. The laser treated cells were visualized with the laser fluence of 252 mJ/cm^2 (Figure 5.5.II.C) following a scanning pattern (Figure 5.5.II.B) on the polymer adhered Jurkat cells (Figure 5.5.II.A).

The viability test and optoporation were performed by adding PI and Cal-AM before the laser treatment to avoid the movement of the cell sample for the following analysis. The fluorescent images were taken 2 h after the laser irradiation. Different laser fluences were chosen from 1.3 mJ/cm^2 to 252 mJ/cm^2. The laser irradiation was at a scanning speed of 1000 µm/s with the step size of 10 µm. For the 1 kHz femtosecond laser, each individual cell received approximately 10 pulses shots with the laser focus with a diameter of 11.3 µm. Typical fluorescent results after the irradiation are shown in Figure 5.5.III. The adhered Jurkat cells, perforated using the fluence 252 mJ/cm^2, were killed, but the cells remained in good condition after the laser treatment at the fluence of 32 mJ/cm^2.

5.3.3 Femtosecond laser treatment of floating Jurkat cells without NPs

With the confined laser fluence range, Jurkat cell optoporation mediated by the femtosecond laser was performed in the floating status in order to be optimized for the future in vitro applications [127, 128]. The individual cell without NPs was irradiated by focusing the laser beam with a 20x objective at various fluences (32 to 252 mJ/cm^2) and durations to be performed and validated using the viability cell stains PI (2.73 µM) and Cal-AM (1 µM). Results are summarized in Table 5.1. Using the laser fluence 79 mJ/cm^2(10 ms), the fluorophores were visualized on the same cell 2 h after the laser treatment, and it indicated a successful perforation without affecting the cell viability. Increasing the laser fluence to 179 mJ/cm^2 (10 ms), the cell was totally dead (red PI fluorescence). At the laser fluence up to 73 mJ/cm^2, the cell viability did not change for different irradiation durations (10 ms, 50 ms and 100 ms). Probably because the dominant factor for the membrane rupture is the heating effect near the cell membrane caused by the femtosecond laser irradiation when there is no NPs decoration on the cell.

The femtosecond laser perforation of an individual cell without NPs shows a potential cell sorting application, eliminating the NPs decorated suspension Jurkat cells in the co-culture of bare Jurkat cells and NP-Jurkat cells.

Table 5.1 Cell viability results from the fluorescence of Jurkat cells without NPs decoration with different laser parameters.

	42 mJ/cm²	52 mJ/cm²	73 mJ/cm²	79 mJ/cm²	179 mJ/cm²	270 mJ/cm²
10 ms	No influence	No influence	No influence	PI and Cal-AM	Dead	Dead
50 ms	No influence	No influence	No influence	-NA	-NA	-NA
100 ms	-NA	PI and Cal-AM	No influence	-NA	-NA	-NA

5.3.4 Femtosecond laser treatment of floating Jurkat cells decorated with NPs

We prepared the NPs bound Jurkat cells in the petri dish (as described above in section 5.2). The experiments at different laser fluences (32 to 252 mJ/cm²) were performed on the floating Jurkat cells with a range number of 4~7 NPs per cell. The laser irradiation accompanied by the transmission imaging to provide a simultaneous observation and radiation. At the fluence of 78 mJ/cm², a visualized hole with a diameter size of 1.3 μm was generated on the cell membrane causing a cell death and increasing the fluence up to 252 mJ/cm², the cell was split (Figure 5.6). The generated macroscopic holes on the membrane can be one of the main causes of the cells' death. At the same time, cell viability stains (PI and Cal-AM) offer the cell perforation details.
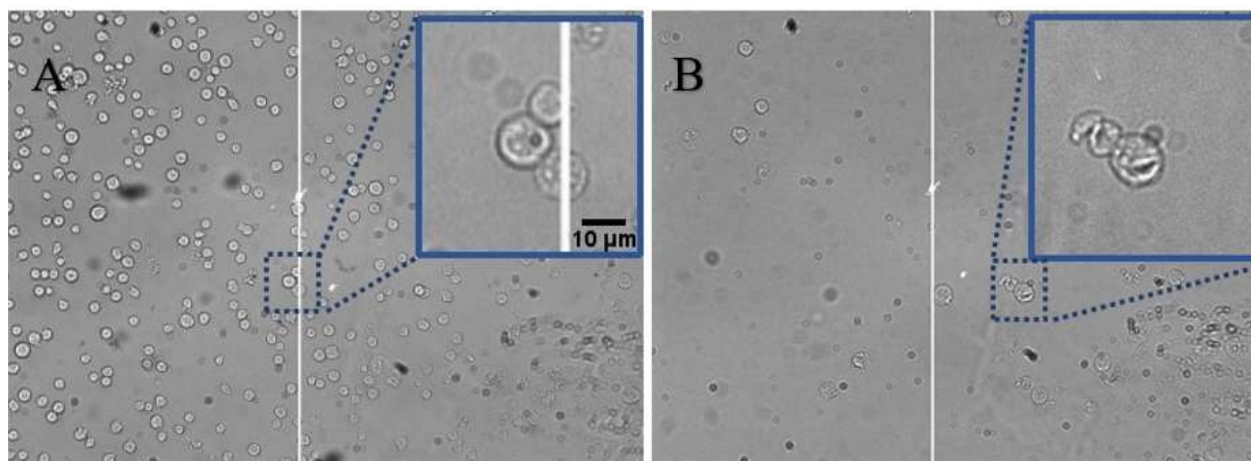
Figure 5.6 Suspending Jurkat cells floating in a Petri dish are irradiated with the femtosecond laser at a fluence of A) 78 mJ/cm^2 and B) 252 mJ/cm^2 respectively, introducing a hole on the cell membrane with a diameter size of 1.3 μm and cutting the cell into half. The solid white vertical line comes from the damage pixels of the camera.

Table 5.2 shows the resulted cell viability at various fluences and irradiation durations including 10 ms (10 pulses), 50 ms (50 pulses), and 100 ms (100 pulses). For the same laser fluence up to 56 mJ/cm^2, longer laser irradiation duration resulted in more damaging effect on the cell viability. For the same irradiation duration, the cell viability damage is more severe as the laser fluence increases. For instance, with 10 ms laser duration, until the laser fluence reaches to 63 mJ/cm^2, both fluorophores are visualized overlapping on the same cell, which indicates the cell is perforated successfully and the cell survives 2 hours after the laser treatment. The increasing laser fluence introduces the cell death indicated by the PI fluorescence exclusively.

Table 5.2 Cell viability of the NPs decorated suspension Jurkat cells after the laser irradiation with various laser fluences and irradiation durations.

	42 mJ/cm^2	56 mJ/cm^2	63 mJ/cm^2	71 mJ/cm^2	78 mJ/cm^2
10 ms	No influence	No influence	PI and Cal-AM	Dead	Dead
50 ms	No influence	Dead	-NA	-NA	-NA
100 ms	No influence	Dead	-NA	-NA	-NA

With the laser fluence of 56 mJ/cm^2 (10 ms), the live cell gave no red fluorescence (no internalized PI) and the treated cell showed a strong fluorescent signal (Cal-AM) after the irradiation (2 h), as shown in Figure 5.7.I. For the laser fluence of 63 mJ/cm^2 (10 ms), the PI fluorophores were internalized into the perforated cell. As shown in Figure 5.7.II, the cell was alive (shown by Cal-AM) before the laser treatment, But an intensity reduction of Cal-AM observed might be caused by leaching of fluorophores away through the generated holes after 2 h post-treatment [129]. The coexistence of PI and Cal-AM in the overlapped image verifies a successful perforation of the live cell [130-132]. The recovery of generated pores on the cell membrane limits fluxing in and out of the fluorophores. By increasing the laser fluence to 71mJ/cm^2 (Figure 5.7.III), the cells internalized plenty of PI molecules, which quickly stained the whole cell (around 10 mins). The cell membrane was irreversibly and dramatically permeabilized and this process led to a cell death (a significant leak of Cal-AM caused a green fluorescent signal lost).
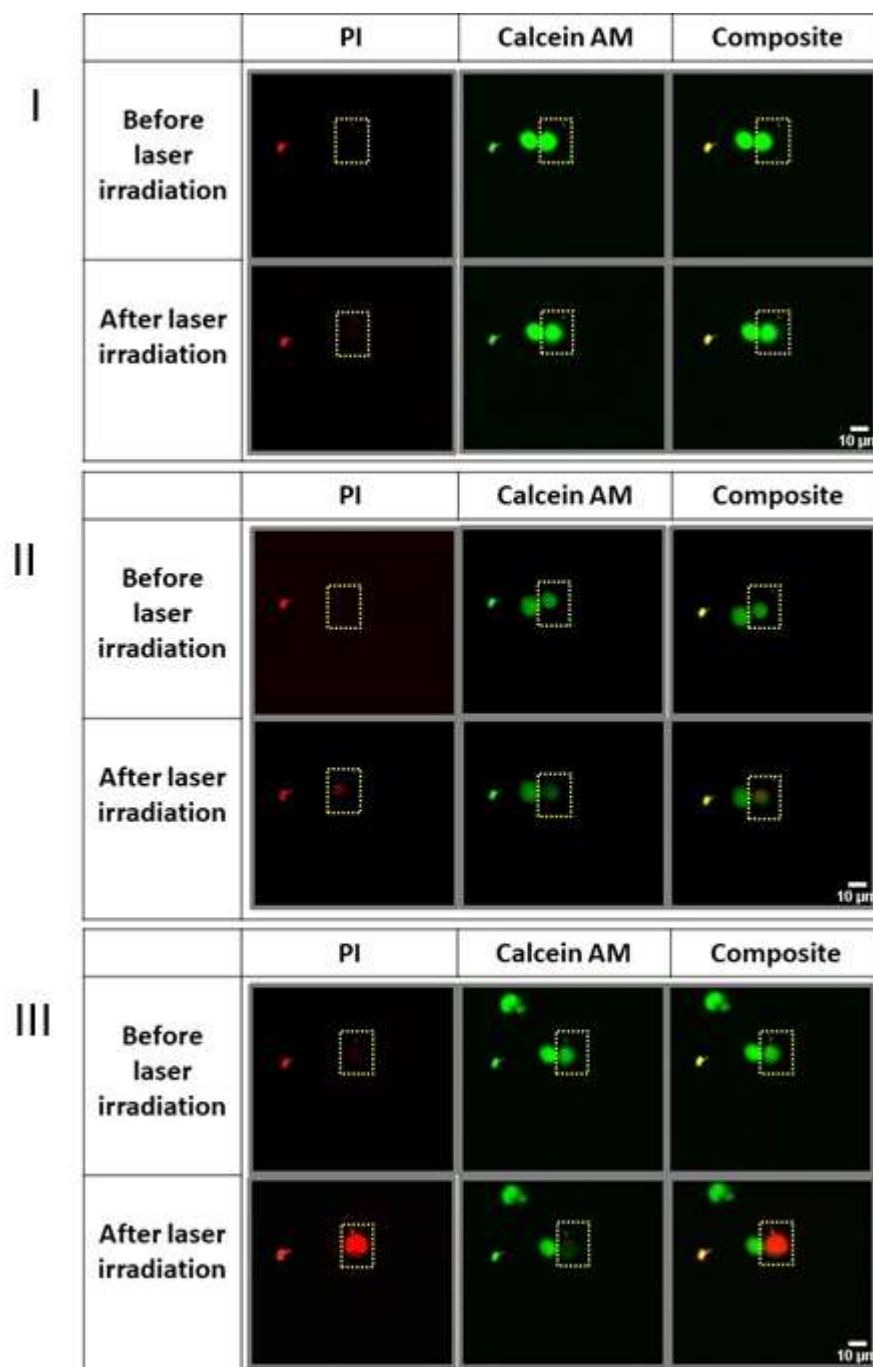
Figure 5.7 Fluorescent images of the targeted individual cells, before and 2 h after the laser treatment. Laser fluences are 56, 63 and 71 mJ/cm^2 respectively (I, II and III, 10 ms). The yellow dotted square represents the treated cell. The small spot on the left side of the image is the defect from the camera.

In conclusion, the Jurkat cells were studies in several steps (traditional adhered cell treatment, floating cell treatment), the specific laser fluence range (56 to 63 mJ/cm^2) provided the possibility to optoporate the floating Jurkat cells.

CHAPTER 6   GENERAL DISCUSSION

6.1 Real-time monitoring of plasmonic nanoparticle-mediated pulsed laser single-cell optoporation

In this thesis, we have developed a reliable protocol for a plasmonic NP-mediated pulsed laser single-cell optoporation. We optimized optoporation process of adherent human breast cancer cell MDA-MB-231 using a compact and easy-to-access nanosecond laser based on a single cell real-time response to the irradiation of an individual NP bound on the cell membrane. The optical setup was performed to identify bound NPs (the membrane targets and near field enhancers) and single-cell optoporation. Real-time tracking of PI fluorophores (dynamic flux curve) and its fluorescence distributions in the targeted cell after the laser irradiation pave new ways to study cellular responses during the cell optoporation, which requires an optimized cytoplasmic trafficking pathway for an efficient transfection.

The bound NPs on the surface of membrane played important roles in the optoporation as the biomarkers and thermal generating spot for pores' formation. The visualized NPs on the cell membrane was achieved with help of the homemade multifunctional optical setup, by the backscattering imaging. A real-time monitoring of the internalization of the impermeable PI molecules was obtained using a modified external-built fluorescence imaging setup. The single cellular real-time response to the nanosecond laser irradiation indicates a detailed relation of the delivered exogenous molecules and the cellular responses after the laser treatment. By using different laser fluences, cellular responses depend on the membrane damages and its subsequent self-healing procedure. A minor rupture of the cell membrane can be resealed by itself, giving out a weak and degressive fluorescent signal. As the laser fluence increases, a bigger rupture below of the killing threshold can be still generated, and the injured cell uptakes more PI molecules, resulting a strong and stable fluorescence signal and simultaneously recovers the formed pores. With the higher laser fluence (above the threshold), the laser generates a severe damage, the cell is dead and plenty of PI molecules enter into the cell Two different possible location dependent mechanisms are shown in Figure 6.1, and the accurate location of NPs on the surface of the cell membrane where the laser beam focus directly affects on the optoporation and cell viability. The laser fluences on the plasmonic nanoparticles should be adjusted to reduce absorbed energy, which melts or

breaks into fragments. It was observed that the laser irradiation targeting the NPs near the cell nucleus kills the cell compared to the irradiated NPs far away from the nucleus due to possible pore formation in cell nucleus. Understanding single cell optoporation is important to provide an efficient transfection for a broad range of biomedical applications.
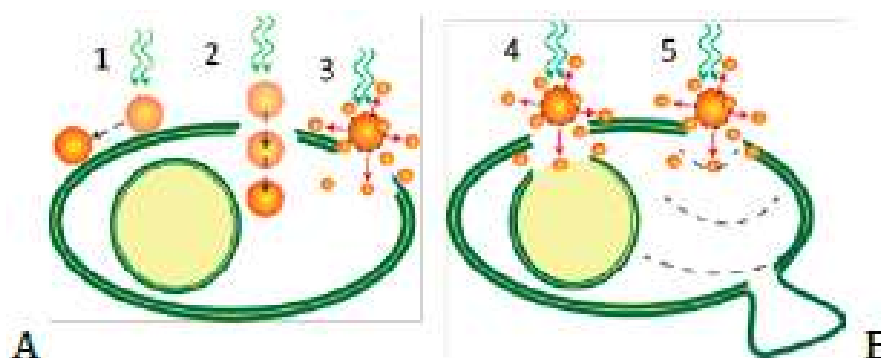
Figure 6.1 NPs decorated cell membrane optomechanical phenomena after local perforation. A.1) NP is driven away; A.2) NP is sinking into the cell membrane; A.3) NP is destroyed and the local membrane is ruptured; B.4) NP near the cell nucleus is destroyed and both the cell and the nucleic membrane are ruptured; B.5) NP afar from the cell nucleus is destroyed and the cell bleb is induced by the pressure wave.

6.2 Visualization of plasmonic nanoparticles bound cell membrane

A darkfield imaging protocol (Figure 6.2.A) has been widely used to visualize the plasmonic NPs. The darkfield imaging protocol visualizes cells and tissues and detects an elastically scattered light by the plasmonic NPs in biological environments. A multiplexing capability can be obtained by the combination with a hyperspectral setup. However, the darkfield imaging protocol offers rather low contrast for NPs in diffusing cells or tissue samples. Another wide-field hyperspectral 3D imaging of NPs bound cell using a reflected light microscopy proposed by Patskovsky et al. [102] overcomes limitations of the darkfield imaging and the poor contrast of brightfield imaging. As shown in Figure 6.2.B, the reflected light microscopy requires high NA oil immersion objectives to obtain a better contrast by minimizing cellular background and backscattering light [93]The complexity of the optical setup for the visualization of plasmonic NPs is a drawback in the nanosecond laser irradiation optoporation.
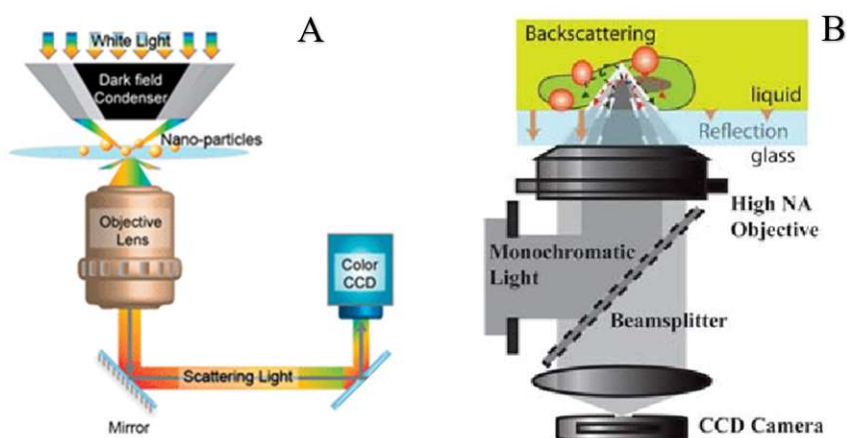
Figure 6.2 A) Traditional darkfield imaging of the NPs in a cell sample, NA matching between the objective and the darkfield condenser is necessary; B) The wide-field hyperspectral backscattering imaging of the NPs in a cell sample, high NA objective is needed for the NPs visualization. Adapted from Ref. [93, 133].

A cost-effective side-illumination device with LED arrays reduces the mentioned complexity of the visualization of plasmonic. The side-illumination imaging protocol has visualized the plasmonic NPs without involving defect of the surface of the sample container (i.e., glass slide and cover slip). Moreover, there is no requirement for an objective magnification. In this thesis, a high contrast for differentiating plasmonic NPs from cells has been achieved by using both 60X and 20X objectives (Figure 6.3). The side-illumination device is a promising tool for the laser-mediated cell optoporation due to simplifying complicated optical setups and offering exclusive biomedical (Appendix A).
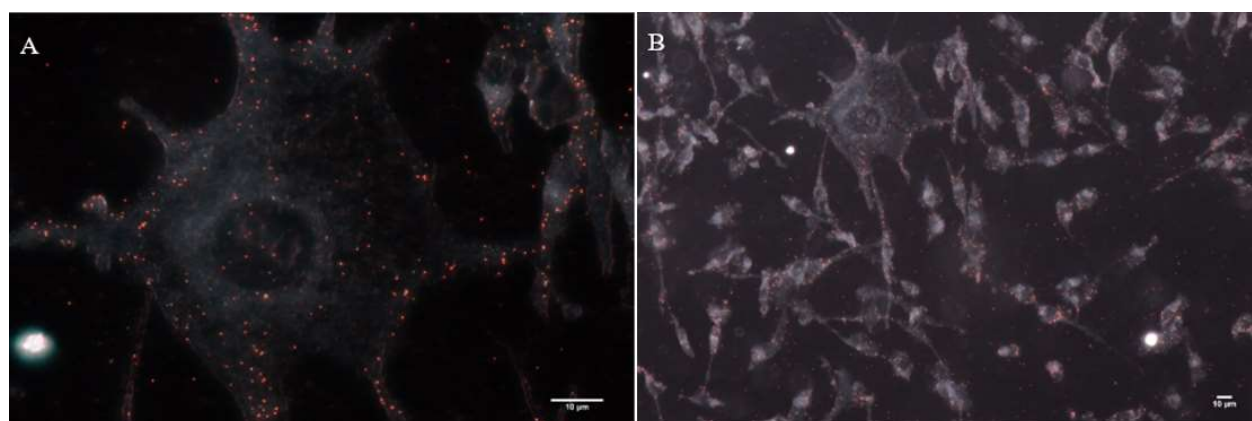
Figure 6.3 Side-illumination imaging of the NPs in a cellular environment with A) 60x and B) 20x objective respectively. Both 60x and 20x objectives provide enough NPs-cell complex contrast.

60x objective with more NPs details and 20x objective with a larger field of view. Scale bar is 10 μm.

6.3 Plasmonic nanoparticle-assisted femtosecond laser Jurkat cells optoporation

After preparing plasmonic NP bound Jurkat cell with a minimum free NPs (in suspension), Jurkat cells were found with a range number of 4~7 NPs on the cell membrane. The polymer adhered Jurkat cells were studied for the preliminary laser fluence range from 1.3 to 252 mJ/cm^2 and it was found a fluence range between 32 to 252 mJ/cm^2 is needed for more exploration for optoporation. Then the laser fluence range exploration (32 to 252 mJ/cm^2) was on the Jurkat cells in the floating condition. The optoporation was performed with different fluences (42mJ/cm^2 to 270 mJ/cm^2 for the Jurkat cell without NPs bound; 42 mJ/cm^2 to 78 mJ/cm^{2}for the Jurkat cells with NPs bound). The treated cells without NPs bound were perforated when the laser fluence was 79 mJ/cm^{2}and the cells were dead with the laser fluence at 179 mJ/cm^2 and higher. The cells with NPs bound were perforated at laser fluence 63 mJ/cm^2 and the cells were killed with the laser fluence of 71 mJ/cm^2. Different biomedical applications could be obtained employing the results such as the selective cell sorting, which is to eliminate the NPs bound suspension Jurkat cells from the co-culture of NPs bound Jurkat cells and the bare Jurkat cells; another application could be the optoporation of Jurkat cells mediated by the femtosecond laser with the NPs bound on the cell membrane. Various laser fluences and effects on the treated cells (adhered Jurkat cells, no NPs bound Jurkat cells and NPs bound Jurkat cells) are summarized in a flow chart for a better understanding (Figure 6.4). The NPs bound Jurkat cells can be eliminated within the fluence range from 63 mJ/cm^2 to 79 mJ/cm^2 in the co-culture of the NPs bound Jurkat cells and the bare Jurkat cells. For the NP-Jurkat cells optoporation, the laser fluence will be chosen between 56 mJ/cm^2 to 71 mJ/cm^2.
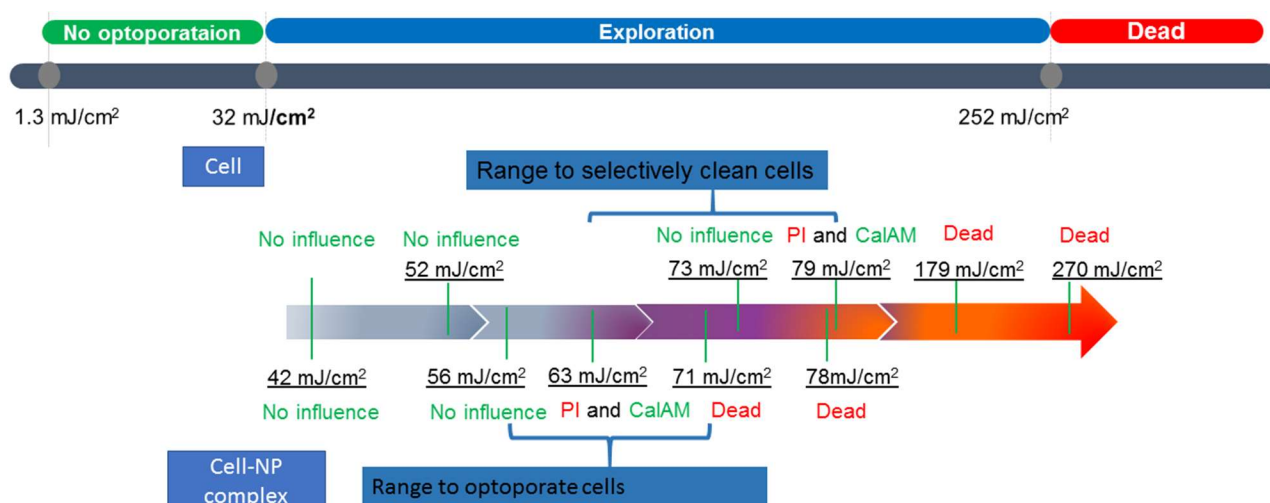
Figure 6.4 Flow chart of laser treatments on the suspension Jurkat cell with different laser parameters. The NPs decorated suspension Jurkat cells have an ideal laser fluence range from 56 mJ/cm² to 71 mJ/cm² for the optoporation. For the specific NPs decorated Jurkat cells sorting from the co-culture, the ideal laser fluence range is from 63 mJ/cm² to 79 mJ/cm².

The narrow range of the laser fluences raises a minor drawback for the optoporation of a bunch of suspension cells in a short time with high efficiency and cell viability. To achieve high optoporation efficiency and throughput simultaneously, a microfluidic system with a constant suspension cell optoporation is recommended to enhance the optoporation by modifying the shape of the laser beam to elongate the focal zone for a uniform laser energy deposition on the cell membrane. (Appendix B). In general, plasmonic NPs-assisted Jurkat cell optoporation by the femtosecond laser might be useful for the activation of immune cells for immunotherapy.

CHAPTER 7 CONCLUSION AND RECOMMENDATIONS

7.1 Main contributions of the thesis

The thesis covers interesting aspects of cell therapy using a nanotechnology-assisted pulsed laser optoporation. Here, we mainly scrutinize all significant parameters, including laser wavelength, laser pulse width and laser fluences, on the nanotechnology-assisted optoporation of adherent and suspended cell lines.

The assembled multifunctional optical setup fulfilled our goal for a real-time monitoring of cellular responses during the nanosecond laser irradiation and cell viability post-treatment. The attached plasmonic NPs (as the marker) on the cell membrane, assisted the visualization, were targeted by a laser beam for the optoporation. Different cellular responses depending on the nanosecond laser parameters were demonstrated a location and fluence dependent optoporation.

The low contrast and complexity of commercial optical setups for the visualization of plasmonic NPs in a cellular environment limit biomedical applications including optoporation. The samples incubated with plasmonic NPs exposed to the LED light from the side-illumination device simply observed without drawbacks of using high NA of objectives. Without limitations of microscope objectives, the side-illumination device was easily adaptable to any basic microscopes to provide a multiplexed image. Three different plasmonic NPs in the cell culture medium and cellular environment were distinguished due to their different scattering lights.

Perforation of suspension Jurkat cells with fs laser has here performed by binding plasmonic NPs to the cellular membrane and internalizing the exogenous small molecules. PI fluorophores as the exogenous materials were internalized into the cell at an optimized range of laser fluence (63 to 71 mJ/cm^2) without reducing cell viability. The treated individual suspension Jurkat cells by using a focused laser beam under their natural floating environment showed a selective transfection; however, the optoporation of suspension cells requires further investigations for gene transfection and therapy

7.2 Recommendations and future work.

The pulsed laser manipulation of plasmonic NPs bound cells (adherent and suspended) and further proof of the exogenous materials intracellular delivery should be studied using the nanosecond

laser optoporation. Pore formation and size created on the cell membrane need to be calculated by introducing exogenous molecules with different molecular weights. After understanding the single cellular perforation with optimized nanosecond laser parameters, scaled-up experiments by treating hundreds of cells may improve the optoporation efficiency without affecting the cell viability rate in order to step forward to clinical translation.

The current developed module of the side-illumination device is suitable for the detection of plasmonic NPs; however, the LED arrays do not provide an efficient illumination and for a long-time usage, it should produce less heat. Moreover, LED wavelengths should be adjustable for the specific fluorophores. The side-illumination device requires a flexible design to be adapted for other well plates, round shape coverslips as well as microfluidic systems.

Optoporation of the suspension of Jurkat cells is important for cell therapy, and it requires a continuous system to perforate all cells to achieve constant transfection efficiency. Therefore, optoporation of Jurkat cells into a microfluidic channel equipped with an optical setup and laser beam is suitable to perform cell therapy in a large scale.

BIBLIOGRAPHY

[1]   N. J. Yang and M. J. Hinner, "Getting across the cell membrane: an overview for small molecules, peptides, and proteins," *Methods Mol Biol,* vol. 1266, pp. 29-53, 2015.

[2]   D. J. Stephens and R. Pepperkok, "The many ways to cross the plasma membrane," *Proceedings of the National Academy of Sciences of the United States of America,* vol. 98, pp. 4295-4298, 2001.

[3]   C. H. Evans, S. C. Ghivizzani, and P. D. Robbins, "Arthritis gene therapy's first death," *Arthritis Res Ther,* vol. 10, p. 110, 2008.

[4]   S. Lehrman, "Virus treatment questioned after gene therapy death," *Nature,* vol. 401, pp. 517-8, Oct 7 1999.

[5]   A. Pfeifer and I. M. Verma, "Gene therapy: promises and problems," *Annu Rev Genomics Hum Genet,* vol. 2, pp. 177-211, 2001.

[6]   G. L. Lukacs, P. Haggie, O. Seksek, D. Lechardeur, N. Freedman, and A. S. Verkman, "Size-dependent DNA mobility in cytoplasm and nucleus," *J Biol Chem,* vol. 275, pp. 1625-9, Jan 21 2000.

[7]   C. J. Bishop, K. L. Kozielski, and J. J. Green, "Exploring the role of polymer structure on intracellular nucleic acid delivery via polymeric nanoparticles," *Journal of controlled release : official journal of the Controlled Release Society,* vol. 219, pp. 488-499, 2015.

[8]   M. R. Capecchi, "High efficiency transformation by direct microinjection of DNA into cultured mammalian cells," *Cell,* vol. 22, pp. 479-88, Nov 1980.

[9]   J. W. Gordon and F. H. Ruddle, "Gene transfer into mouse embryos: production of transgenic mice by pronuclear injection," *Methods Enzymol,* vol. 101, pp. 411-33, 1983.

[10]   C. P. Yao, Z. X. Zhang, R. Rahmanzadeh, and G. Huettmann, "Laser-based gene transfection and gene therapy," *IEEE Trans Nanobioscience,* vol. 7, pp. 111-9, Jun 2008.

[11]   A. A. Davis, M. J. Farrar, N. Nishimura, M. M. Jin, and C. B. Schaffer, "Optoporation and genetic manipulation of cells using femtosecond laser pulses," *Biophys J,* vol. 105, pp. 862-71, Aug 20 2013.

[12]   C. V. Kelly, M. M. Kober, P. Kinnunen, D. A. Reis, B. G. Orr, and M. M. Banaszak Holl, "Pulsed-laser creation and characterization of giant plasma membrane vesicles from cells," *J Biol Phys,* vol. 35, pp. 279-95, Aug 2009.

[13]   T. Shimada, W. Watanabe, S. Matsunaga, T. Higashi, H. Ishii, K. Fukui*, et al.*, "Intracellular disruption of mitochondria in a living HeLa cell with a 76-MHz femtosecond laser oscillator," *Opt Express,* vol. 13, pp. 9869-80, Nov 28 2005.

[14]   H. Potter and R. Heller, "Transfection by electroporation," *Curr Protoc Mol Biol,* vol. Chapter 9, p. Unit9 3, Oct 2010.

[15]   J. L. Young and D. A. Dean, "Electroporation-mediated gene delivery," *Adv Genet,* vol. 89, pp. 49-88, 2015.

[16] D. A. Dean, "Cell-specific targeting strategies for electroporation-mediated gene delivery in cells and animals," *J Membr Biol,* vol. 246, pp. 737-44, Oct 2013.

[17] S. Mehier-Humbert and R. H. Guy, "Physical methods for gene transfer: improving the kinetics of gene delivery into cells," *Adv Drug Deliv Rev,* vol. 57, pp. 733-53, Apr 5 2005.

[18] J. Yoon, S. W. Ryu, S. Lee, and C. Choi, "Cytosolic irradiation of femtosecond laser induces mitochondria-dependent apoptosis-like cell death via intrinsic reactive oxygen cascades," *Sci Rep,* vol. 5, p. 8231, Feb 4 2015.

[19] W. Ding, E. Bergeron, R. Lachaine, and M. Meunier, "16 - Nanomaterial-assisted light-induced poration and transfection of mammalian cells," in *Applications of Nanoscience in Photomedicine*, M. R. Hamblin and P. Avci, Eds., ed Oxford: Chandos Publishing, 2015, pp. 331-376.

[20] R. Lachaine, C. Boutopoulos, P. Y. Lajoie, E. Boulais, and M. Meunier, "Rational Design of Plasmonic Nanoparticles for Enhanced Cavitation and Cell Perforation," *Nano Lett,* vol. 16, pp. 3187-94, May 11 2016.

[21] X. Sun, G. Zhang, R. S. Keynton, M. G. O'Toole, D. Patel, and A. M. Gobin, "Enhanced drug delivery via hyperthermal membrane disruption using targeted gold nanoparticles with PEGylated Protein-G as a cofactor," *Nanomedicine,* vol. 9, pp. 1214-22, Nov 2013.

[22] S. Kalies, D. Heinemann, M. Schomaker, T. Birr, T. Ripken, H. E. D. L. L. Meyer*, et al.*, "Gold nanoparticle mediated laser transfection for high-throughput antisense applications," in *Medical Laser Applications and Laser-Tissue Interactions VI*, Munich, 2013, p. 880309.

[23] E. C. Wang and A. Z. Wang, "Nanoparticles and their applications in cell and molecular biology," *Integrative biology : quantitative biosciences from nano to macro,* vol. 6, pp. 9-26, 2014.

[24] D. Heinemann, M. Schomaker, S. Kalies, M. Schieck, R. Carlson, H. Murua Escobar*, et al.*, "Gold nanoparticle mediated laser transfection for efficient siRNA mediated gene knock down," *PLoS One,* vol. 8, p. e58604, 2013.

[25] J. M. Meacham, K. Durvasula, F. L. Degertekin, and A. G. Fedorov, "Physical Methods for Intracellular Delivery:Practical Aspects from Laboratory Use to Industrial-Scale Processing," *Journal of Laboratory Automation,* vol. 19, pp. 1-18, 2014.

[26] K. Kamimura, T. Suda, G. Zhang, and D. Liu, "Advances in Gene Delivery Systems," *Pharmaceut Med,* vol. 25, pp. 293-306, Oct 1 2011.

[27] K. Lundstrom, "Viral Vectors in Gene Therapy," *Diseases (Basel, Switzerland),* vol. 6, p. 42, 2018.

[28] P. C. Hendrie and D. W. Russell, "Gene Targeting with Viral Vectors," *Molecular Therapy,* vol. 12, pp. 9-17, 2005/07/01/ 2005.

[29] J. L. Betker and T. J. Anchordoquy, "Relating toxicity to transfection: using sphingosine to maintain prolonged expression in vitro," *Molecular pharmaceutics,* vol. 12, pp. 264-273, 2015.

[30] M. Breunig, U. Lungwitz, R. Liebl, and A. Goepferich, "Breaking up the correlation between efficacy and toxicity for nonviral gene delivery," *Proceedings of the National Academy of Sciences of the United States of America,* vol. 104, pp. 14454-14459, 2007.

[31] F. Liu and L. Huang, "Noninvasive gene delivery to the liver by mechanical massage," *Hepatology,* vol. 35, pp. 1314-1319, 2002.

[32] H. Mukai, S. Kawakami, and M. Hashida, "Renal press-mediated transfection method for plasmid DNA and siRNA to the kidney," *Biochemical and Biophysical Research Communications,* vol. 372, pp. 383-387, 2008/08/01/ 2008.

[33] H. Mukai, S. Kawakami, Y. Kamiya, F. Ma, H. Takahashi, K. Satake*, et al.*, "Pressure-mediated transfection of murine spleen and liver," *Human gene therapy,* vol. 20, pp. 1157-1167, 2009.

[34] S. Oba, S. Kumano, E. Suzuki, H. Nishimatsu, M. Takahashi, H. Takamori*, et al.*, "miR-200b precursor can ameliorate renal tubulointerstitial fibrosis," *PloS one,* vol. 5, p. e13614, 2010.

[35] E. B. Ghartey-Tagoe, B. A. Babbin, A. Nusrat, A. S. Neish, and M. R. Prausnitz, "Plasmid DNA and siRNA transfection of intestinal epithelial monolayers by electroporation," *International Journal of Pharmaceutics,* vol. 315, pp. 122-133, 2006/06/06/ 2006.

[36] J. A. Williams, "Vector Design for Improved DNA Vaccine Efficacy, Safety and Production," *Vaccines,* vol. 1, pp. 225-249, 2013.

[37] S. Lu, S. Wang, and J. M. Grimes-Serrano, "Current progress of DNA vaccine studies in humans," *Expert Rev Vaccines,* vol. 7, pp. 175-91, Mar 2008.

[38] M. A. Liu, "DNA vaccines: an historical perspective and view to the future," *Immunol Rev,* vol. 239, pp. 62-84, Jan 2011.

[39] Y. Wang, Y. Guo, X. Wang, J. Huang, J. Shang, and S. Sun, "Human serum amyloid P functions as a negative regulator of the innate and adaptive immune responses to DNA vaccines," *J Immunol,* vol. 186, pp. 2860-70, Mar 1 2011.

[40] C. Rosazza, J. M. Escoffre, A. Zumbusch, and M. P. Rols, "The actin cytoskeleton has an active role in the electrotransfer of plasmid DNA in mammalian cells," *Mol Ther,* vol. 19, pp. 913-21, May 2011.

[41] X. Du, J. Wang, Q. Zhou, L. Zhang, S. Wang, Z. Zhang*, et al.*, "Advanced physical techniques for gene delivery based on membrane perforation," *Drug delivery,* vol. 25, pp. 1516-1525, 2018.

[42] T. Pylaev, E. Vanzha, E. Avdeeva, B. Khlebtsov, and N. Khlebtsov, "A novel cell transfection platform based on laser optoporation mediated by Au nanostar layers," *Journal of Biophotonics $V 12,* pp. n/a-n/a, 2019.

[43] J. C. Weaver, K. C. Smith, A. T. Esser, R. S. Son, and T. R. Gowrishankar, "A brief overview of electroporation pulse strength-duration space: a region where additional intracellular effects are expected," *Bioelectrochemistry (Amsterdam, Netherlands),* vol. 87, pp. 236-243, 2012.

[44] E. C. Gianulis, J. Lee, C. Jiang, S. Xiao, B. L. Ibey, and A. G. Pakhomov, "Electroporation of mammalian cells by nanosecond electric field oscillations and its inhibition by the electric field reversal," *Scientific Reports,* vol. 5, p. 13818, 09/08/online 2015.

[45]   W. Zhou, Z. Xiong, Y. Liu, C. Yao, and C. Li, "Low voltage irreversible electroporation induced apoptosis in HeLa cells," *Journal of Cancer Research and Therapeutics,* vol. 8, pp. 80-85, January 1, 2012 2012.

[46]   K. Dhakal, B. Black, and S. Mohanty, "Introduction of impermeable actin-staining molecules to mammalian cells by optoporation," *Scientific reports,* vol. 4, pp. 6553-6553, 2014.

[47]   M. Shibata, H. Nishimasu, N. Kodera, S. Hirano, T. Ando, T. Uchihashi*, et al.*, "Real-space and real-time dynamics of CRISPR-Cas9 visualized by high-speed atomic force microscopy," *Nature Communications,* vol. 8, p. 1430, 2017/11/10 2017.

[48]   P. D. Hsu, E. S. Lander, and F. Zhang, "Development and applications of CRISPR-Cas9 for genome engineering," *Cell,* vol. 157, pp. 1262-78, Jun 5 2014.

[49]   A. V. Wright, J. K. Nunez, and J. A. Doudna, "Biology and Applications of CRISPR Systems: Harnessing Nature's Toolbox for Genome Engineering," *Cell,* vol. 164, pp. 29-44, Jan 14 2016.

[50]   L. Cong, F. A. Ran, D. Cox, S. Lin, R. Barretto, N. Habib*, et al.*, "Multiplex genome engineering using CRISPR/Cas systems," *Science,* vol. 339, pp. 819-23, Feb 15 2013.

[51]   J. A. Doudna and E. Charpentier, "Genome editing. The new frontier of genome engineering with CRISPR-Cas9," *Science,* vol. 346, p. 1258096, Nov 28 2014.

[52]   J. Yang, X. Meng, J. Pan, N. Jiang, C. Zhou, Z. Wu*, et al.*, "CRISPR/Cas9-mediated noncoding RNA editing in human cancers," *RNA biology,* vol. 15, pp. 35-43, 2017.

[53]   Y. Zhang, G. Arango, F. Li, X. Xiao, R. Putatunda, J. Yu*, et al.*, "Comprehensive off-target analysis of dCas9-SAM-mediated HIV reactivation via long noncoding RNA and mRNA profiling," *BMC medical genomics,* vol. 11, pp. 78-78, 2018.

[54]   E. Boulais, R. Lachaine, and M. Meunier, "Plasma mediated off-resonance plasmonic enhanced ultrafast laser-induced nanocavitation," *Nano Lett,* vol. 12, pp. 4763-9, Sep 12 2012.

[55]   C. M. Pitsillides, E. K. Joe, X. Wei, R. R. Anderson, and C. P. Lin, "Selective cell targeting with light-absorbing microparticles and nanoparticles," *Biophysical journal,* vol. 84, pp. 4023-4032, 2003.

[56]   C. Yao, R. Rahmanzadeh, E. Endl, Z. Zhang, J. Gerdes, and G. Huttmann, "Elevation of plasma membrane permeability by laser irradiation of selectively bound nanoparticles," *J Biomed Opt,* vol. 10, p. 064012, Nov-Dec 2005.

[57]   E. Y. Lukianova-Hleb, A. P. Samaniego, J. Wen, L. S. Metelitsa, C. C. Chang, and D. O. Lapotko, "Selective gene transfection of individual cells in vitro with plasmonic nanobubbles," *J Control Release,* vol. 152, pp. 286-93, Jun 10 2011.

[58]   A. Ben-Yakar, D.S. Eversole, and O. Ekici, "Spherical and Anisotropic Gold Nanomaterials in Plasmonic Laser Phototherapy of Cancer," in *Nanotechnologies for the Life Sciences*, ed, 2008, pp. 493-593.

[59]   J. Baumgart, L. Humbert, E. Boulais, R. Lachaine, J. J. Lebrun, and M. Meunier, "Off-resonance plasmonic enhanced femtosecond laser optoporation and transfection of cancer cells," *Biomaterials,* vol. 33, pp. 2345-50, Mar 2012.

[60]   B. Lamprecht, J. R. Krenn, A. Leitner, and F. R. Aussenegg, "Resonant and Off-Resonant Light-Driven Plasmons in Metal Nanoparticles Studied by Femtosecond-Resolution Third-Harmonic Generation," *Physical Review Letters,* vol. 83, pp. 4421-4424, 11/22/ 1999.

[61]   B. St-Louis Lalonde, E. Boulais, J. J. Lebrun, and M. Meunier, "Visible and near infrared resonance plasmonic enhanced nanosecond laser optoporation of cancer cells," *Biomed Opt Express,* vol. 4, pp. 490-9, Apr 1 2013.

[62]   S. K. Mohanty, M. Sharma, and P. K. Gupta, "Laser-assisted microinjection into targeted animal cells," *Biotechnol Lett,* vol. 25, pp. 895-9, Jun 2003.

[63]   J. Krawinkel, M. L. Torres-Mapa, K. Werelius, A. Heisterkamp, S. Ruttermann, G. E. Romanos*, et al.*, "Gold Nanoparticle-Mediated Delivery of Molecules into Primary Human Gingival Fibroblasts Using ns-Laser Pulses: A Pilot Study," *Materials (Basel),* vol. 9, May 20 2016.

[64]   G. Palumbo, M. Caruso, E. Crescenzi, M. F. Tecce, G. Roberti, and A. Colasanti, "Targeted gene transfer in eucaryotic cells by dye-assisted laser optoporation," *J Photochem Photobiol B,* vol. 36, pp. 41-6, Oct 1996.

[65]   H. Schneckenburger, A. Hendinger, R. Sailer, W. S. Strauss, and M. Schmitt, "Laser-assisted optoporation of single cells," *J Biomed Opt,* vol. 7, pp. 410-6, Jul 2002.

[66]   R. Xiong, K. Raemdonck, K. Peynshaert, I. Lentacker, I. De Cock, J. Demeester*, et al.*, "Comparison of gold nanoparticle mediated photoporation: vapor nanobubbles outperform direct heating for delivering macromolecules in live cells," *ACS Nano,* vol. 8, pp. 6288-96, Jun 24 2014.

[67]   N. Saklayen, M. Huber, M. Madrid, V. Nuzzo, D. I. Vulis, W. Shen*, et al.*, "Intracellular Delivery Using Nanosecond-Laser Excitation of Large-Area Plasmonic Substrates," *ACS Nano,* vol. 11, pp. 3671-3680, 2017/04/25 2017.

[68]   R. Xiong, C. Drullion, P. Verstraelen, J. Demeester, A. G. Skirtach, C. Abbadie*, et al.*, "Fast spatial-selective delivery into live cells," *Journal of Controlled Release,* vol. 266, pp. 198-204, 2017/11/28/ 2017.

[69]   E. Bergeron, C. Boutopoulos, R. Martel, A. Torres, C. Rodriguez, J. Niskanen*, et al.*, "Cell-specific optoporation with near-infrared ultrafast laser and functionalized gold nanoparticles," *Nanoscale,* vol. 7, pp. 17836-47, Nov 14 2015.

[70]   U. K. Tirlapur and K. Konig, "Targeted transfection by femtosecond laser," *Nature,* vol. 418, pp. 290-1, Jul 18 2002.

[71]   A. Uchugonova, K. Konig, R. Bueckle, A. Isemann, and G. Tempea, "Targeted transfection of stem cells with sub-20 femtosecond laser pulses," *Opt Express,* vol. 16, pp. 9357-64, Jun 23 2008.

[72]   D. J. Stevenson, F. J. Gunn-Moore, P. Campbell, and K. Dholakia, "Single cell optical transfection," *J R Soc Interface,* vol. 7, pp. 863-71, Jun 6 2010.

[73]   N. N. Nedyalkov, S. Imamova, P. A. Atanasov, Y. Tanaka, and M. Obara, "Interaction between ultrashort laser pulses and gold nanoparticles: nanoheater and nanolens effect," *Journal of Nanoparticle Research,* vol. 13, pp. 2181-2193, 2011/05/01 2011.

[74] M. Schomaker, J. Baumgart, D. Motekaitis, D. Heinemann, J. Krawinkel, M. Pangalos*, et al.*, *Mechanisms of gold nanoparticle mediated ultrashort laser cell membrane perforation* vol. 7925: SPIE, 2011.

[75] E. Boulais, R. Lachaine, A. Hatef, and M. Meunier, "Plasmonics for pulsed-laser cell nanosurgery: Fundamentals and applications," *Journal of Photochemistry and Photobiology C: Photochemistry Reviews,* vol. 17, pp. 26-49, 2013/12/01/ 2013.

[76] D. Stevenson, B. Agate, X. Tsampoula, P. Fischer, C. T. Brown, W. Sibbett*, et al.*, "Femtosecond optical transfection of cells: viability and efficiency," *Opt Express,* vol. 14, pp. 7125-33, Aug 7 2006.

[77] M. Antkowiak, M. L. Torres-Mapa, F. Gunn-Moore, and K. Dholakia, "Application of dynamic diffractive optics for enhanced femtosecond laser based cell transfection," *J Biophotonics,* vol. 3, pp. 696-705, Oct 2010.

[78] H. Georg Breunig, A. Uchugonova, A. Batista, and K. Konig, "Software-aided automatic laser optoporation and transfection of cells," *Sci Rep,* vol. 5, p. 11185, Jun 8 2015.

[79] M. Schomaker, D. Heinemann, S. Kalies, S. Willenbrock, S. Wagner, I. Nolte*, et al.*, "Characterization of nanoparticle mediated laser transfection by femtosecond laser pulses for applications in molecular medicine," *J Nanobiotechnology,* vol. 13, p. 10, Feb 3 2015.

[80] T. Montier, P. Delépine, K. Le Ny, Y. Fichou, M. Le Bris, E. Hardy*, et al.*, "KLN-5: a safe monocationic lipophosphoramide to transfect efficiently haematopoietic cell lines and human CD34+ cells," *Biochimica et Biophysica Acta (BBA) - Biomembranes,* vol. 1665, pp. 118-133, 2004/10/11/ 2004.

[81] B. B. Praveen, D. J. Stevenson, M. Antkowiak, K. Dholakia, and F. J. Gunn-Moore, "Enhancement and optimization of plasmid expression in femtosecond optical transfection," *Journal of Biophotonics,* vol. 4, pp. 229-235, 2011.

[82] K. Landauer, M. Dürrschmid, H. Klug, S. Wiederkum, G. Blüml, and O. Doblhoff-Dier, "Detachment factors for enhanced carrier to carrier transfer of CHO cell lines on macroporous microcarriers," *Cytotechnology,* vol. 39, pp. 37-45, 2002.

[83] S. Basiouni, H. Fuhrmann, and J. Schumann, "High-efficiency transfection of suspension cell lines," *BioTechniques,* vol. 53, pp. 1-4, 2012.

[84] H. G. Breunig, A. Uchugonova, A. Batista, and K. König, "High-throughput continuous flow femtosecond laser-assisted cell optoporation and transfection," *Microscopy Research and Technique,* vol. 77, pp. 974-979, 2014.

[85] A. Uchugonova, H. G. Breunig, A. Batista, and K. Konig, "Optical reprogramming of human cells in an ultrashort femtosecond laser microfluidic transfection platform," *J Biophotonics,* vol. 9, pp. 942-7, Sep 2016.

[86] R. F. Marchington, Y. Arita, X. Tsampoula, F. J. Gunn-Moore, and K. Dholakia, "Optical injection of mammalian cells using a microfluidic platform," *Biomedical optics express,* vol. 1, pp. 527-536, 2010.

[87] M. Waleed, S. U. Hwang, J. D. Kim, I. Shabbir, S. M. Shin, and Y. G. Lee, "Single-cell optoporation and transfection using femtosecond laser and optical tweezers," *Biomed Opt Express,* vol. 4, pp. 1533-47, 2013.

[88] M. Tsukakoshi, S. Kurata, Y. Nomiya, Y. Ikawa, and T. Kasuya, "A novel method of DNA transfection by laser microbeam cell surgery," *Applied Physics B,* vol. 35, pp. 135-140, November 01 1984.

[89] J. S. Soughayer, T. Krasieva, S. C. Jacobson, J. M. Ramsey, B. J. Tromberg, and N. L. Allbritton, "Characterization of cellular optoporation with distance," *Anal Chem,* vol. 72, pp. 1342-7, Mar 15 2000.

[90] X. Huang, B. Kang, W. Qian, M. A. Mackey, P. C. Chen, A. K. Oyelere*, et al.*, "Comparative study of photothermolysis of cancer cells with nuclear-targeted or cytoplasm-targeted gold nanospheres: continuous wave or pulsed lasers," *J Biomed Opt,* vol. 15, p. 058002, Sep-Oct 2010.

[91] H. Zhao, J. Oczos, P. Janowski, D. Trembecka, J. Dobrucki, Z. Darzynkiewicz*, et al.*, "Rationale for the real-time and dynamic cell death assays using propidium iodide," *Cytometry Part A,* vol. 77A, pp. 399-405, 2010.

[92] H. M. Davey and P. Hexley, "Red but not dead? Membranes of stressed Saccharomyces cerevisiae are permeable to propidium iodide," *Environmental Microbiology,* vol. 13, pp. 163-171, 2011.

[93] S. Patskovsky, E. Bergeron, D. Rioux, and M. Meunier, "Wide-field hyperspectral 3D imaging of functionalized gold nanoparticles targeting cancer cells by reflected light microscopy," *J Biophotonics,* vol. 8, pp. 401-7, May 2015.

[94] S. Patskovsky and M. Meunier, "Reflected light microspectroscopy for single-nanoparticle biosensing," *J Biomed Opt,* vol. 20, p. 097001, 2015.

[95] D. A. Jans and A. S. Sobolev, "Editorial: Targeted Subcellular Delivery of Anti-cancer Agents," *Frontiers in pharmacology,* vol. 9, pp. 1577-1577, 2019.

[96] Y. A. Lau, B. L. Henderson, J. Lu, D. P. Ferris, F. Tamanoi, and J. I. Zink, "Continuous spectroscopic measurements of photo-stimulated release of molecules by nanomachines in a single living cell," *Nanoscale,* vol. 4, pp. 3482-9, Jun 7 2012.

[97] E. Fortunati and V. Bianchi, "Plasma membrane damage detected by nucleic acid leakage," *Mol Toxicol,* vol. 2, pp. 27-38, Winter 1989.

[98] J. L. Compton, A. N. Hellman, and V. Venugopalan, "Hydrodynamic determinants of cell necrosis and molecular delivery produced by pulsed laser microbeam irradiation of adherent cells," *Biophysical journal,* vol. 105, pp. 2221-2231, 2013.

[99] X. Huang and M. A. El-Sayed, "Gold nanoparticles: Optical properties and implementations in cancer diagnosis and photothermal therapy," *Journal of Advanced Research,* vol. 1, pp. 13-28, 2010/01/01/ 2010.

[100] K.-T. Yong, I. Roy, M. T. Swihart, and P. N. Prasad, "Multifunctional Nanoparticles as Biocompatible Targeted Probes for Human Cancer Diagnosis and Therapy," *Journal of materials chemistry,* vol. 19, pp. 4655-4672, 2009.

[101] A. B. Chinen, C. M. Guan, J. R. Ferrer, S. N. Barnaby, T. J. Merkel, and C. A. Mirkin, "Nanoparticle Probes for the Detection of Cancer Biomarkers, Cells, and Tissues by Fluorescence," *Chemical Reviews,* vol. 115, pp. 10530-10574, 2015/10/14 2015.

[102] S. Patskovsky, E. Bergeron, D. Rioux, M. Simard, and M. Meunier, "Hyperspectral reflected light microscopy of plasmonic Au/Ag alloy nanoparticles incubated as multiplex chromatic biomarkers with cancer cells," *Analyst,* vol. 139, pp. 5247-5253, 2014.

[103] A. Saha, S. K. Basiruddin, R. Sarkar, N. Pradhan, and N. R. Jana, "Functionalized Plasmonic−Fluorescent Nanoparticles for Imaging and Detection," *The Journal of Physical Chemistry C,* vol. 113, pp. 18492-18498, 2009/10/29 2009.

[104] K. Seekell, M. J. Crow, S. Marinakos, J. Ostrander, A. Chilkoti, and A. Wax, "Hyperspectral molecular imaging of multiple receptors using immunolabeled plasmonic nanoparticles," *Journal of biomedical optics,* vol. 16, pp. 116003-116003, 2011.

[105] S. Naahidi, M. Jafari, F. Edalat, K. Raymond, A. Khademhosseini, and P. Chen, "Biocompatibility of engineered nanoparticles for drug delivery," *Journal of Controlled Release,* vol. 166, pp. 182-194, 2013/03/10/ 2013.

[106] C.-C. Wang, C.-P. Liang, and C.-H. Lee, "Three-dimensional nanoparticle tracking and simultaneously membrane profiling during endocytosis of living cells," *Applied Physics Letters,* vol. 95, p. 203702, 2009.

[107] X. Huang, P. K. Jain, I. H. El-Sayed, and M. A. El-Sayed, "Gold nanoparticles: interesting optical properties and recent applications in cancer diagnostics and therapy," *Nanomedicine,* vol. 2, pp. 681-693, 2007.

[108] A. K. A. a. J. C. A. V. Kumar, *Robbins & Cotran Pathologic Basis of Disease, 9th Edition*, 2015.

[109] E. Bergeron, S. Patskovsky, D. Rioux, and M. Meunier, "3D multiplexed immunoplasmonics microscopy," *NANOSCALE,* vol. 8, pp. 13263-13272, 2016.

[110] K. Seekell, H. Price, S. Marinakos, and A. Wax, "Optimization of immunolabeled plasmonic nanoparticles for cell surface receptor analysis," *Methods,* vol. 56, pp. 310-316, Feb 2012.

[111] Y. Kawano, C. Higgins, Y. Yamamoto, J. Nyhus, A. Bernard, H.-W. Dong*, et al.*, "Darkfield Adapter for Whole Slide Imaging: Adapting a Darkfield Internal Reflection Illumination System to Extend WSI Applications," *PLOS ONE,* vol. 8, p. e58344, 2013.

[112] S. Ramachandran, D. A. Cohen, A. P. Quist, and R. Lal, "High performance, LED powered, waveguide based total internal reflection microscopy," *Scientific Reports,* vol. 3, p. 2133, 07/04/online 2013.

[113] J. H. Kim and J. S. Park, "Partial dark-field microscopy for investigating domain structures of double-layer microsphere film," *Scientific reports,* vol. 5, pp. 10157-10157, 2015.

[114] M. H. V. Werts, V. Raimbault, M. Loumaigne, L. Griscom, O. Français, J. Navarro*, et al.*, *Optical microscopy and spectroscopy of analyte-sensitive functionalized gold nanoparticles in microfluidic systems* vol. 8595, 2013.

[115] M. Azizi, H. Ghourchian, F. Yazdian, S. Bagherifam, S. Bekhradnia, and B. Nystrom, "Anti-cancerous effect of albumin coated silver nanoparticles on MDA-MB 231 human breast cancer cell line," *Scientific Reports,* vol. 7, Jul 12 2017.

[116]   A. Mukerjee, J. Shankardas, A. P. Ranjan, and J. K. Vishwanatha, "Efficient nanoparticle mediated sustained RNA interference in human primary endothelial cells," *Nanotechnology,* vol. 22, p. 445101, 2011/10/11 2011.

[117]   A. Gallud, D. Warther, M. Maynadier, M. Sefta, F. Poyer, C. D. Thomas*, et al.*, "Identification of MRC2 and CD209 receptors as targets for photodynamic therapy of retinoblastoma using mesoporous silica nanoparticles," *RSC Advances,* vol. 5, pp. 75167-75172, 2015.

[118]   R. A. Meyer, "Light scattering from biological cells: dependence of backscatter radiation on membrane thickness and refractive index," *Applied Optics,* vol. 18, pp. 585-588, 1979/03/01 1979.

[119]   Q. Zhang, L. Zhong, P. Tang, Y. Yu, S. Liu, J. Tian*, et al.*, "Quantitative refractive index distribution of single cell by combining phase-shifting interferometry and AFM imaging," *Scientifique Reports,* vol. 7, 2017.

[120]   L. Pantanowitz, P. N. Valenstein, A. J. Evans, K. J. Kaplan, J. D. Pfeifer, D. C. Wilbur*, et al.*, "Review of the current state of whole slide imaging in pathology," *Journal of pathology informatics,* vol. 2, pp. 36-36, 2011.

[121]   D. L. Bolton, B.-I. Hahn, E. A. Park, L. L. Lehnhoff, F. Hornung, and M. J. Lenardo, "Death of CD4(+) T-cell lines caused by human immunodeficiency virus type 1 does not depend on caspases or apoptosis," *Journal of virology,* vol. 76, pp. 5094-5107, 2002.

[122]   R. E. Jeeninga, B. Jan, B. van der Linden, H. van den Berg, and B. Berkhout, "Construction of a Minimal HIV-1 Variant that Selectively Replicates in Leukemic Derived T-Cell Lines: Towards a New Virotherapy Approach," *Cancer Research,* vol. 65, pp. 3347-3355, 2005.

[123]   D. Mazurov, A. Ilinskaya, G. Heidecker, P. Lloyd, and D. Derse, "Quantitative comparison of HTLV-1 and HIV-1 cell-to-cell infection with new replication dependent vectors," *PLoS pathogens,* vol. 6, pp. e1000788-e1000788, 2010.

[124]   J. E. Celis and N. Carter, *Cell Biology: A Laboratory Handbook*: Elsevier Science, 2005.

[125]   J. E. Celis and K. Geri, *Cell Biology Assays: Essential Methods*: Elsevier Science, 2009.

[126]   S. Li. (2006, 2006). Optimizing electrotransfection of Mammalian cells in vitro. *CSH protocols 2006(1),* 142-147. Available: http://europepmc.org/abstract/MED/22485780

https://doi.org/10.1101/pdb.prot4449

[127]   U. Schneider, H. U. Schwenk, and G. Bornkamm, "Characterization of EBV-genome negative "null" and "T" cell lines derived from children with acute lymphoblastic leukemia and leukemic transformed non-Hodgkin lymphoma," *Int J Cancer,* vol. 19, pp. 621-6, May 15 1977.

[128]   M. R. Katika, P. J. Hendriksen, J. Shao, H. van Loveren, and A. Peijnenburg, "Transcriptome analysis of the human T lymphocyte cell line Jurkat and human peripheral blood mononuclear cells exposed to deoxynivalenol (DON): New mechanistic insights," *Toxicol Appl Pharmacol,* vol. 264, pp. 51-64, Oct 1 2012.

[129]   W. P. Thorpe, M. Toner, R. M. Ezzell, R. G. Tompkins, and M. L. Yarmush, "Dynamics of photoinduced cell plasma membrane injury," *Biophys J,* vol. 68, pp. 2198-206, May 1995.

[130] I. G. Abidor, V. B. Arakelyan, L. V. Chernomordik, Y. A. Chizmadzhev, V. F. Pastushenko, and M. P. Tarasevich, "Electric breakdown of bilayer lipid membranes: I. The main experimental facts and their qualitative discussion," *Journal of Electroanalytical Chemistry and Interfacial Electrochemistry,* vol. 104, pp. 37-52, 1979/01/01/ 1979.

[131] L. V. Chernomordik, G. B. Melikyan, and Y. A. Chizmadzhev, "Biomembrane fusion: a new concept derived from model studies using two interacting planar lipid bilayers," *Biochim Biophys Acta,* vol. 906, pp. 309-52, Oct 5 1987.

[132] S. K. Y. Tang and W. F. Marshall, "Self-repairing cells: How single cells heal membrane ruptures and restore lost structures," *Science,* vol. 356, pp. 1022-1025, 2017.

[133] Y. Li, C. Jing, L. Zhang, and Y.-T. Long, "Resonance scattering particles as biological nanosensors in vitro and in vivo," *Chemical Society Reviews,* vol. 41, pp. 632-642, 2012.

APPENDIX A – SIDE-ILLUMINATION FOR FLUORESCENCE INFORMATION

During the exploration of the side-illumination device, the individual RGB LEDs offer illumination at different wavelengths, Red LED with the peak wavelength ~628 nm, Green LED with the peak wavelength ~530 nm and Blue LED with the peak wavelength ~470 nm. The illumination wavelength of individual LED matches the excitation wavelength of specific cell stain. For example, cell viability stains, PI and Cal-AM, the corresponding excitation wavelengths for them are ~533 nm and ~494 nm respectively (according to the protocol from ThermoFisher). The Green LED and Blue LED illumination wavelengths of the side-illumination device are within the cell stains excitation wavelength range. It is to say that the side-illumination device is capable to provide fluorescence information of the viability for the stained cell samples.

To validate the fluorescence excitation function of the side-illumination device, the same cell sample is tested by the RGB LED illumination, to compare with the standard commercial XCite illumination for fluorescence. Figure A.1 demonstrates the cell sample is stained by PI and Cal-AM, the fluorescence information is offered by two different illumination devices. All RGB LEDs are on to get the fluorescence picture as in Figure A.1.A. With the commercial fluorescence filters and the XCite illumination for PI and Cal-AM, the composite fluorescence picture of the two cell stains is in Figure A.1.B. For the same sample with two cell stains, two fluorescence imaging methods offer the same information that one dead cell is surrounded by other five alive cells. Fluorescence information shown in both methods is similar, it is capable to distinguish the cell viability by comparing and analyzing the fluorescent colors.

As all RGB LEDs illumination might cause either cross-excitation of the cell stains or analysis of the fluorescence signals from the original illumination with errors, they could offer fraud fluorescence information. For that reason, individual functional LEDs (Green LED and Blue LED) are tested for the single cell stain equipped with the stain corresponding emission filter, comparing with the standard commercial fluorescence lamp plus the respective filter cubes. Table A.1 shows the purposes and the tools that are used for the test. The blue LED of the side-illumination device plus the FITC emission filter (~525 nm) are applied to test Cal-AM. The green LED plus the DsRED emission filter (~600 nm) are for the test of PI. For the standard fluorescence lamp, the

XCite LED lamp plus respective filter cubes (FITC filter cube for Cal-AM and DsRED filter cube for PI) are combined for the test.
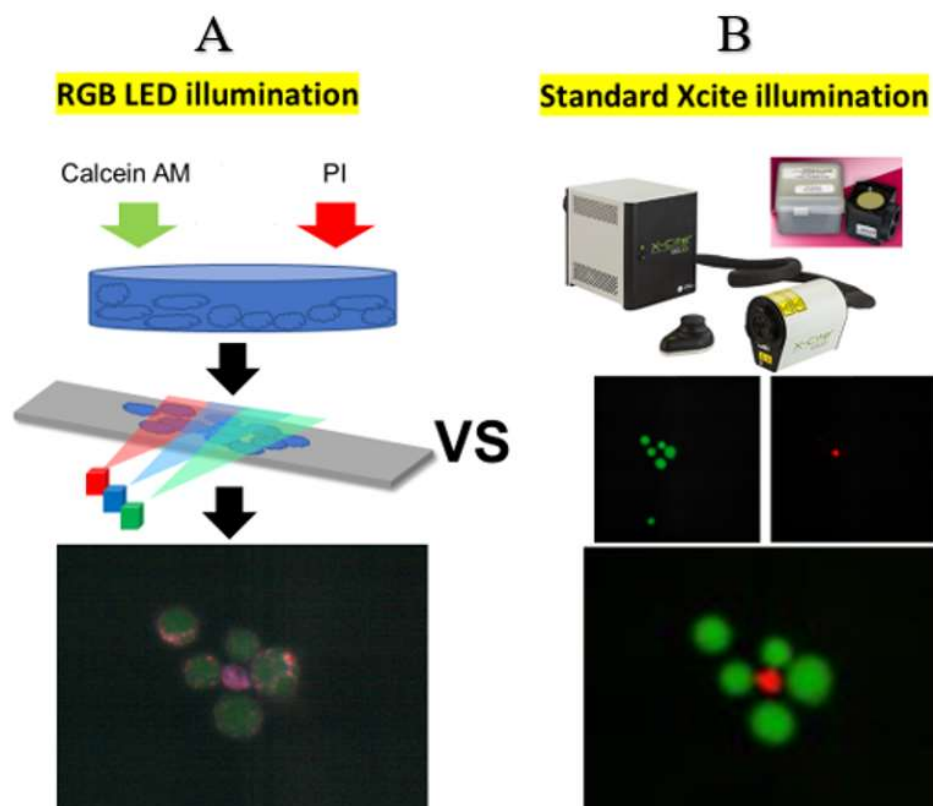

Figure A.1 A) Side-illumination device offers the cell viability stains Cal-AM and PI compared with B) the fluorescence information from the standard XCite illumination. The LED arrays can excite the cell stains to some degree, providing similar fluorescence details of the cell viability.

Table A.1 Cell viability stains fluorescence information is tested by comparing the side-illumination device (Blue LED and Green LED) with the corresponding emission filters to the standard XCite fluorescence setup.

	RGB LEDs plus Emission filter	Standard fluorescence setup
Fluorophore	To test Cal-AM	
	To test PI	
Illumination	Blue LED	XCite LED lamp
	Green LED	
Filter	FITC Emission filter	FITC filter cube
	DsRED Emission filter	DsRED filter cube

The individual test results are shown in Figure A.2. The blue LED plus the FITC emission filter (Figure A.2.A) offers similar fluorescence information as that is provided by the commercial XCite fluorescence setup (Figure A.2.B). The corresponding yellow and purple squares are used to compare the same position in the cell samples. Figure A.2.C is the combined image of the brightfield imaging plus the conventional fluorescence imaging to verify all the cells in the region of interest. The slight difference of the cell fluorescence information provided by two methods might be caused by the movement of the cells or the leak of the cell stains. For the PI test, the green LED plus the DsRED emission filter (Figure A.2.D) offers similar PI fluorescence information as the XCite fluorescence setup (Figure A.2.E). Figure A.2.F is the transmission imaging plus the fluorescence imaging to visualize all the cells in the cell sample.
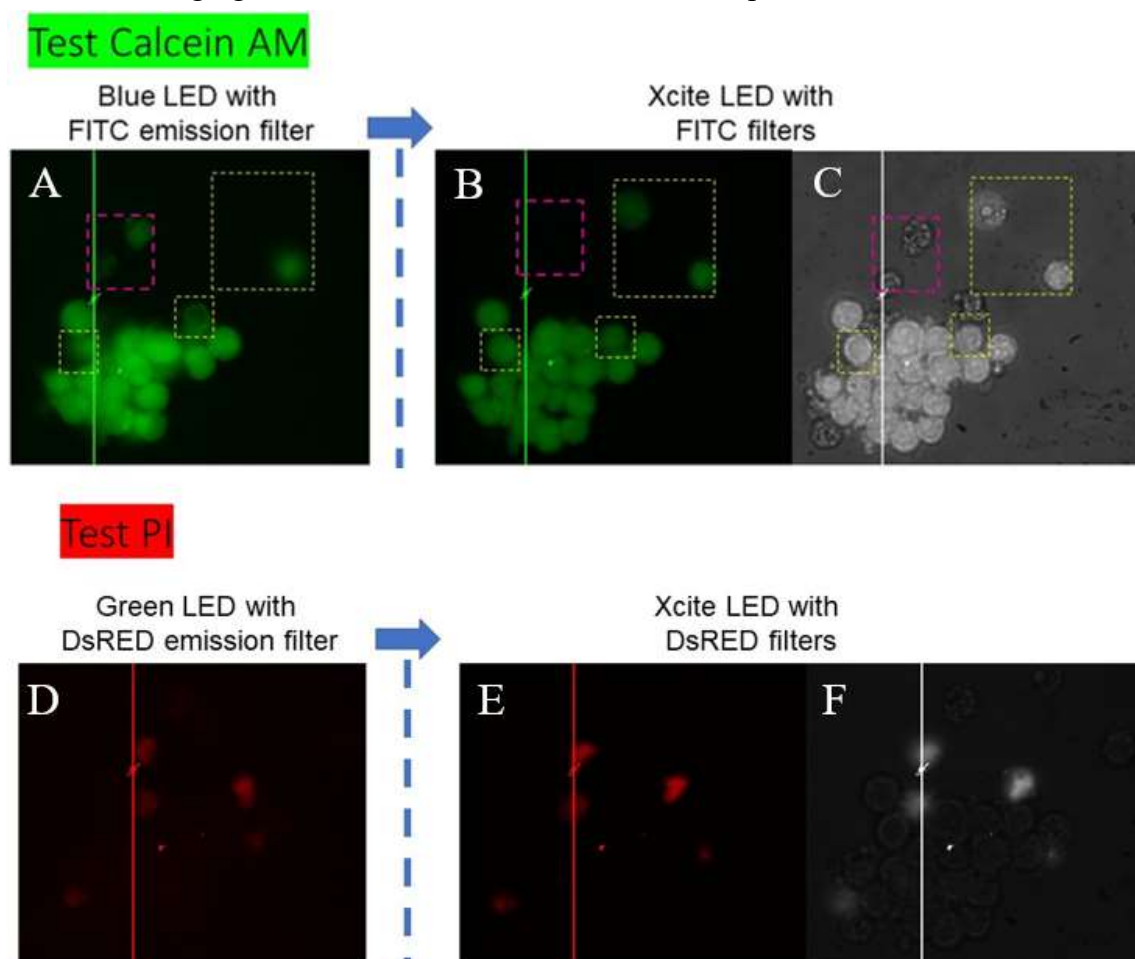

Figure A.2 Cell viability stains fluorescence information comparison: A) and D) by using the side-illumination (Blue LED and Green LED) with the corresponding emission filters; B) and E) by using the standard XCite fluorescence setup; The grey images C) and F) are the combination of the

brightfield imaging plus the fluorescence imaging. The straight line in the middle is due to the damaged camera pixels.

With the preliminary test of the side-illumination device on the fluorescence information, it is feasible to employ the compact and the cost-effective device in any microscope setup for both sample visualization and fluorescence information test.

APPENDIX B – MODIFICATIONS OF FEMTOSECOND LASER SETUP FOR THE OPTOPORATION OF JURKAT CELLS

As the preliminary exploration of the femtosecond laser-mediated optoporation of NPs decorated Jurkat cells shows that there is a narrow laser energy operational range. For the better manipulation of the floating Jurkat cells for the optoporation with high quantity and efficiency, it is proposed that the suspension cells are constantly pumped to flow through a microfluidic channel which offers the spatial and temporal manipulation with the reshaped laser line with a uniform energy profile. The ideal optical setup is illustrated in Figure B.1, the femtosecond laser with a uniform energy distribution irradiates NPs decorated cell flow in the microfluidic channel with a syringe pump. The treated labelled cells are collected at the end of the fluidic channel for further analysis.
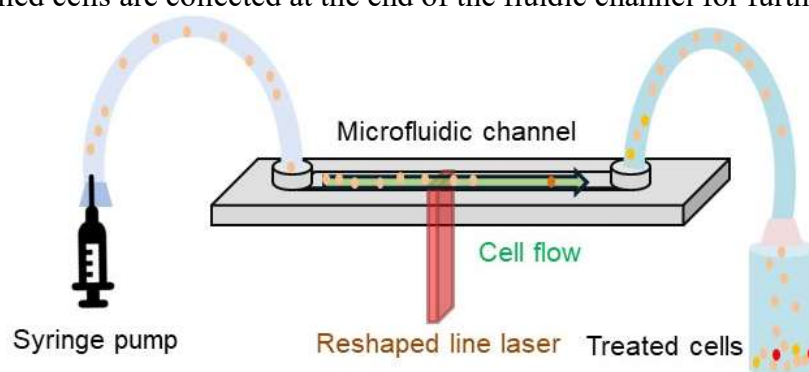

Figure B.1 The modified femtosecond laser optical setup for suspension Jurkat optoporation with high throughput. The NPs decorated Jurkat cells are pumped into the microfluidic channel at a specific speed. The desired reshaped laser line irradiates the cell flow with a uniform energy deposition. The laser treated cells are collected in a container for the further optoporation and viability analysis.

The visualization of NPs-cell complex in the microfluidic channel is challenging as the commercial fluidic channel is built in the middle of a special plastic substrate which scatters a lot of illumination light which is for the NPs-cell visualization. Side-illumination is employed for the visualization of NPs-cell complex in the fluidic channels to reduce the complexity of the system and with enough NPs-cell contrast. As shown in Figure B.2, the NPs decorated Jurkat cells are cultured in the microfluidic channel and the NPs are easy to be observed in the cellular environment. For NPs-cell complex imaging, the side-illumination device provides a much easier and better option. We use the 40x objective for the imaging.
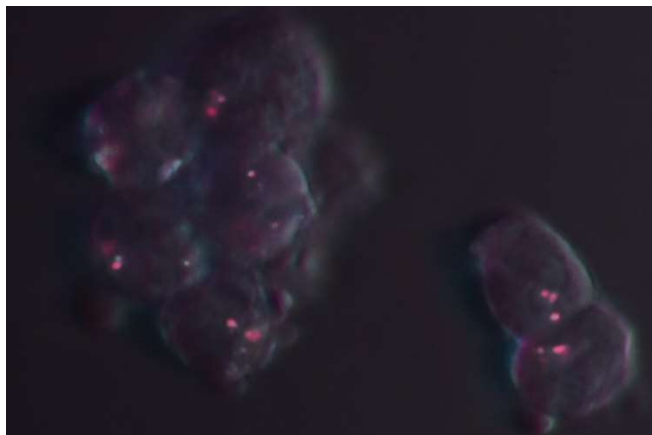
Figure B.2 NPs visualization in Jurkat cellular environment within a microfluidic channel by the side-illumination device. The pinkish bright spots are the cell membrane attached NPs, 40x objective is used.

In addition, the femtosecond laser profile needs to be modified to achieve a uniform distribution. Allowing the Jurkat cell flow in the microfluidic channel is affected by the femtosecond laser irradiation with the same energy (Figure B.3.A), it is proposed that the laser focal spot is reshaped into the laser line (Figure B.3.B). The preliminary modification of the optical system is illustrated in Figure B.3.C, the HeNe laser is used for the test due to the ease of use. The following beam splitter (BE) is used to broaden the beam from the laser source. With the convex cylindrical lens generating a focused line at the back aperture of the 4x objective, the modified laser focus profile is demonstrated as a smooth line.
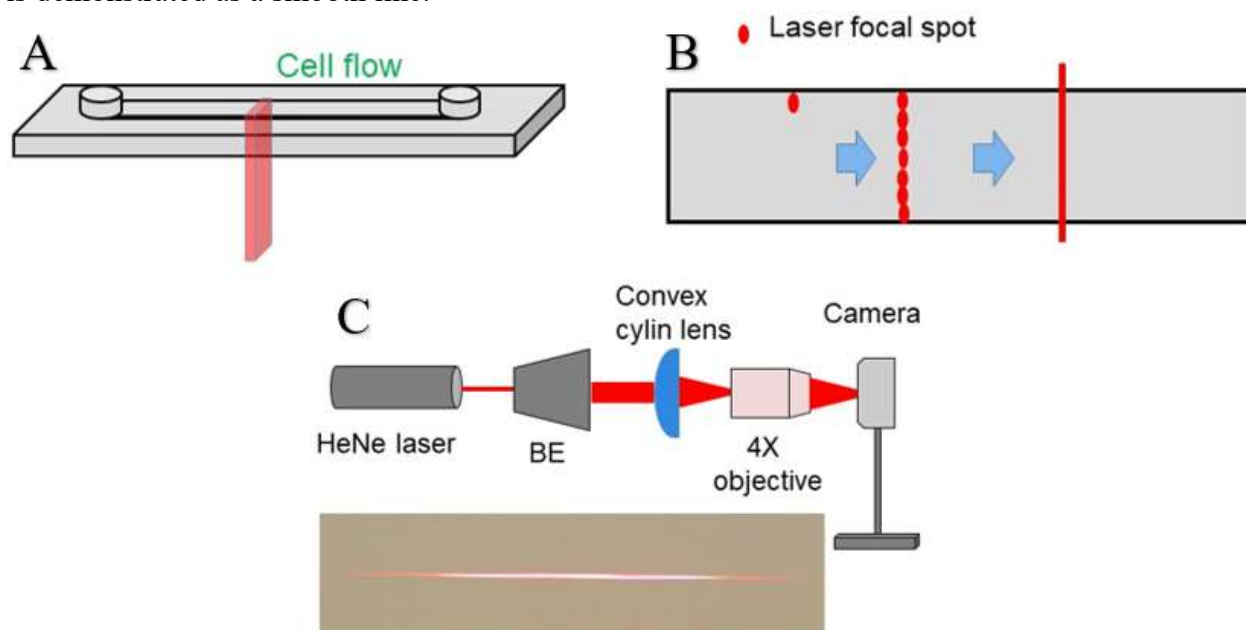
Figure B.3 A) Modifications on reshaping the laser in the laser optical path; B) The proposed reshaped laser line is to replace the laser focal spot scanning; C) The laser reshaping is realized by applying a cylindrical lens before the objective.

To characterize the laser focal point before and after the laser profile change, the energy distribution and the size of the focus are tested and analyzed. Before the laser profile reshapes, the focal point and the energy distribution are shown in Figure B.4.A. The focal point diameter is measured around 16 μm as in Figure B.4.B. For the modified line shape laser focus, the characterizations are in two directions, demonstrated in Figure B.5.B, the modified laser focus profile is a crescent-shaped line with a size of 9 μm x 0.3 mm.
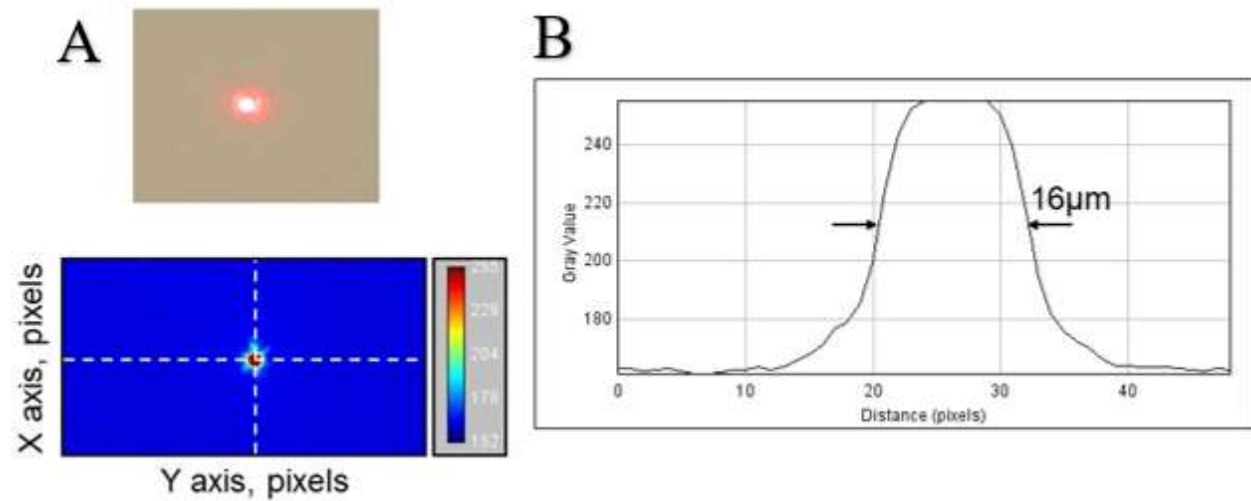

Figure B.4 Laser focus characterization before reshaping. The laser focal point diameter is around 16 μm.
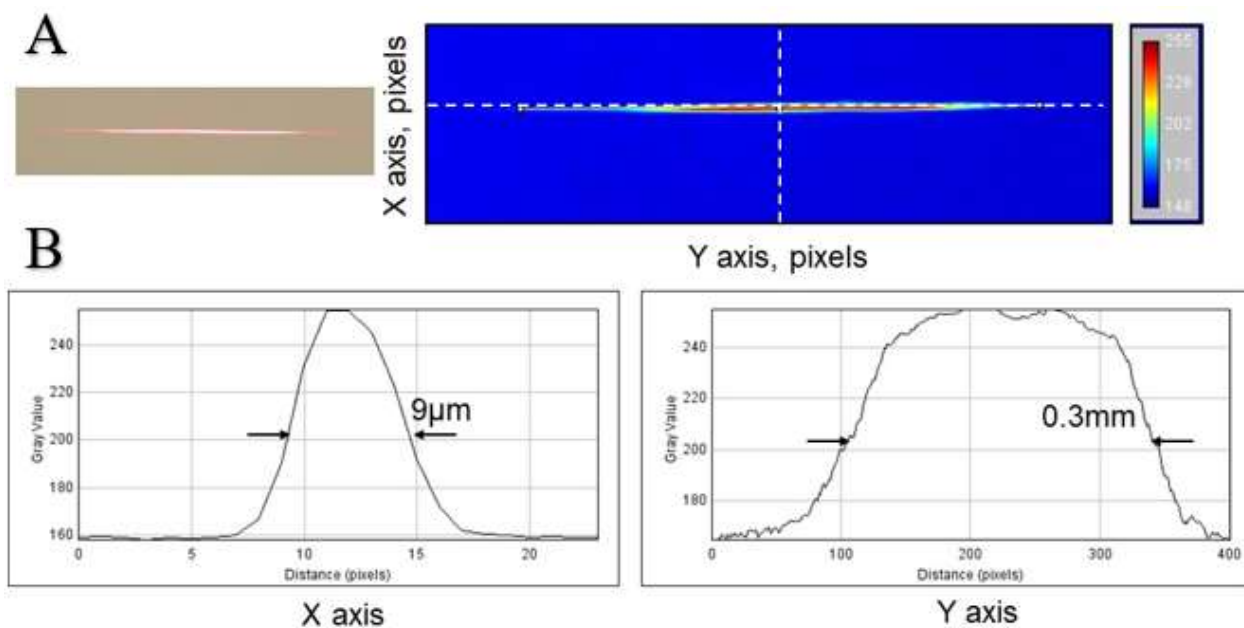
Figure B.5 Laser focus characterization after reshaping. The focal point (~16 µm) is reshaped to a crescent-shaped line with a size of 9 µm x 0.3 mm. The reshaped line could be applied to irradiate the suspension cells in the microfluidic channels.